Stereoscopy and tomography of coronal structures

Von der Fakultät für Elektrotechnik, Informationstechnik, Physik
der Technischen Universität Carolo-Wilhelmina
zu Braunschweig
zur Erlangung des Grades einer
Doktorin der Naturwissenschaften
(Dr.rer.nat.)
genehmigte
Dissertation

von Judith de Patoul
aus Brüssel, Belgien

Bibliografische Information der Deutschen Nationalbibliothek

Die Deutsche Nationalbibliothek verzeichnet diese Publikation in der Deutschen Nationalbibliografie; detaillierte bibliografische Daten sind im Internet über `http://dnb.d-nb.de` abrufbar.

1. Referentin oder Referent: Prof. Dr. Karl-Heinz Glassmeier
2. Referentin oder Referent: Prof. Dr. Sami K. Solanki
eingereicht am: 18. August 2011
mündliche Prüfung (Disputation) am: 21. Oktober 2011

ISBN 978-3-942171-65-6

uni-edition GmbH 2012
http://www.uni-edition.de

Printed in Germany

In memory of Agnès van der Straeten.

Vorveröffentlichungen von Teilergebnissen dieser Arbeit

Teilergebnisse aus dieser Arbeit wurden mit Genehmigung der Fakultät für Elektrotechnik, Informationstechnik, Physik, vertreten durch den Mentor der Arbeit, in folgenden Beiträgen vorab veröffentlicht:

Publikationen:

- de Patoul, J., Inhester, B., Feng, L., Wiegelmann, T. (2011). 2-D and 3-D polar plume analysis from the three vantage positions of STEREO/SECCHI A, B and SOHO/EIT. *Solar Physics*, in press

Tagungsbeitäge:

- de Patoul, J., Feng, L., Inhester, B., Wiegelmann, T. (2011). *2-D and 3-D polar plume analysis from the three vantage positions of STEREO/SECCHI A, B and SOHO/EIT.* Stereo-4/SDO-2/SOHO-25 Workshop, Kiel, Germany. (Vortrag)
- de Patoul, J., Feng, L., Inhester, B., Wiegelmann, T. (2010). *3D reconstruction of polar plumes from the three vantage positions of STEREO/SECCHI A,B and SOHO/EIT using the Hough-wavelet transform.* Solar-Terrestrial Center of Excellence, Royal Observatory of Belgium. (Eingeladener Vortrag)
- de Patoul, J., Feng, L., Inhester, B., Wiegelmann, T. (2010). *3D reconstruction of polar plumes from the three vantage positions of STEREO/SECCHI.* Solar Image Processing Workshop V, Les Diablerets, Switzerland (Vortrag)
- de Patoul, J., Feng, L., Inhester, B., Wiegelmann, T. (2010). *Stereoscopic 3D reconstruction of polar plumes from the three vantage positions of STEREO/SECCHI A, B and SOHO/EIT using the Hough-wavelet transform.* 38th COSPAR Scientific Assembly 38, Bremen, Germany. (Poster)
- de Patoul, J., Feng, L., Inhester, B., Wiegelmann, T. (2009). *Stereoscopic reconstruction of polar plumes from STEREO/SECCHI data using a wavelet-Hough transform.* Stereo-3/SOHO-22 Workshop, Bournemouth, Dorset, England. (Poster)
- de Patoul, J., Feng, L., Inhester, B., Wiegelmann, T. (2008). *3D reconstruction of polar plumes from STEREO/SECCHI images using the Hough transform.* Solar Imaging Processing Workshop IV, Baltimor, USA. (Vortrag)
- de Patoul, J., Feng, L., Inhester, B., Wiegelmann, T. (2008). *Study of the temporal evolution of polar plumes detected in STEREO/SECCHI images.* STEREO Consortium Meeting 8, Washington, USA. (Vortrag)

Contents

Abstract **9**

I Introduction **13**

1 Introduction to the Physics of Solar Corona **15**
1.1 Quick Journey through the Sun . . . 15
1.1.1 Solar Interior . . . 16
1.1.2 Solar Atmosphere . . . 17
1.2 Physics of the Solar Corona . . . 22
1.2.1 Coronal Magnetic Field . . . 23
1.2.2 X-rays and EUV Coronal Emission . . . 24
1.2.3 Coronal Holes . . . 25
1.2.4 Polar Plumes . . . 27
1.3 Space Missions for Observation of the Solar Corona . . . 33
1.3.1 General Overview . . . 33
1.3.2 SOHO/EIT and STEREO/SECCHI/EUVI Telescopes . . . 36
1.3.3 Camera Model . . . 39

2 Motivation and Goals of the Thesis **41**

II Image Processing & 3-D Reconstruction Techniques **45**

3 Image Processing Tools **47**
3.1 The Image as a 2D Signal . . . 47
3.2 Continuous Wavelet Transform . . . 49
3.2.1 Family of Wavelets and Wavelet Transform . . . 49
3.2.2 Implementation . . . 53
3.2.3 Examples . . . 54
3.3 Hough Transform . . . 58
3.3.1 Hough Transform as Wavelet Transform . . . 58
3.3.2 Hough Transform for Plume Analysis . . . 60

3.3.3 Implementation . . . 61
3.3.4 Examples . . . 61
3.4 Hough and Wavelet Transform . . . 64
3.4.1 Hough-wavelet Transform . . . 64
3.4.2 Hough-wavelet Transform for Plume Analysis . . . 66
3.4.3 Implementation . . . 67
3.4.4 Examples . . . 67
3.5 Summary and Conclusion . . . 71

4 3D Reconstruction Tools 73
4.1 Sinogram . . . 73
4.2 Tomography . . . 75
4.2.1 Filtered Backprojection in 2D . . . 76
4.2.2 Tomography for Solar Differential Rotation . . . 80
4.2.3 Implementation . . . 81
4.3 Stereoscopy . . . 82
4.3.1 Triangulation and Correspondence . . . 83
4.3.2 Triangulation with Hough-wavelet Coefficients . . . 84
4.4 3D model and Reconstruction . . . 86
4.4.1 Sinogram . . . 87
4.4.2 Filtered Backprojection Reconstruction . . . 88
4.4.3 Stereoscopic Reconstruction . . . 89
4.5 Summary and Conclusion . . . 92

III Plume Study 95

5 Plume Identification and Temporal Evolution in 2D 97
5.1 Image Pre-Processing . . . 97
5.1.1 Non-solar Feature Removal . . . 99
5.1.2 Contrast-enhancement Technique . . . 99
5.2 Plumes in the Hough-wavelet Space . . . 101
5.3 Time Series and Sinogram . . . 103
5.4 Summary and Conclusion . . . 111

6 Plume 3D Reconstruction 113
6.1 Tomography . . . 113
6.2 Stereoscopy . . . 114
6.3 Comparison between Tomography and Stereoscopy . . . 118
6.4 Plume Lifetime and Cross Section . . . 120
6.5 Plumes and other Phenomena . . . 123
6.6 Summary and Conclusion . . . 126

IV Conclusion & Outlook **129**

Appendix **135**

A Image transforms **135**
A.1 Hölder regularity 135
A.2 Wavelets 135

B Dipole Magnetic Field **137**

Bibliography **139**

Acknowledgements **146**

Abstract

The hot solar corona consists of a low density plasma, which is highly structured by the magnetic field. To resolve and study the corona, several solar Ultraviolet (UV) and X-ray telescopes are operated with high spatial and temporal resolution. EUV (Extreme UV) image sequences of the lower solar corona have revealed a wide variety of structures with sizes ranging from the Sun's diameter to the limit of the angular resolution. Active regions can be observed with enhanced temperature and density, as well as "quiet" regions, coronal holes with lower density and numerous other transient phenomena such as plumes, jets, bright points, flares, filaments, coronal mass ejections, all structured by the coronal magnetic field.

In this work, we analyze polar plumes in a sequence of Solar EUV images taken nearly simultaneously by the three telescopes on board of the spacecraft STEREO/SECCHI A and B, and SOHO/EIT. Plumes appear in EUV images as elongated objects starting on the surface of the Sun extending super-radially into the corona. Their formation and contribution to the fast solar wind and other coronal phenomena are still under debate. Knowledge of the polar plume 3D geometry can help to understand some of the physical processes in the solar corona. In this dissertation we develop new techniques for the characterization of polar plume structures in solar coronal images (Part II) then we analyze these structures using the techniques (Part III):

- We design a new technique capable of automatically identifying plumes in solar EUV images close to the limb at 1.01–1.39 $R_{\odot}$. This plume identification is based on a multi-scale Hough-wavelet analysis. We show that the method is well adapted to identifying the location, width and orientation of plumes. Starting from Hough-wavelet analysis, we elaborate on two other techniques to determine 3D plume localization and structure: (i) tomography employing data from a single spacecraft over more than half a rotation and (ii) stereoscopy from simultaneous data observed by two or more spacecrafts. For tomography, we consider the filtered back projection method for which we incorporate the differential rotation of the Sun. For stereoscopy, we use three view directions for a conventional stereoscopic triangulation. These multi-scale Hough-wavelet analyses, stereoscopy and tomography extentions have been applied for the first time in a coronal plumes study.

- The temporal evolution of the mean orientation of plumes from May 2007 to April 2008 is then analyzed and discussed. Since the plume orientation is assumed to follow the coronal magnetic field, this analysis reveals: (i) a mean orientation of plumes more horizontal than for a dipole magnetic field, (ii) an asymmetry of the coronal open polar cap magnetic

field from the solar rotation axis by up to 6° and (iii) a variation of these orientation and asymetry over the year.

- Finally, with the help of the reconstructed 3D geometry of the plumes, we study in detail their temporal evolution as well as the shape and size of their cross sections. The study reveals: (i) different lifetimes of plumes from 2-3 days up to 9 days and (ii) the presence of both near-circular plume cross sections and plumes with curtain-like structures. Also discussed is the plumes positions and their relation to other coronal phenomena such as coronal holes and jets. Plumes are found to be located inside coronal holes, and jets could explain the intensity enhancement within the plumes.

Part I

Introduction

Chapter 1
Introduction to the Physics of Solar Corona

For a long time, mankind has tried to come up with scientific explanations to understand the nature of the Sun and related phenomena resulting from its activity. It is also of great interest to scientists since the Sun is the closest star, which can be observed in detail. The first developed telescopes allowed, for example, Galileo and others to observe sunspots in the solar atmosphere for the first time around 1611. Since then, technology for building new instruments has seen a continuous improvement offering increasingly high quality observations of the Sun.

We start by giving a brief overview in Section 1.1 of the solar structure from its interior, where energy and magnetic fields are generated, to the upper atmosphere and the solar corona. We then describe the physics of the corona in Section 1.2 by explaining its magnetic field, emission lines and some related phenomena. Section 1.2.3 and 1.2.4, raises the issue of polar plumes, which are the central object of research presented in this thesis. And finally, in Section 1.3, we introduce the space missions built to observe the corona and, which have obtained the data used in this study.

1.1 Quick Journey through the Sun

The Sun is a G2V star located along the main sequence, with 70 % of its mass composed of hydrogen, 28 % of helium and the rest made up of heavier elements. Table 1.1 (a) shows very briefly some most important properties of the Sun.

The Sun can be divided into different layers depending on the local physical properties and processes. The layers are the the solar interior (subdivided into core, radiative zone and convective zone), which extends up to one solar radius $R_\odot$, and the solar atmosphere (subdivided into photosphere, chromosphere, transition region, corona and heliosphere). $R_\odot$ =6.955×10^5 km and is defined as the distance from the center up to the optical depth $\tau = 2/3$ (Stix, 2004), where the temperature has its effective temperature $T_{\rm eff}$, which is $L_\odot = 4\pi R_\odot^2 \sigma T_{\rm eff}^4$ where $T_{\rm eff}$ = 5778 K, $L_\odot$ is the luminosity and σ is the Stefan-Boltzmann constant.

Fig. 1.1 (b) shows the different layers of the Sun according to our current understanding.

The Sun

Temperature surface:	T_{eff}=5778 K
Mass:	$M_{\odot}$=2×10^{30} kg
Radius:	$R_{\odot}$=6.955^{5} km
Luminosity:	$L_{\odot}$=3.8×10^{26} W
Visual Brightness:	-26.7
Absolute Magnitude:	4.8

(a)

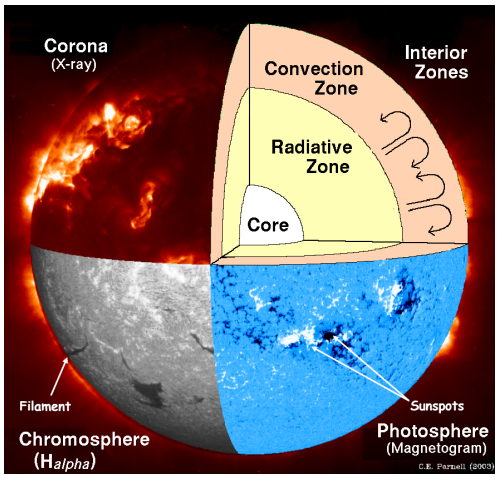

(b)

Figure 1.1: (a) Some fundamental physical characteristics for the Sun (Lang, 2001; Stix, 2004). (b) Simplified sketch of the Sun's structure from its interior to the atmosphere (C.E. Parnell).

1.1.1 Solar Interior

In the solar standard model (Phillips, 1992), the Sun's interior is divided into three zones: In the core, the huge pressure condenses solar matter to 150 g cm^{-3} giving the conditions for nuclear fusion, which provides the energy source of the Sun, and leading to temperature of 15.6×10^{6} K. The core extends to about 0.25 $R_{\odot}$. From 0.25 $R_{\odot}$ to 0.7 $R_{\odot}$, the temperature gradient is small enough to keep the matter stably stratified so that the energy produced in the deep interior of the Sun is transported by radiation (radiative zone). With increasing radial distance, from 0.7 $R_{\odot}$ to the solar surface at 1.0 $R_{\odot}$, the material becomes cooler (from 7×10^{6} K to 2×10^{6} K) and the density drops (from 20 g cm^{-3} to 0.2 g cm^{-3}). Beyond 0.7 $R_{\odot}$, the gradient of temperature becomes so large that solar matter is hydrostatically unstable (see Schwarzschild criterion, Phillips, 1992) and the energy is transported by convection (convection zone). The outermost layer of convection cells appear on the surface of the Sun as a granulation pattern (Rieutord and Rincon, 2010). On the surface, above which the solar gas becomes optically transparent, the temperature drops to 5778 K and the density to 0.2 g cm^{-3} (Fig. 1.2). While the bulk of solar interior below 0.7 $R_{\odot}$, rotates nearly as a solid body, the base of the convection zone shows a region of strong radial shear in the angular rotation. This boundary layer between the radiative layer and convective layer is known as the tachocline. Above, the convection zone exhibits differential rotation varying with latitude (Howe, 2009). A dynamo mechanism operating in the tachocline is generally considered to be the source of the Suns magnetic field (Charbonneau, 2010). Strong toroidal magnetic fields generated by the velocity shear rise through the convection zone with magnetic buoyancy and related instabilities, and emerge at the visible solar surface in the form of bipolar magnetic regions.

Differential Rotation

The Sun rotates about its axis approximately once every 27 days. However, the rotation is not

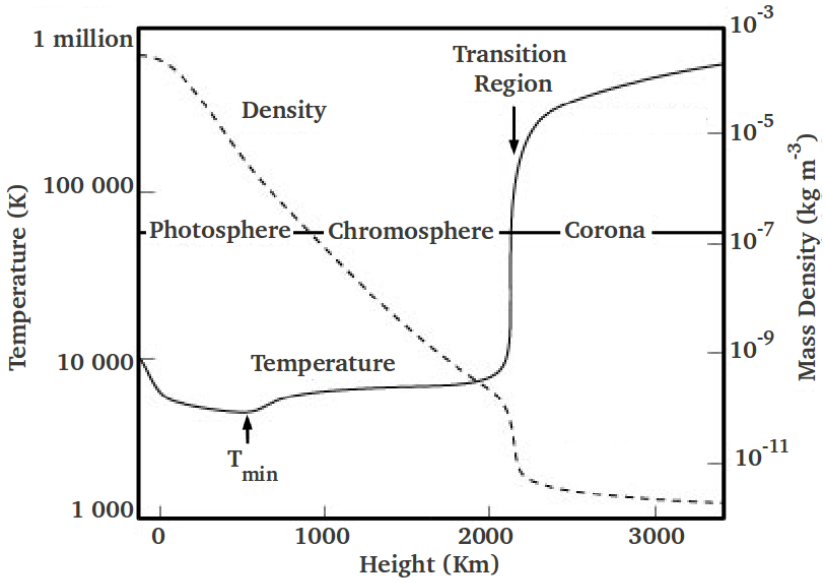

Figure 1.2: Average of the quiet Sun of the temperature and density as function of height where zero correspond to the solar surface at one $R_\odot$. Locally, large variations in temperature and density are present (Lang, 2001).

uniform, being substantially slower near the poles than at the equator (Howe, 2009). As seen above, the differential rotation starts in the solar interior between the radiative zone and the convection zone and extends beyond the solar surface. The differential rotation on the surface has been observed since 1630[1]. Current measurements commonly express rotation, ω, in even powers of $\sin\beta$ as (Howard and Harvey, 1970),

$$\omega(\beta) = A + B\sin^2\beta + C\sin^4\beta \quad [^\circ\ \mathrm{d}^{-1}], \tag{1.1}$$

where β is the latitude, A is the equatorial rotation rate in $^\circ\ \mathrm{d}^{-1}$; B and C determine the differential rotation rate in $^\circ\ \mathrm{d}^{-1}$. We consider the current set of accepted average values $A = 14.71^\circ\ \mathrm{d}^{-1}$, $B = -2.39^\circ\ \mathrm{d}^{-1}$ and $C = -1.78^\circ\ \mathrm{d}^{-1}$ determined by measuring the rotation of Doppler shift of features in the solar photosphere (Snodgrass and Ulrich, 1990). Beck (2000) gives a comparison of differential rotation measurements from different techniques (see, Fig. 1.3): Doppler shift, feature tracking and helioseismology techniques. The rotation measurements are consistent within a margin of 5 % (Beck, 2000). Depending on the latitude, a full rotation takes between 34.18 days at the pole and 24.46 days at the equator.

1.1.2 Solar Atmosphere

Fig. 1.2 shows a lateral average over the density and temperature above the visible surface of the quiet Sun. From the temperature variation, the solar atmosphere is conventionally subdivided

[1]As early as 1630, Christoph Scheiner noted that sunspots near the equator traverse the solar disk more rapidly than those near the poles (Paternò, 2010).

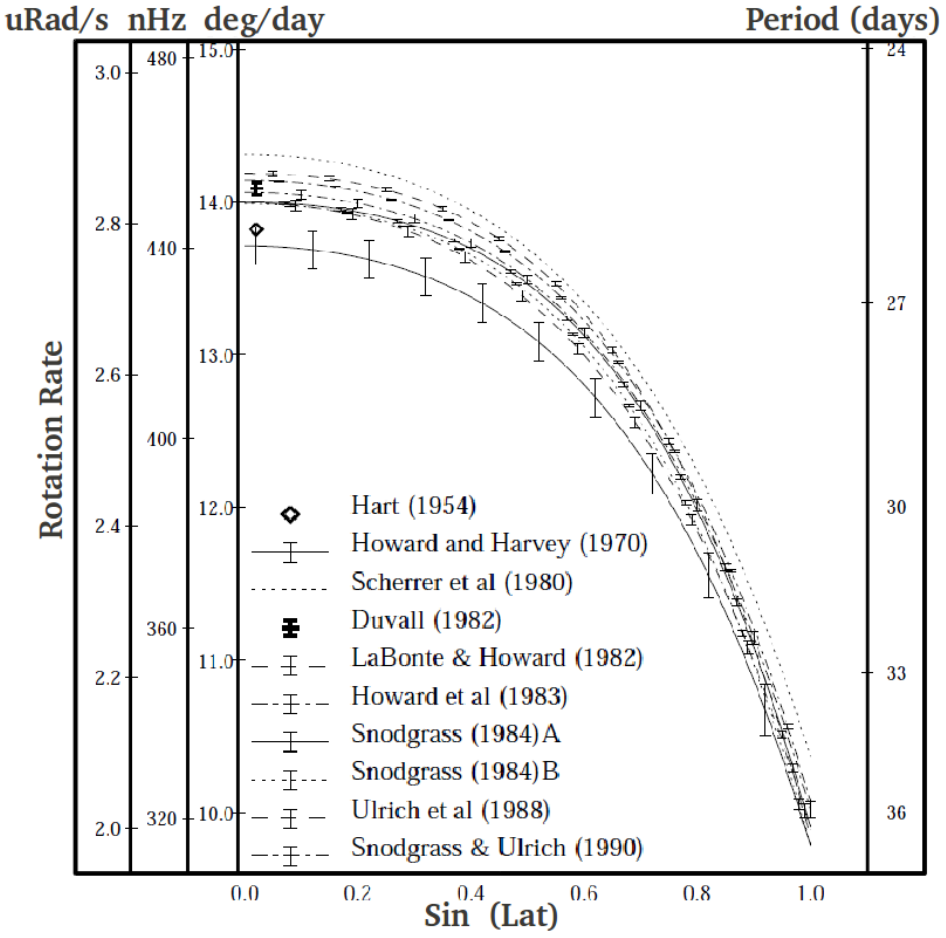

Figure 1.3: Comparison of differential rotation measurements. (Beck, 2000)

into the cool Photosphere (5800 K) and Chromosphere (20 000 K), the Transition region with a strong temperature gradient (from 25 000 K to 1.0×10^6 K) and the hot Corona (1.5×10^6 K). Also the subdivided regions are spatially much more inhomogeneous than suggested by Fig. 1.2. They are not "layers" but are very structured and temporally evolving regions, which is different than the underlying layers where gravity dominates and the Sun may be described in terms of layers.

Photosphere The transition from the hydrostatically unstable convection zone to a hydrostatically stable atmosphere occurs in the Photosphere. The photosphere represent the boundary, at which plasma becomes optically thick, i.e., the optical depth $\tau = 1$ (5000 Å). It is a thin layer (400–500 km) where the atmosphere becomes sufficiently transparent so that the photons can escape from the Sun. The decrease of the density contributes to the transparency. The photospheric magnetic field can be measured by the Zeeman effect, which produces line-of-sight magnetograms showing complex magnetic structures such as sunspots. At optical wavelength, sunspots appear as large dark patches on the surface where a strong magnetic field (about 2500–

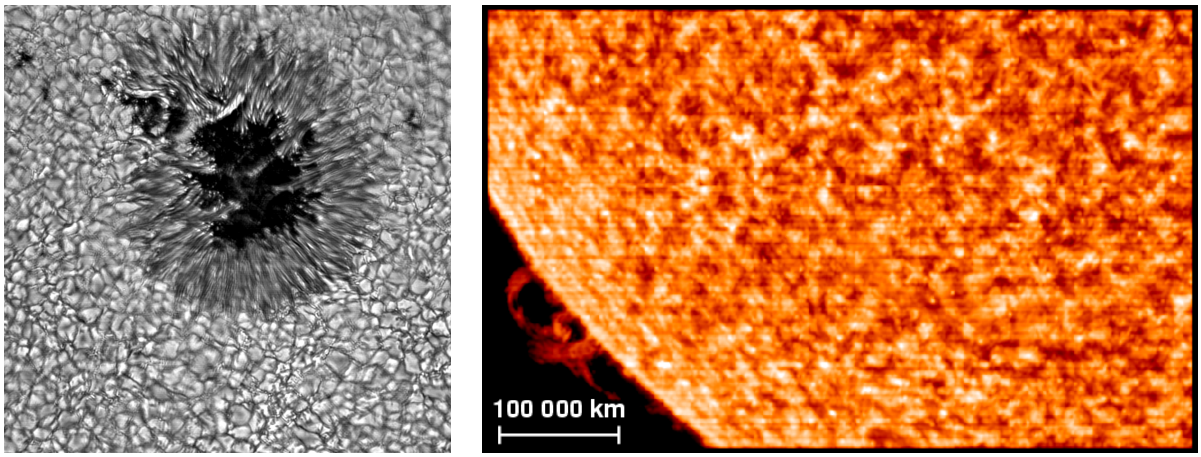

(a) (b)

Figure 1.4: (a) A sunspot surrounding by solar granular convection cells of about 1 Mm. The central, dark part of the sunspots is the umbra, the radially striated part is the penumbra. Picture produced by the Vacuum Tower Telescope at the Sacramento Peak Observatory (credit: T. Rimmele/NSO/AURA/NSF). (b) The solar transition region at 6×10^4 K as seen at 977Å. South-eastern part of a SUMER full-disk scan. The patchy pattern is the chromospheric network with a typical cell size of 20 Mm to 30 Mm. (Peter, 2001).

3000 G) concentration reduces the convective transport of heat from below (Solanki, 2003). Fig. 1.4 (a) shows an example of a sunspot. Due to the lower temperature (about 4000 K compared to about 6000 K), sunspots appear dark on the surface, surrounded by a penumbra where the field direction diverges horizontally into the solar atmosphere. In contrast, quiet surface regions are dominated by a random pattern of convection cells, called granules. They appear as bright features surrounded by dark edges, Fig. 1.4 (a). The granules have a size of the order of 1000 km, a lifetimes of 5 min to 8 min and mean vertical velocity lower than 0.5 km s^{-1} (Zirin, 1966). Groups of granules may form a super granular structure, (Nordlund et al., 2009). Typically this is observed in the chromosphere lines where the magnetic field is believed to impose the supergranular cells, Fig. 1.4 (b).

Chromosphere The photosphere is succeeded by a narrow layer (about 2500 km) called chromosphere, within which the temperature increases again with height from the temperature minimum 4.2×10^3 K up to 10.0×10^3 K. Theories of heating mechanisms are still under debate (Hall, 2008). Many oscillations are observed in the chromosphere (Schmieder and Murdin, 2000). When acoustic waves travel upwards through the solar atmosphere the density gradient leads to a shock-wave formation which dissipate the energy to heat, (Schmieder and Murdin, 2000). With increasing temperature, atmospheric gas particles are more frequently and more highly ionized and the spectral lines differ from those in the photosphere (Stix, 2004). A particularly important chromospheric emission line is the Hα line at 6563 Å visible as reddish emission during a total solar eclipse. This reddish emission gave its original name *color-sphere*, (Bray and Loughhead, 1974). And other important emission line is the Fraunhofer line of singly ionized calcium (Ca II 3934 Å) (Phillips, 1992). Organized magnetic field structures can be observed in the

chromosphere because the plasma pressure is not sufficient to mix the magnetic fields as in the photosphere and below. For example, we observe the chromospheric network, which outlines the boundaries of supergranules in the photosphere rising into the chromosphere by concentrated magnetic flux tubes. The chromospheric network appears as a patchy pattern, Fig. 1.4 (b). The typical cell size ranges from 20 to 50 Mm (Simon and Leighton, 1964; Del Moro, 2004; Delouille et al., 2005).

Transition Region Between the chromosphere and the corona, in the transition region, the temperature increases drastically from 10^3 K up to 10^6 K. Pressure balance in presence of the steep increase of temperature requires an equally steep decrease in density (see in Fig. 1.2). In particular, the almost complete ionization of hydrogen prohibits radiative cooling by emission of hydrogen lines.

Corona Finally in the outer part of the transition region, the mean temperature profile flattens to an extended region, the corona, with a temperature of 10^6 K and with an extremely low density. The existence of a hot solar corona is still puzzling. Several theories have been proposed and two most likely candidates are the heating by dissipation of magneto-acoustic and Alfén waves and and by magnetic reconnection (Ulmschneider, 1996; Podladchikova, 2002). The physics of the corona are described in more detail below.

The height profiles in Fig. 1.2 only represent the horizontal average over density and temperature. However, the magnetic field penetrating the solar atmosphere causes strong horizontal variations on a broad range of scales. On large scales, we can distinguish roughly three different types of regions in the lower corona: Active regions (AR), quite Sun (QS) and coronal hole (CH) regions. The pattern and the distribution of these regions also varies with time. We have roughly outlined the three different regions in Fig. 1.5.

Solar Cycle The magnetic activity of the Sun, which is manifested by the sunspots visible on the surface or by eruptive phenomena in the upper atmosphere and corona, shows a cyclic variation with a period of about 11 years (Solanki, 2003). During this solar cycle, the number of sunspots is enhanced during the maximum and reduced during the minimum activity (see Fig. 1.6). Two Hα images taken in 2002 during the maximum activity and in 2007 during the minimum show also the difference in magnetic activity: large prominences and bright plage regions in the neighborhood of the sunspots can be seen in the Hα images during large activity (Fig. 1.6 (a)) while the image taken in 2007 shows only very few structures (Fig. 1.6 (b)). This magnetic activity is also observed in the corona, see Fig. 1.5. Moreover, the orientation of the Sun's magnetic dipole moment and also hemispheric polarity orientation of sunspot groups (Hale's law) show that a complete magnetic cycle covers two 11 year-activity cycles with systematic reversals of the solar magnetic field every 11 years (Solanki et al., 2006).

Active Regions The term active region designates a region, in which strong magnetic field concentrations are rooted. In EUV images, they appear bright due to a higher plasma density and electron temperature than in the surrounding region. Active regions are most of the time

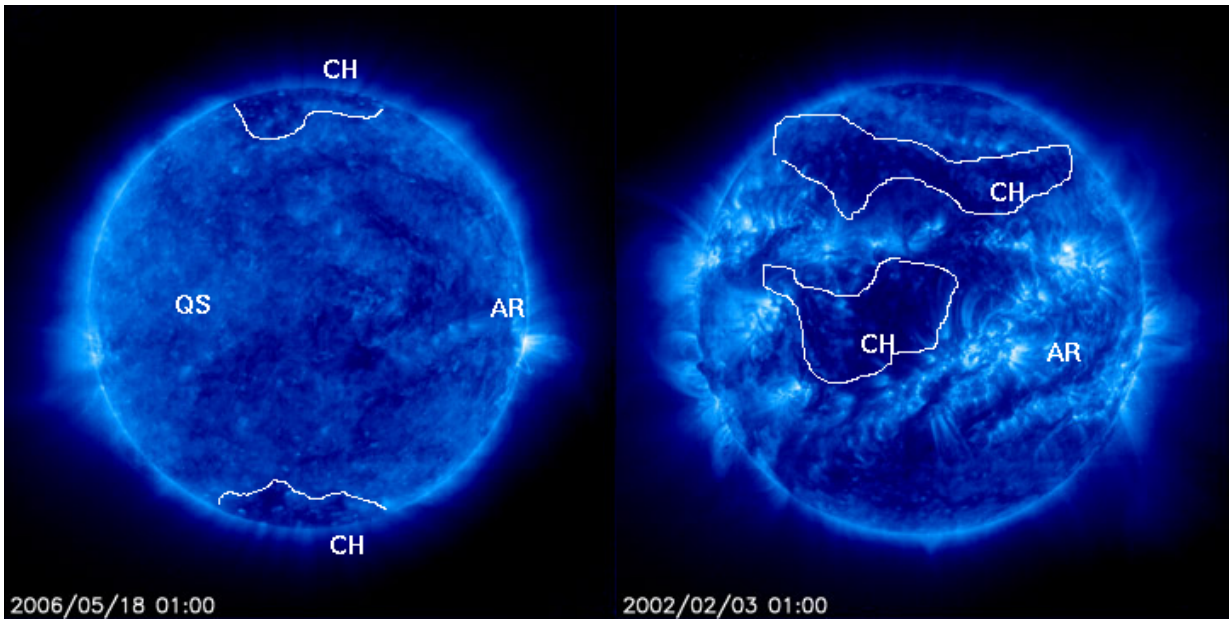

Figure 1.5: Two SOHO/EIT images of the solar corona at 171 Å. The three different zones are overploted in white: Active regions (AR), quite Sun (QS) and coronal hole (CH). On the left, the image was taken during the minimum of activity, and on the right, during the maximum of activity.

associated with sunspot groups (Solanki et al., 2006). Many dynamic phenomena such as flares (e.g., Benz and Murdin, 2000; Hudson, 2011) and coronal mass ejections (e.g., Thompson et al., 1998; Gibson and Low, 1998), occur in these regions.

Coronal Holes Coronal holes are the lowest density plasma components of the Sun's outer atmosphere (Cranmer et al., 1999; Cranmer, 2002). They appear on the surface as dark patches in EUV and X-ray lines. At low coronal activity, they are concentrated at the poles and during times of large activity they are distributed all over the solar surface (see, Fig. 1.5). Coronal holes are associated with rapidly expanding magnetic fields. Along these open field lines, the high-speed solar wind ($\approx$ 800 km s^{-1}) can escape into the heliosphere (Cranmer et al., 1999). They have been observed as the site of thin, ray-like polar plumes.

Quiet Sun Quiet Sun region designates the rest of the solar coronal disk. In the past, this zone was believed to be quiet with low magnetic activity. With increased resolution of solar observations, considerable activity has been observed in these regions, however at a much smaller scale than in an active region. Typical examples of activity in these "quiet" Sun regions are bright points, small flares, small coronal mass ejections and jets (Podladchikova, 2002; Sanchez Almeida et al., 2010).

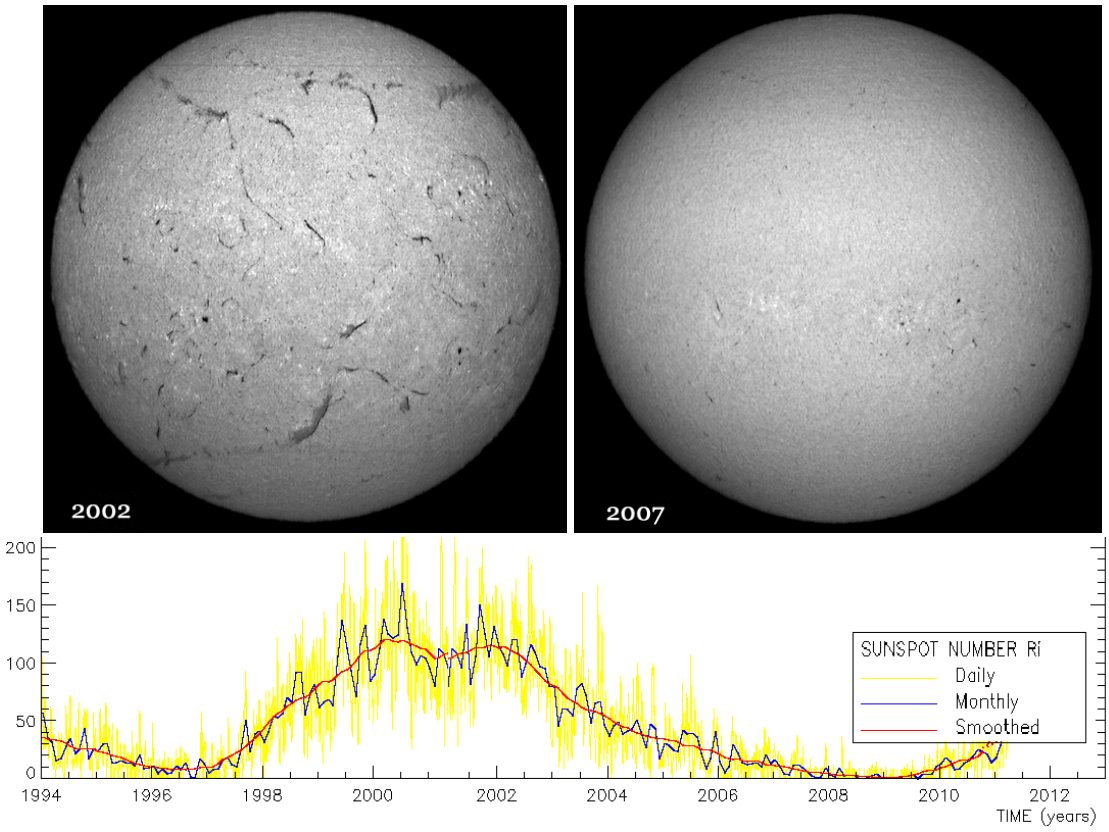

Figure 1.6: Big Bear Solar Observatory contrast enhanced full disk H-alpha images in 2002 and 2007. Below, sunspot number over a solar activity cycle (SIDC data center, http://www.sidc.be**).**

1.2 Physics of the Solar Corona

The corona can only be observed in visible light from Earth during a solar eclipse when the intense direct light from the Sun is occulted by the Moon. Fig. 1.7 (a) shows a photograph taken from the Earth during the solar eclipse 2008. The image has been processed to increase the contrast in order to show more clearly the structures in the corona. The appearance of the corona gave use to its name already in ancient Greek as *κοωνη*.

The corona consists of a plasma at a temperature of about 10^6 K. Because of this high temperature, the coronal plasma is highly ionized, and the corona is visible in a variety of emission lines predominantly in the extreme ultraviolet (EUV) and X-rays spectrum. In these wavelength ranges, we need to observe from space in order to avoid the absorption by the Earth's atmosphere. The solar corona is far from being homogeneous: Its density, temperature and magnetic field vary spatially and temporally. The solar corona is highly structured by the magnetic field, which is rooted at the solar surface and is partially open to the heliosphere allowing the solar wind to escape into the heliosphere. Contrary, closed magnetic loops consist of hotter and denser plasma, which is confined by the magnetic field. These loops appear brighter in EUV due the

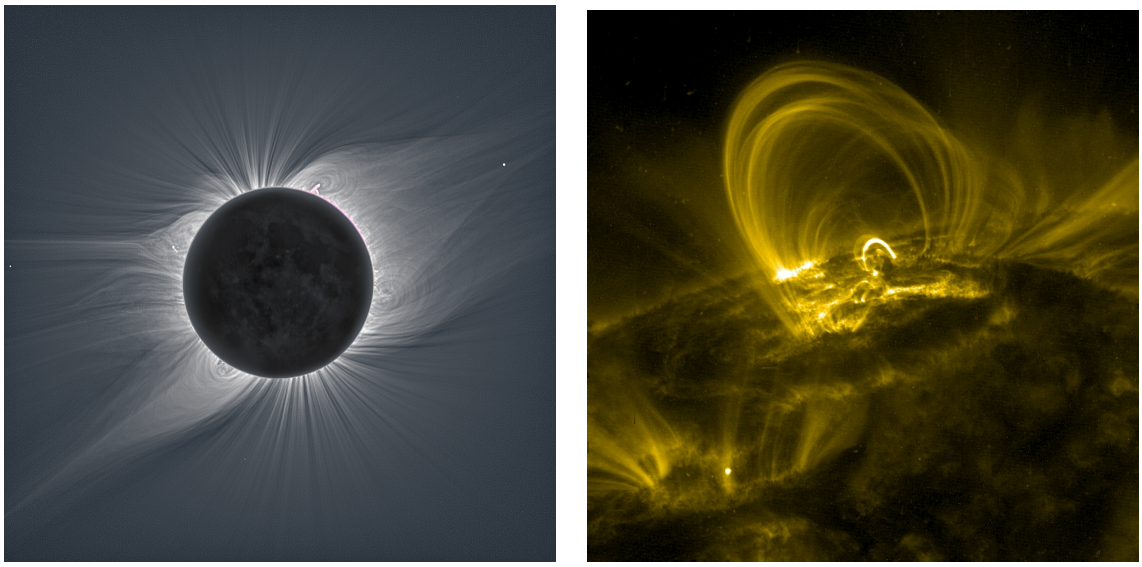

(a) (b)

Figure 1.7: (a) Solar eclipse the 1st of August 2008. (Credit: Hana Druckmüllerová, Miloslav Druckmüller) (b) SOHO/TRACE image of an active region (AR-10808) in September 2005.

higher temperature and density since emission intensities in X-ray and EUV lines roughly scale with the plasma density squared. An example of a set of closed loops is shown in Fig. 1.7 (b).

1.2.1 Coronal Magnetic Field

Unlike the photospheric field, the coronal magnetic field cannot easily be measured by the Zeeman effect. The enhanced temperature broadens the emission lines, which makes the observation of the Zeeman spectral line splitting difficult. One way[2] to estimate the coronal magnetic field topology and strength is its reconstruction by extrapolation from surface magnetograms, which are measurements of the Zeeman splitting in the photosphere (Wiegelmann, 2008; Thalmann and Wiegelmann, 2009; Tadesse et al., 2009). In the corona, the magnetic energy density usually dominates the plasma and gravitational energy density (Aschwanden, 2004). The critical parameter, which describes the importance of the magnetic field for dynamical pressures, is the plasma-β parameter defined as the ratio of the thermal plasma pressure to the magnetic pressure:

$$\beta = \frac{\text{thermal plasma pressure}}{\text{magnetic pressure}} = \frac{nk_BT}{B^2/2\mu_0}\,, \tag{1.2}$$

where n is the number density, k_B is the Boltzmann constant, T the temperature, B magnetic field and μ_0 the magnetic permeability. Most parts of the corona have a plasma-β parameter of $\beta << 1$. As a consequence, the solar magnetic field influences most dynamic coronal phenomena. The charged particles of the hot coronal plasma are trapped along magnetic field lines. Some closed field lines in the corona appear bright in EUV where their plasma density is enhanced.

[2]There are several other ways to estimate the coronal magnetic field see Solanki (2003).

These bright loops outline the geometry of local magnetic field lines. The observation of the field line shape from EUV loops is an alternative way to obtain the magnetic field topology. Fig. 1.7 (b) shows a set of EUV loops displaying a complex topology. At higher altitudes of several $R_\odot$, the thermal plasma pressure approaches the magnetic field pressure (which means plasma-β approaches unity). Moreover, the dynamic pressure of the solar wind reaches the same order of magnitude (which means the solar wind velocity approaches the Alfvén velocity). Loops reaching these altitudes can open and connect eventually to the heliosphere. At low solar activity these open field lines are rooted predominately in the polar regions. At higher activity their footpoint regions also extend to lower latitudes. These regions are considered the source of the fast solar wind.

1.2.2 X-rays and EUV Coronal Emission

Electromagnetic emission from the corona occurs in a very wide spectrum ranging from radio waves to ultraviolet and X-rays. In the optical range we have Fraunhofer absorption lines embedded in the photospheric continuum (Phillips, 1992). In EUV and X-rays the emission is concentrated in emission lines. The data we use in this thesis were obtained from EUV imaging telescopes (Section 1.3), we therefore concentrate on the emission in EUV and X-rays of an optically thin plasma.
The emission in a spectral line of an ion X^{+m} occurs by transition from a upper level j to a lower level i

$$X_j^{+m} \rightarrow X_i^{+m} + \gamma \,,$$

where ion X_j^{+m} is m-times ionized. The photon γ is emitted at a wavelength λ_{ij} corresponding to the energy difference between levels i and j: $\Delta E_{ij} = ch/\lambda_{ij}$, with h the Planck constant and c the speed of light. The total power emitted in this transition per unit volume of coronal plasma, is

$$P_{ij}^{X} = N_j(X^{+m}) A_{ji} \frac{hc}{\lambda_{ij}} \quad [\text{erg cm}^{-3}\ \text{s}^{-1}] \,, \tag{1.3}$$

where $N_j(X^{+m})$ is the number density of atoms of the ion species X^{+m} in level j and A_{ji} is the Einstein spontaneous emission coefficient into level i. The intensity $I(\lambda_{ij})$ at wavelength λ_{ij} and observed at a distance R from the Sun is obtained by the integration of (1.3) over a volume element ΔV of interest in the corona (Golub and Pasachoff, 2009),

$$I(\lambda_{ij}) = \frac{1}{4\pi R^2} \int_{\Delta V} P_{ij}^{X}\ dV \quad [\text{erg cm}^{-2}\ \text{s}^{-1}] \,. \tag{1.4}$$

With an imaging instrument, the photon flux (1.4) into one pixel is the integration along the line of sight (LOS) of the total power (1.3) multiplying by the space solid angle Ω_{pixel} of one pixel:

$$I(\lambda_{ij})_{\text{pixel}} = \frac{\Omega_{\text{pixel}}}{4\pi} \int_{\text{LOS}} P_{ij}^{X}\ dl \,. \tag{1.5}$$

In the case of the corona, if we assume that the relative abundance of Ion X and the population

Wavelength	Emission line	Regions	$\log_{10}(T/\mathrm{K})$
white light	continuum	photosphere	3.7
1700 Å	continuum	Photosphere, minimum temperature	3.7
304 Å	He II	Chromosphere, transition region	4.7
1600 Å	C IV+cont.	Transition region, upper photosphere	5.0
171 Å	Fe IX	Quiet corona, upper transition region	5.8
195 Å	Fe XII	Corona	6.2
193Å	Fe XII, XXIV	Corona, hot flare plasma	6.1, 7.3
284 Å	Fe XV	Corona, active-regions	6.3
211 Å	Fe XIV	Corona, active-regions	6.3
335 Å	Fe XVI	Corona, active-region	6.4
94 Å	Fe XVIII	Corona, flaring regions	6.8
131 Å	Fe VIII,XX,XXIII	Corona, flaring regions	5.6, 7.0, 7.2

Table 1.1: Wavelength relation with temperature, emission line and corresponding region in the solar atmosphere (Lemen et al., 2011).

of the upper level j are in local thermal equilibrium, the level j is depopulated exclusively by spontaneous radiative decay to the level, i, and excited by inelastic electron collisions. With this assumptions, the equilibrium power P_{ji}^{X} can be expressed as,

$$P_{ji}^{\mathrm{X}} = 0.8 A_{\mathrm{X}} G(T_{\mathrm{e}}, \lambda_{ji}) N_{\mathrm{e}}^2 \quad [\mathrm{erg\ cm^{-3}\ s^{-1}}] \,,$$

where 0.8 is the hydrogen abundance relative to the electron density ; A_{X} is the abundance of element X relative to hydrogen ; $G(T_{\mathrm{e}}, \lambda_{ji})$ is the contribution function depending on the electron temperature T_{e} ; N_{e} is the electron density.
Therefore, observations of the corona in EUV emission lines yields in principle information about the electron temperature and the electron density. The Table 1.1 lists the equilibrium temperature of maximal emission at a specific wavelength observed by the instruments SDO/AIA, STEREO/SECCHI and SOHO/EIT[3].

1.2.3 Coronal Holes

Since polar plumes, which are the topic of this thesis, reside above coronal holes, we describe the characteristics of these regions more extensively.
Coronal holes cover a large part of the surface, from 20 % to 30 %, and are surface regions that are magnetically connected to the outer heliosphere (Wang et al., 1996). A local dominance of photospheric flux elements of one polarity provides a net field of about 10 G or more at the coronal base, which feeds the open flux (Solanki et al., 2006). These more uniform and unipolar surface regions can be observed in solar surface magnetograms.

[3]Those instruments are described in Section 1.3.

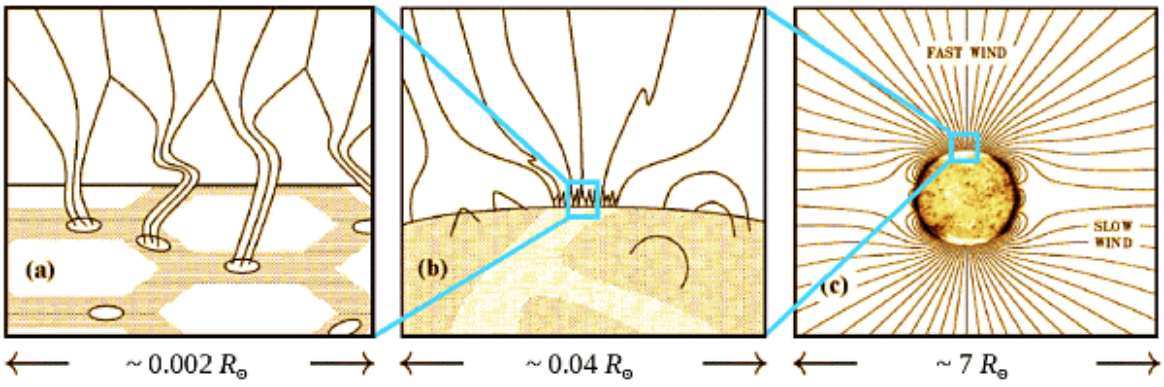

Figure 1.8: Illustration of unipolar magnetic field structure of polar coronal holes. The strong-field magnetic flux tubes in intergranules lanes (a) merge into "funnel, rooted in a supergranular network lane (b) then finally, extended into the corona (c). (Cranmer, 2009).

Hot coronal plasma in coronal holes cannot be confined on these open field lines and the plasma escapes from the corona along open field lines into the interplanetary space and feeds the heliosphere solar wind (Wilhelm et al., 2000). Density and pressure in the coronal hole are consequently reduced, which results in low emission in the UV and X-ray spectrum. Therefore, they appear as dark patches in these wavelengths.

The density difference is less pronounced in the photosphere and low chromosphere where the temperature does not exceed 7×10^5 K. Therefore, in the photosphere, coronal holes are hardly distinguishable from their surroundings (Cranmer, 2009).

The shape and location of coronal holes varies during the solar activity cycle. For about 1-2 years during solar maximum, coronal holes appear at low-latitude and are scattered all over the solar surface (Cranmer, 2009). Many low-latitude coronal holes are located near the edges of magnetically complex active regions, an example of this is shown in Fig. 1.5. Soon after the solar maximum activity, new-polarity coronal holes gradually grow at the poles. At about seven years around solar minimum, coronal holes become large and concentrated at the polar caps, which gives them their name of polar coronal holes (Cranmer, 2009).

If coronal hole regions are observed with high spatial and time resolution, it is apparent that they are highly structured. Some magnetic flux tubes, which emerge out of a coronal hole, are visible as polar plumes against the dark background in coronagraphs and EUV images close to the limb (see Section 1.2.4). There are also other small and short-live events such as e.g. jets, spicules, macrospicules and bright points.

The open field lines of coronal holes are rooted in thin chromospheric and photospheric unipolar magnetic flux tubes emerging mainly in the dark lanes between the photospheric granulation cells (Cranmer, 2009). These funnels are believed to be the source region of the fast solar wind. Fig. 1.8 illustrates the successive merging of these flux tubes between granules and supergran-

ules: Fig. 1.8 (a) is a zoom onto the photosphere where thin magnetic flux tubes concentrate in the dark lanes between photospheric granulation cells, which have a size of $\approx 1.5 \times 10^3$ km ($\approx 1.002\ R_\odot$). Fig. 1.8 (b) shows the chromosphere at a larger scale where the individual flux tubes form "funnels" and merge into a even larger network field distribution. This network is the supergranular network in coronal-hole and has a typical size of $\approx 30 \times 10^3$ km ($\approx 0.04\ R_\odot$). Finally, Fig. 1.8 (c) shows at large scales ($7\ R_\odot$) how the field extends into the corona.

1.2.4 Polar Plumes

The best observation time for polar plumes is during minimum solar activity when the coronal holes are largest in size and are located at the poles. We can see an example in Fig. 1.5. Fig. 1.9 shows the southern coronal hole observed in March 1995. The image combines observations from different instruments in white light and in EUV showing the space above the polar coronal hole from the limb out to $20\ R_\odot$. The image is transformed to cylindrical coordinates, so that the super-radial expansion of individual plumes can be seen in the image.

Thin, ray-like polar plumes have for long been observed above coronal holes (Saito, 1958; Stoddard et al., 1966; Newkirk and Harvey, 1968). The earliest measurements of polar plume were made in visible light during a solar eclipse (Saito, 1958). The plumes were found to follow the super-radially expanding open magnetic field lines above the polar limb. Space-based observations improved the understanding of plumes and inter-plume region. Similar coronal ray-like structures seen in EUV above coronal holes were found to be aligned with the plumes observed in white light (DeForest and Gurman, 1998). These authors therefore concluded that white light and EUV plumes were one and the same object. Studying plumes was found to be of great interest for the understanding of the acceleration of the fast component of the solar wind (Teriaca et al., 2003).

Plume, General Characteristics

Polar plumes consist of denser and cooler plasma compared to the surrounding inter-plume corona. The review paper from Wilhelm et al. (2011) gives a summary of measurements of plume temperatures, densities and outflow velocities studied up to now. The density is 3 times to 5 times higher inside a plume than in the nearby inter-plume corona and it decreases with height. The temperature inside plumes is below 1.0×10^6 K unlike the temperature of 1.0×10^6 K to 1.2×10^6 K in the inter-plume regions. The plasma outflow velocities in plumes have been determined using the Doppler dimming technique with both SUMER and UVCS instruments (Teriaca et al., 2003; Gabriel et al., 2003). The conclusions drawn by these papers argue different scenarios: (Gabriel et al., 2003) observe that plumes have a greater outflow speeds than in inter-plume. Whereas Teriaca et al. (2003) found only low velocities and conclude that plumes cannot be considered as the source of the fast solar wind. This was also confirmed by Feng et al. (2009) who corrected the observed Doppler shift by the angle of the reconstructed 3D plume axis with the line-of-sight. The velocity was found to be lower inside plumes than in the corona and inter-plums region with a value below 10 km s^{-1}.

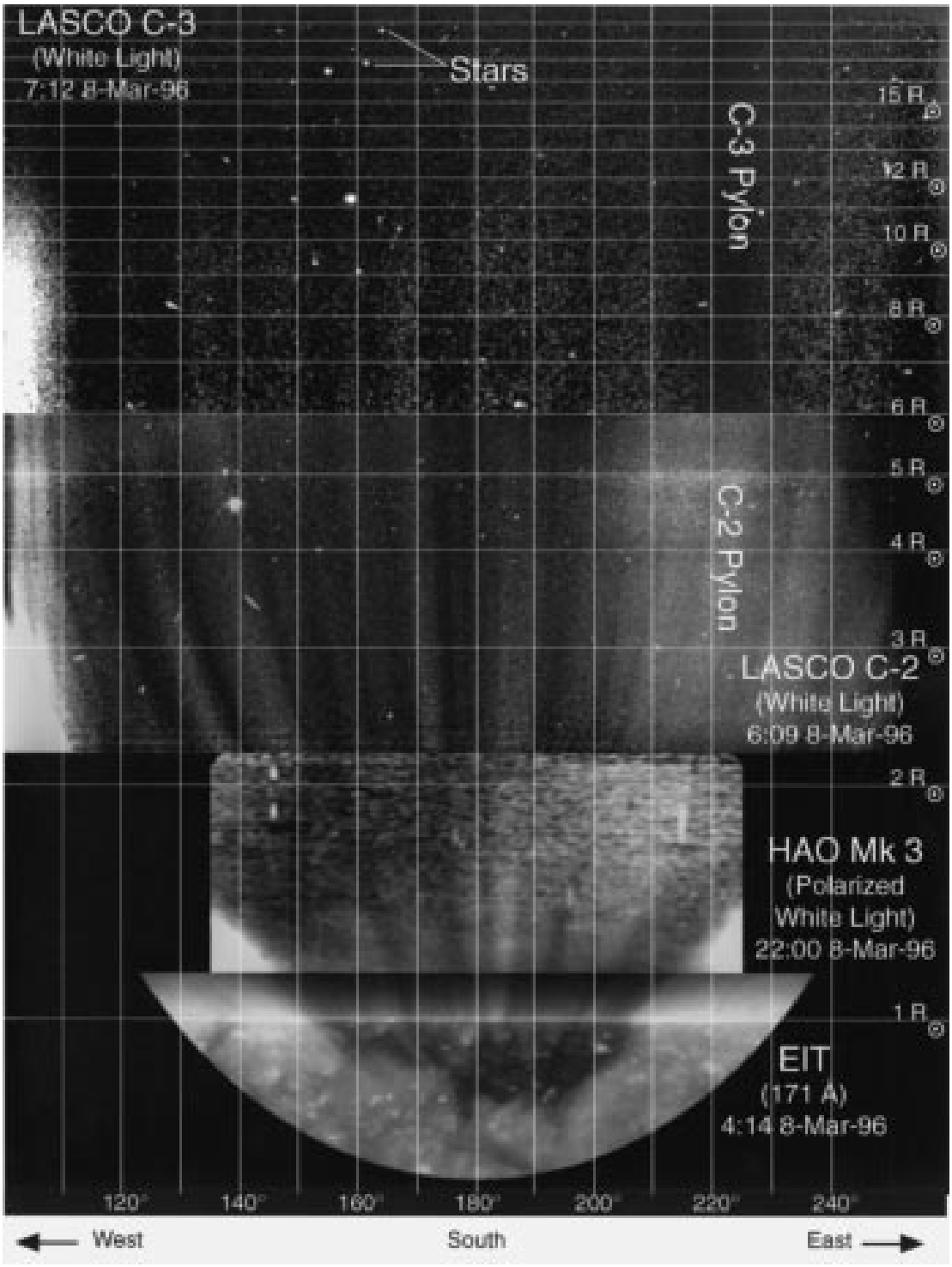

Figure 1.9: Image in radial coordinate system of a south coronal hole observed in Mars 1995. Superradial expansion of the coronal hole and individual plumes, can be seen in this image (DeForest et al., 1997).

Plume, 3D Geometry and Distribution

The general plume morphology has been related to the global structure of the polar magnetic field. From white light observations, plumes show a super-radial expansion with altitude (DeForest et al., 1997; Feng et al., 2009) as expected for near dipole magnetic field lines. Coronal plumes have a 3D structure, but the observations show only their projection on the plane of the sky. Since plumes are optically thin in white-light and EUV their observations are a line-of-sight integrations of the respective plume emissivity. Therefore, it is impossible to determine their 3D geometry from just 2D observations. A first sight, plumes appear to be plasma columns with a super-radial expansion similar to coronal holes. The 3D plume orientations has been identified by Feng et al. (2009) and subsequently compared with a basic dipole magnetic field. As expected, the plume orientations show a clear super-radial behavior. Near the limb, plumes have an average cross-section angle of about $2.0^\circ - 2.6^\circ$ corresponding to about 31 Mm on the surface (Wilhelm et al., 2011). However there is a broad variation of cross-section widths.

The 3D cross-section shapes of plumes are poorly known. Different assumptions of the 3D plume cross section shape and plume distribution have been proposed in the literature: DeForest et al. (1997) defined plumes as objects with a near-circular cross section having a diameter of about 30 Mm growing with height. Llebaria et al. (2002) proposed a fractal structure for the plume cross section, which would explain the large variations of their thickness and spatial distribution. Wang and Sheeley (1995) suggested a curtain- or sheet- like shape also proposed by Gabriel et al. (2003). Gabriel et al. (2005) suggested the existence of two different plume populations having distinct geometrical forms: the classical *beam plumes* having a near-elliptical cross section and the *curtain plumes*, which are only visible when the curtain is sufficiently aligned with the line-of-sight. This geometric effect would limit the detectability of curtain plumes to about 1 day to 3 days.
The distribution of plumes above a coronal hole is also under debate: Raouafi et al. (2007) observed that plumes are rooted preferably along a ring at latitudes between 70° and 80°. Since plumes are closely related to the network activity, Gabriel et al. (2009) proposed that the supergranular network imprints its spatial distribution onto the plume location and cross section shape. They claim that micro-plumes are concentrated within some 5 Mm of the cell boundaries and therefore call this population *network plumes*. Barbey et al. (2008) have used tomographic techniques for the reconstruction of pole plume observations showing a network pattern as proposed by Gabriel et al. (2009). Fig. 1.10 (b), shows a tomography reconstruction of the north pole emissivity by Barbey et al. (2008). We can see an network pattern that bears some resemblances to the supergranular network shown in Fig. 1.10 (a).

Plume Formation

Based on the empirical association between plumes and network brightening inside coronal holes, Wang and Sheeley (1995) and Wang (1998) suggested that plumes are formed when small magnetic bipoles reconnect with nearby unipolar flux concentrations in the solar chromosphere (Fig. 1.11). The procedure is as follows: a bipole inside a supergranular cell is pulled by con-

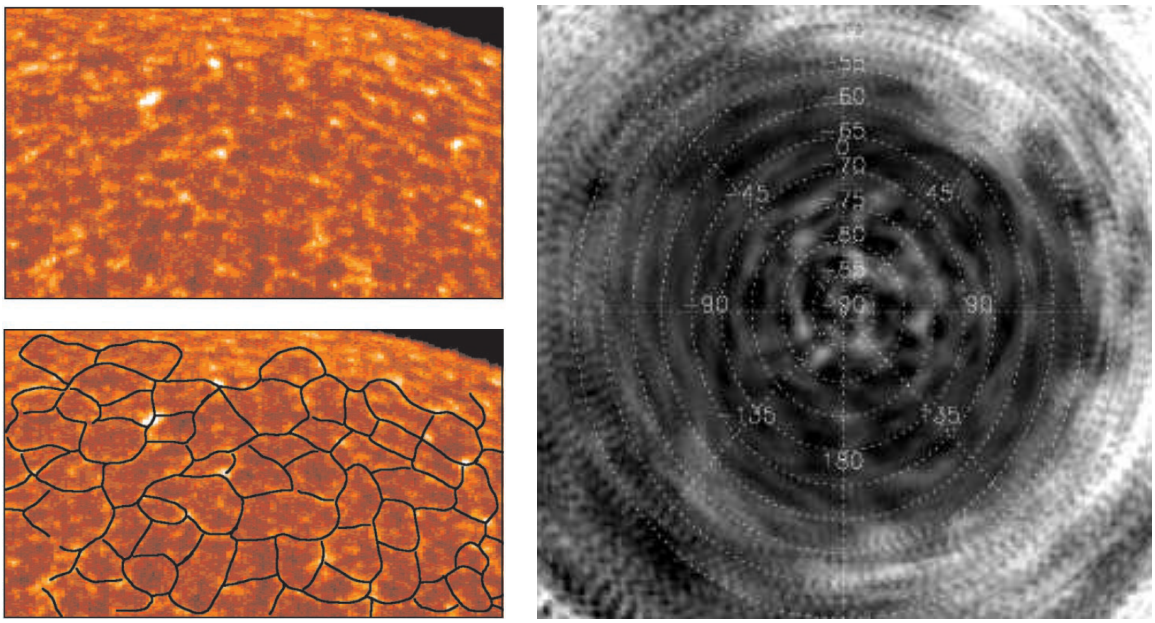

(a) **(b)**

Figure 1.10: (a) Chromospheric images from the north polar region, (SOHO/SUMER Si II 1533Å, 21-Sept-1996). Below, supergranular network structure determined by tracing the intensity using visual pattern recognition, is superposed (Hassler et al., 1999). (b) Tomography reconstruction of the north pole emissivity at 171 Å and at 1.05 $R_\odot$ using STEREO/EUVI A and B data (171 Å) and assuming a static corona (Barbey et al., 2008).

vective motions so that some, e.g., of its negative-polarity flux reconnects with a neighboring positive flux concentration (positive-polarity "monopole") present at one of the cell vertices. A corresponding amount of positive-polarity flux opens up at the other end of the bipole. The coronal temperature increases along the reconnecting field lines and gives rise to a plume at the location of the newly opened flux. However, the observation of polar plume and bipoles do not show a clear relationship; not every bipole or EUV bright point can be associated with a plume and a bright point is not always observed at the foot-point of a plumes. Also, whereas bright points erupt on a timescale of few hours, plumes grow and fade over a much longer time period.

Plume Lifetime

The lifetime of a plume is also poorly known. Llebaria et al. (1998) and DeForest et al. (2001) determined different time ranges. In the first paper, average lifetimes of 1 day to 3 days were obtained while in the second, characteristic lifetimes of a week and even longer were estimated. Plumes with a near-elliptical cross section were suggested to have a lifetime of the order of a week and occasionally longer (DeForest et al., 1997). Gabriel et al. (2005) proposed that the two characteristic lifetimes could be explained if *beam plumes* with a near-elliptical cross section have a lifetime of about a week, and *curtain plumes* are only visible briefly for 1 day to 2 days when the curtain is sufficiently aligned with the line-of-sight. Raouafi et al. (2008) showed that

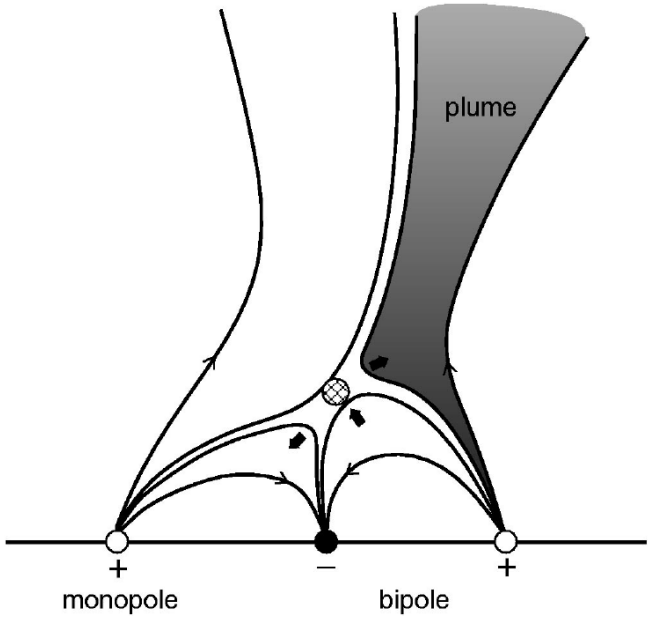

Figure 1.11: Schematic of flux exchange and formation of a plume. (Wang, 1998)

coronal jets can be also precursors of plumes. They found that these jets may be the responsible for the extended life cycle of a plume.

Coronal Plume Models

The observed plumes arise from small (diameter of 2 Mm to 4 Mm or 2 ” to 5 ”) unipolar magnetic flux concentrations on chromospheric network cell boundaries (DeForest et al., 1997). The plumes expand rapidly with height, in the range 1.00 $R_\odot$ to 1.05 $R_\odot$, to a diameter of about 30 Mm off the surface (Saito, 1965; Ahmad and Withbroe, 1977; Ahmad and Webb, 1978). This local spreading becomes then constant above about 1.05 $R_\odot$, (Suess et al., 1998). Plumes also show a global spreading imposed by the coronal hole geometry, which varies much more slowly. The assumption that plumes are rooted on unipolar magnetic flux concentrations, permits to model the geometry of the lowest portion of the plume in terms of a magnetic field configuration (Newkirk and Harvey, 1968; Suess, 1982; Del Zanna et al., 1997; Suess et al., 1998). Potential field models explaining the lowest portion of the plume behavior were first proposed by Newkirk and Harvey (1968) and by Suess Suess (1982). However, the models do not include plasma parameters such as density, temperature and plasma-β in their analysis. Del Zanna et al. (1997) proposed a magnetohydrodynamic model for solar coronal plumes taking into account the lateral pressure balance between the plume and the ambient plasma. They model plumes by assuming a density of 10^8 cm^{-3} to 10^9 cm^{-3}, an electron temperature of 10^6 K and a β-plasma parameter of 10^{-3} inside the base of the plume, so that plume geometry should be close to the shape of a force-free field. Fig. 1.12 shows density and velocity of the plume and the modeled magnetic field in cylindrical coordinates. In their model, density decreases with height as seen in the gray-scale contour map in Fig. 1.12, with denser regions displayed darker. It is interesting to also compare

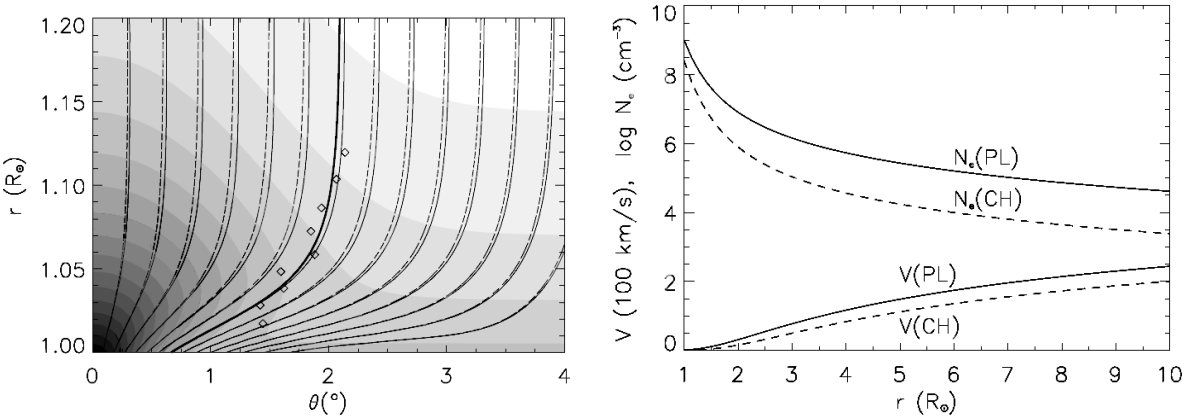

(a) (b)

Figure 1.12: (a) Plume model from Del Zanna et al. (1997) in cylindrical coordinates. The field lines are depicted with solid lines. The gray-scale contour map describes the density (from black to white the density decreases). (b) The density in units of cm^{-3} in logarithmic scale and the velocity in units of 100 km s^{-1}. The solid lines refer to the plume axis (PL) whereas the dashed lines refer to the background coronal hole (CH). (Del Zanna et al., 1997)

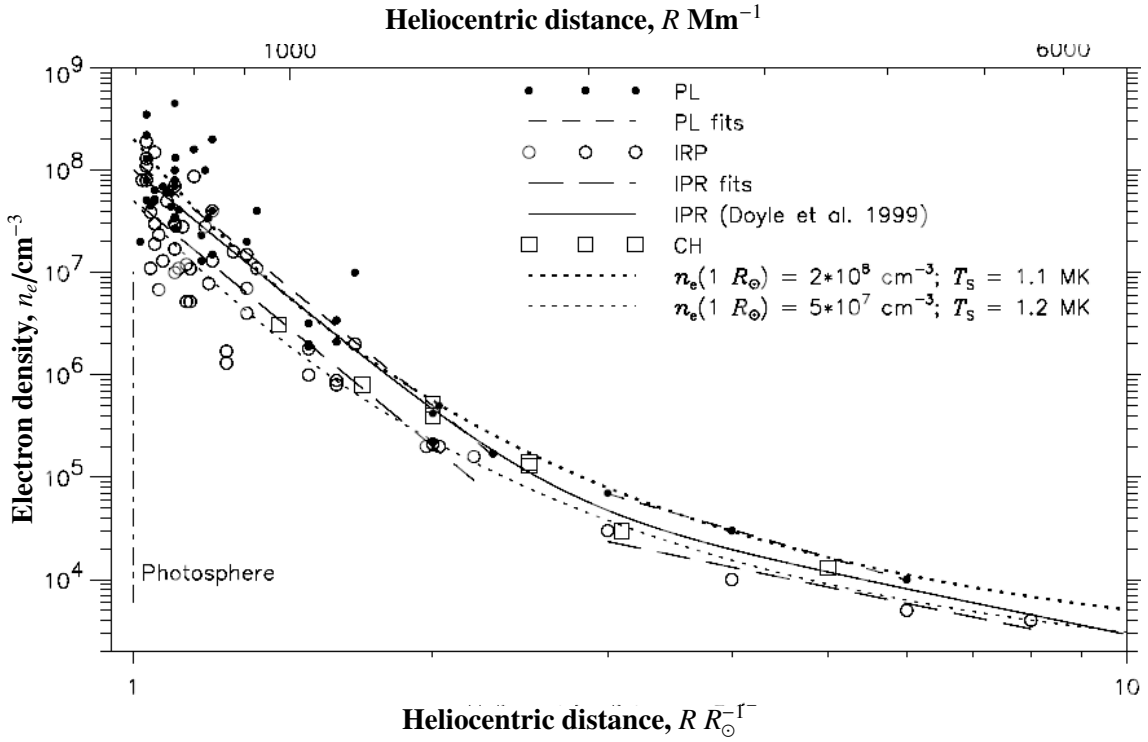

Figure 1.13: Electron density, in unit of cm^{-3}. Inside plumes (PL), inter-plume regions (IPR) and coronal holes (CH) measurements are plotted. (Wilhelm et al., 2011)

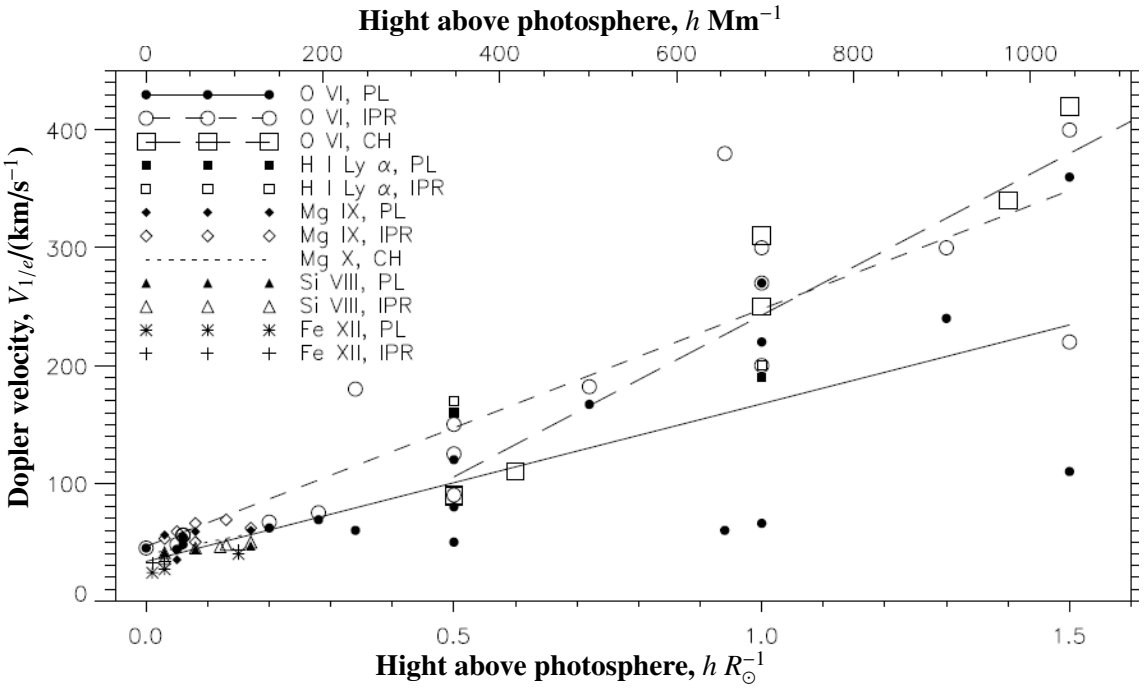

Figure 1.14: Dopler velocity measurements in unit of km s^{-1} for the inside plumes (PL), the interplume regions (IPR) and coronal holes (CH). (Wilhelm et al., 2011)

the density and outflow velocity given by the model with the observation values collected by Wilhelm et al. (2011), Fig. 1.13 and Fig. 1.14.

1.3 Space Missions for Observation of the Solar Corona

Nowadays, there are several space missions supplied with instruments continuously observing the Sun. Here, we focus on the missions SOHO and STEREO and only briefly mention mission SDO and the future mission SOLO. We then describe the specific instruments, which have produced the data we are using in this study.

1.3.1 General Overview

The Solar and Heliospheric Observatory (SOHO) mission is a cooperative effort between the space agencies NASA and ESA (Domingo et al., 1995). The satellite was launched in December 1995 with 12 instruments dedicated to helioseismology, observation of the solar atmosphere and in situ recordings of the solar wind. SOHO orbits the Lagrange Point L1 at a distance of about 1.5×10^6 km from the Earth and about 150.7×10^6 km from the Sun. At this point, the satellite is balanced by the gravitation of the Sun and the Earth and the centrifugal force, which keeps it in an orbit locked to the Earth-Sun line. As shown in Fig. 1.15, SOHO mission observations now cover more than a solar cycle.One of its instruments used in this study is the Extreme ultraviolet Imaging Telescope (EIT). It is a full-disk and subfield imager of EUV corona in four wavelengths

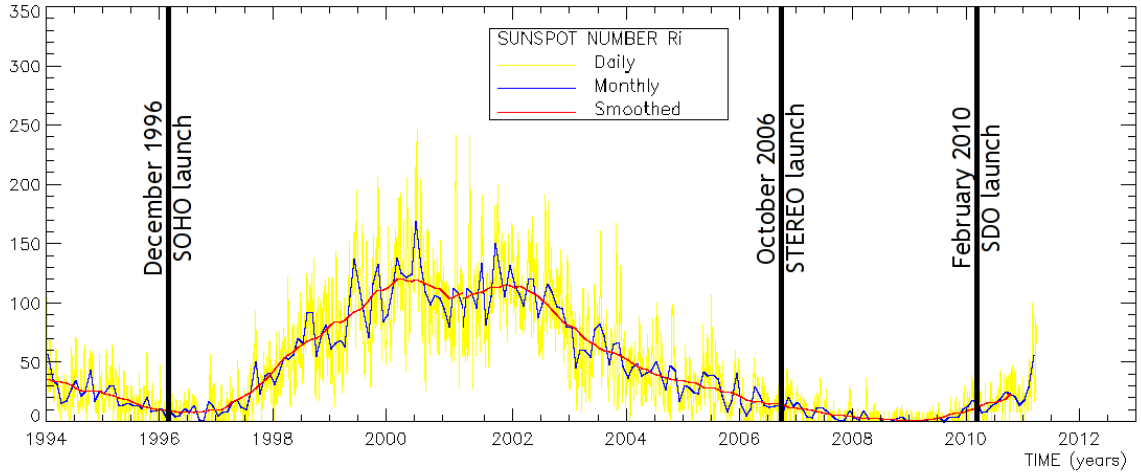

Figure 1.15: Sunspot number over the solar cycle (SIDC data center, http://www.sidc.be**). We have marked the launch data of SOHO, STEREO and SDO satellites. SOHO has been able to observe more than one solar cycle.**

(171 Å, 195 Å, 284 Å, 304 Å, see Table 1.1 for emission line and temperature correspondences) with a resolution of 5.18 ” pixel^{-1} or 2.95 ” pixel^{-1}, see Fig 1.16 for an example of one such image, (http://umbra.nascom.nasa.gov/eit/).

In October 2006, eleven years after the launch of SOHO, the Solar-Terrestrial Relations Observatory (STEREO) satellites were launched by NASA (Kaiser et al., 2008). The mission consists of two satellites, one ahead (STEREO-A) of the Earth orbit, the other (STEREO-B) trailing behind (see Fig. 1.17). This new pair of viewpoints provides a unique view of the Sun-Earth System. Each spacecraft is equipped with four instrument packages, which are identical in both spacecraft. The imaging package is called SECCHI (Sun Earth Connection Coronal and Heliospheric Investigation), (Howard et al., 2008). It consits of two coronagraphs (COR 1 and COR 2), which observe the inner corona (from 1.4 to 4.0 $R_\odot$) and outer corona (from 2.0 to 15.0 $R_\odot$), an Extreme Ultraviolet Imager (EUVI), which provides full Sun coverage, and an Heliospheric Imager (HI), which observe the heliosphere from the Sun to the Earth (from 12.0 to 318.0 $R_\odot$). The main scientific objective is to study initiation of coronal mass ejections (CMEs) on the solar surface and to follow their propagation through the inner heliosphere until the Earth. In this thesis, we use the images taken by the two Extreme Ultraviolet Imagers (EUVI-A and EUVI-B) belonging to the instrument package STEREO/SECCHI-A and STEREO/SECCHI-B, respectively. There are a full-disk imager of the EUV corona in four wavelengths (171 Å, 195 Å, 284 Å, 304 Å, see Table 1.1) with a resolution of 1.59 ” pixel^{-1}, see Fig 1.16 for an example of images, (http://secchi.lmsal.com/EUVI/). During 2007 and 2008 we have observations from three view directions; from the two STEREO spacecrafts and from SOHO spacecraft. During this time of period, the Sun was at its minimum of activity making the perfect situation for studying plumes and coronal holes.

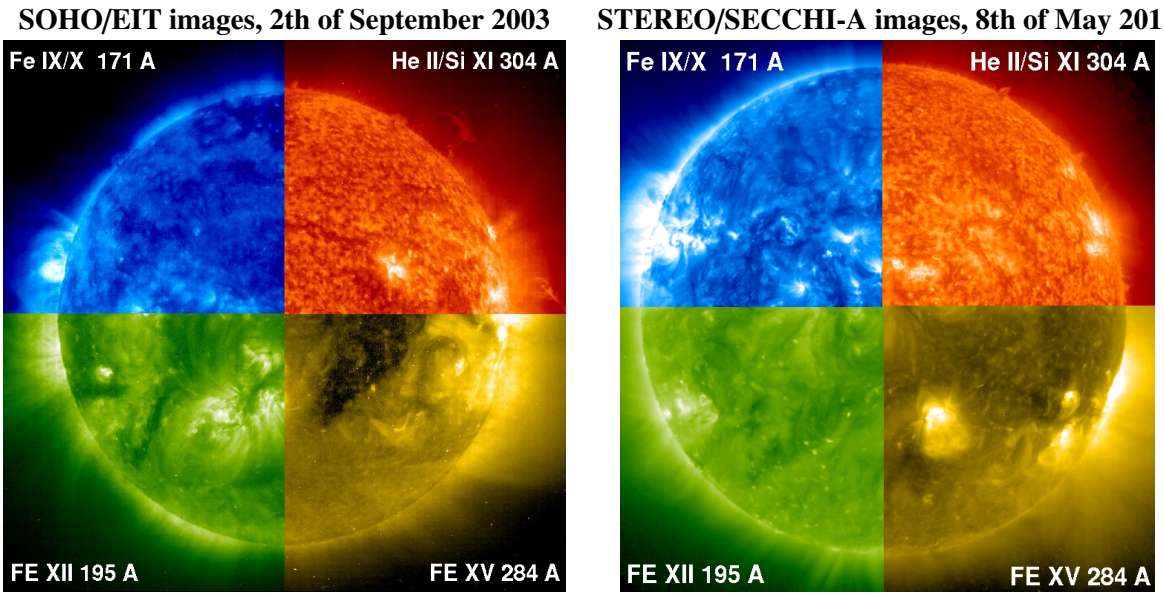

Figure 1.16: SOHO/EIT and STEREO/SECCHI-A images assemblage.

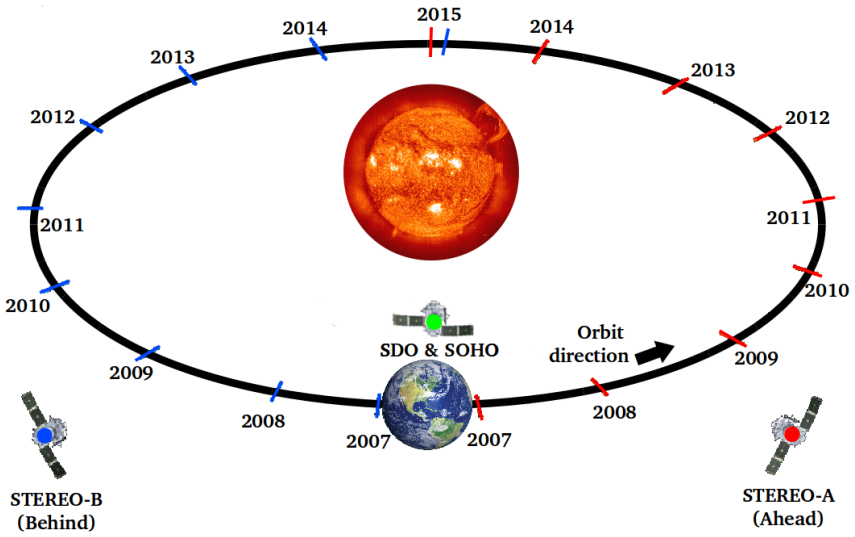

Figure 1.17: Diagram showing the orbits of the two satellites STEREO-A and STEREO-B. The Sun is represented in the center with the Earth below. This diagram is not to scale. (Illustration adapted from http://www.nasa.gov/mission$_$pages/stereo**)**

In February 2010, the Solar Dynamics Observatory (SDO) was launched (February 2010) by NASA. This spacecraft orbits around the Earth on a geosynchronous orbit giving roughly the same view direction as the SOHO mission but with higher spatial and temporal resolution. SDO is equipped with a full-disk imager, AIA (for Atmospheric Imaging Assembly, Lemen et al., 2011), which takes images of the solar atmosphere in 10 wavelengths (Table 1.1) with a cadence of 10 s and with a resolution of 0.6 " pixel^{-1}, (http://aia.lmsal.com/). However, the data are not included in this work.

Another satellite still under study by ESA is Solar Orbiter (SOLO). If selected, SOLO will view the poles from heliospheric latitudes higher than 30° and from close distances (60 $R_\odot$, or 0.28 AU). The launch is planned for 2017.

1.3.2 SOHO/EIT and STEREO/SECCHI/EUVI Telescopes

EIT, EUVI-A and EUVI-B are similar telescopes (Ritchey-Chretien type with a CCD camera). Although the instruments are similar with both full disk imagers, there are also several differences. Both are full disk imagers with a 1.7 $R_\odot$ field of view of EUVI covers 1.7 $R_\odot$ field of view mapped onto a 2048×2048 pixels grid with a resolution of 1.6 arcsec pixel^{-1}. While EIT has 1.5 $R_\odot$ field of view mapped onto a 1024×1024 pixels grid with a resolution of 2.5 arcsec pixel^{-1}. The time cadence for the EUVI images can be up to two minutes, whereas the cadence for EIT images varies a lot between every six hours to 60 minutes. Another difference is that the EIT, operating since 1995, has a decreased image quality compared to EUVI-A and -B. Information about these instruments can be found in Delaboudiniere et al. (1995) and Howard et al. (2008) for EIT and EUVI, respectively.

Basically, the instruments record the incident spectral radiance $L_\lambda(\Theta, \lambda)$ by means of a CCD sensor in the direction Θ corresponding to each CCD pixel $\mathbf{x} = (x, y)$ and emitted at a wavelength λ [erg cm^{-2} s^{-1} sr^1 Å] (Defise, 1999), Fig. 1.18. For a set of instrumental parameters p such as time, exposure time, filters, field of view, the resulting instrumental signal is an image $I(\mathbf{x}, p)$:

$$I(\mathbf{x}, p) = \Re(L_\lambda(\Theta, \lambda), p) \tag{1.6}$$

where $\Re$ is the global response function, which characterizes the transformation of the incident spectral radiance L_λ to the digital number (DN) recorded by the instrument. The relation 1.6 is called *calibration equation* (Defise, 1999). This transformation results from the transmission through the optical system including certain number of filters (selecting the wavelength for example) and from the conversion of the photons in the CCD sensor to an analogue electron charge and the digitization of this analogue signal by the attached electronics. A photon, which hits the area of one pixel of the CCD detector, lifts a number of electrons into the conduction band of the CCD semi-conductor, depending on the quantum efficiency. The assembled electrons are then read out pixel by pixel at the end of the exposure time and electron charge collected is within some limits proportional to the intensity at each pixel.
An estimation of $\Re$ requires the calibration of the instruments and the removal of instrumental effects. IDL routines such as *secchi_prep.pro* and *eit_prep.pro* for STEREO/SECCHI and

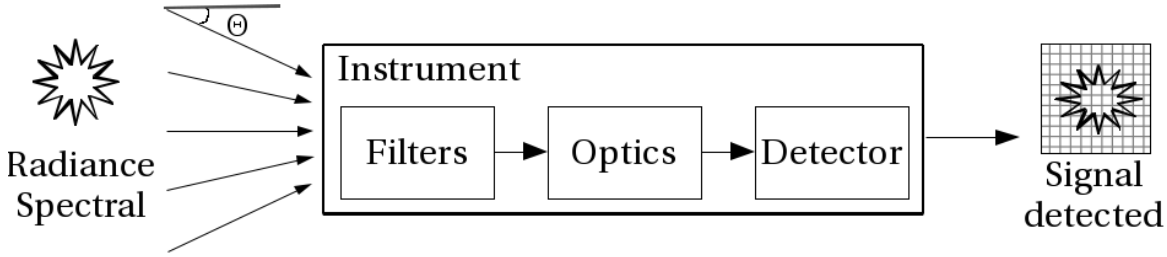

Figure 1.18: Simplified sketch of the conversion of the radiance spectral into an instrumental signal through an imager instrument such as EIT and SECCHI. A description of the EIT instrument is given by Delaboudiniere et al. (1995) before the starting of the mission and then update by Moses et al. (1997) after the launch. Instrumental performances and the characterization of the instrumental response is developed by Defise (1999). Likewise, the instrument SECCHI is described in Howard et al. (2008).

SOHO/EIT instruments respectively (in SolarSoft, Freeland and Handy, 1998), provide this image calibration procedure. For EIT, the instrumental effects that need to be taken into account have been described by Delaboudiniere et al. (1995) before the launch of the mission and were updated by Moses et al. (1997) after the launch. The instrumental effects on SECCHI images are described in Howard et al. (2008).

After applying the flat-fielding, bias subtraction and calibration procedure to an image, different types of noise still affect the signal. First there are the types of noise due to the CCD camera. The most important are these ones,

Photon noise results from the inherent statistical variation in the rate of photons incident on the CCD detector. The probability of k photons arriving in a given time interval T follows a Poisson distribution $P(k) = \mu^k e^{\mu}/k!$ with a mean number μ of photons proportional to the exposure time T. If I is the intensity in the signal the Poisson, distribution gives the signal's fluctuations by the standard deviation $\sigma = \sqrt{I}$. (This noise is also called shot noise.)

Read-out noise consists of two inseparable components Howell: First is generated by the CCD electronics when a very small packet of charge is measured. Second is the conversion from analog signal to digital number (also known as "digitization noise"). It affects all the image and is independent of the exposure time. It becomes dominant when the signal is weak, for example in the off-disk part or for short exposure times. It follows usually a Gaussian distribution and has a constant variance of few DN per pixels (about 1.6 DN for EIT data, Defise, 1999).

Thermal noise results from the statistical variation in the number of electrons thermally generated within the structure of the CCD detector. The generation rate of thermal electrons at a given CCD temperature is referred to as dark current. A low operational temperature of the detector reduces the dark current and the thermal noise can be neglected.

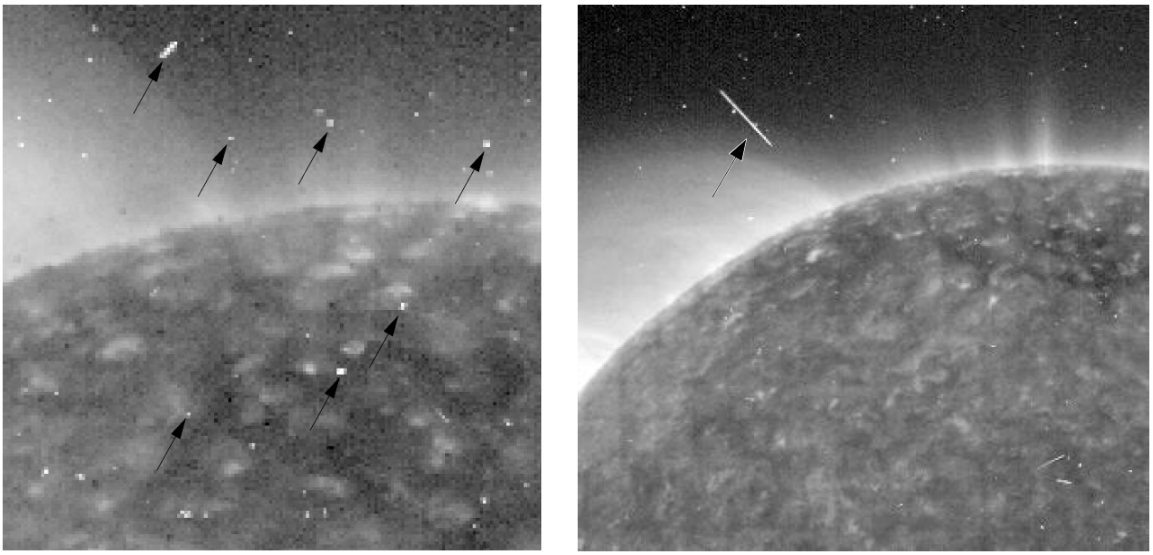

(a) (b)

Figure 1.19: Example of cosmic ray hits on an image (SOHO/EIT 284 Å). Depending on the incident angle to the CCD normal plane, cosmic ray hits form an elongated trace on the image Jacques (2004).

Cosmic ray hits. Cosmic rays can also deteriorate the quality of the image. They are relativistic particles, mainly protons or electrons some of them are generated by the Sun, while others originate from other stars. A cosmic ray signal on a CCD is typically localized at a random location on few neighboring pixels and can reach high intensity. If the angle of incidence to the CCD normal plane is near 90 degree, the cosmic ray hit may form an elongated trace on the image. Normally they do not persist in subsequent images, Fig. 1.19.

There are two other image deficiencies, which locally smooth the image and can affect further analysis:

Blurring from the Point-Spread-Function (PSF). The PSF describes the response of a point source transmitted through an optical system. Ideally, the PSF is a δ-Dirac function. In practice, the PSF response cannot be more localized than the bounds imposed by the refraction limit. Moreover, the PSF often has a low, far-reaching tail due to stray light. Its effect on the image is to blur the signal and to lower the contrast.

Compression effect. Images from SECCHI instrument are compressed with ICER, a lossless compression method based on discrete wavelet transform. It affects the Poisson-noise statistics by adding an aliasing effect. See Fig. 1.20 (a).

A final instrumental effect are data recording gaps. E.g., EIT suffers from unstable telemetry: The image is transmitted by blocks of 32×32 pixels and reconstructed after reception on the ground. Unfortunately, some few blocks are lost on the way and produce an image that cannot be reconverted completely, see Fig. 1.20 (b).

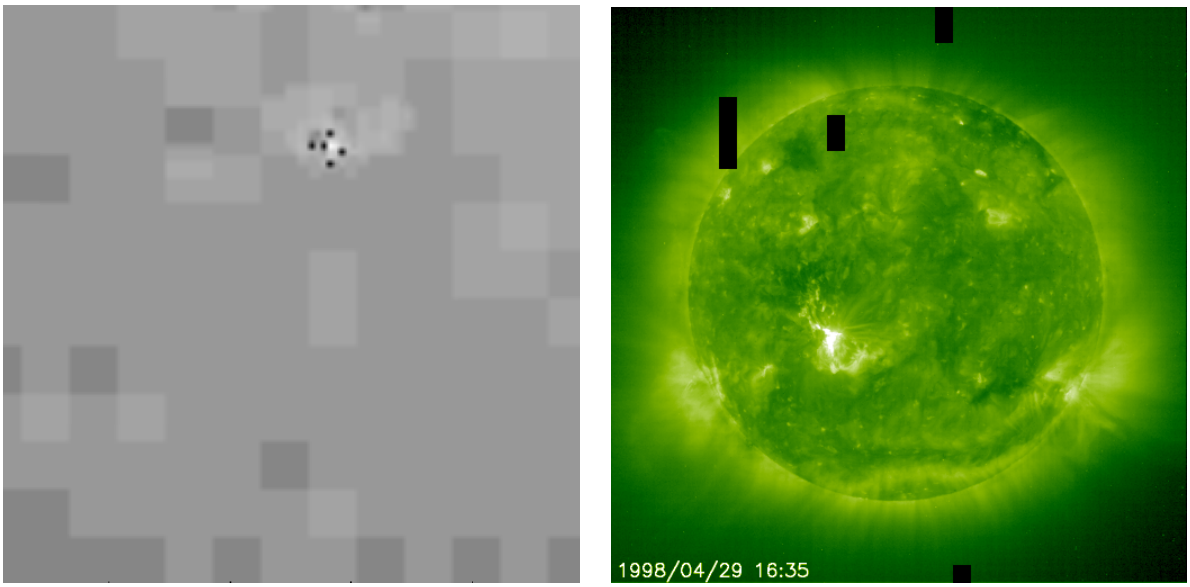

(a) (b)

Figure 1.20: (a) Typical example from ICER compression. Zoom into the off-disk part of an STEREO/EUVI image showing a cosmic ray hit surrounded by the aliasing effect introduced by the compression. (b) Image SOHO/EIT taken the 29th of April 1998 at 195 Å. This image contains 9 missing boxes of 32×32 pixels size.

All these noise effects have to be taken into account while interpreting the image and while choosing an appropriate image analysis tools.

1.3.3 Camera Model

The relation between the images taken by the SOHO/EIT and STEREO/SECCHI/EUVI Telescopes and the 3D world is usually defined in terms of a camera model (e.g., Hartley and Zisserman, 2004). Since in solar physics the object of observation is very far away, the pinhole model is a good approximation to the camera model used for solar observations. The geometry of a pinhole camera model is illustrated in Fig. 1.21. It consists of an *image plane* spanned by the edge vectors $(\mathbf{h}, \mathbf{v})$ and the image center C. The *optical axis* $\mathbf{e}_{opx}$ is normal to this plane passing through the image center C. This optical axis corresponds to the pointing of the telescope. The optical axis $\mathbf{e}_{opx}$ with the the edge vectors $(\mathbf{h}, \mathbf{v})$ defined the attitude of the telescope. The distance between the image plane and the optical center is the focal length f of the camera. The focal length defines the scale factor with, which 3D objects are projected into the image. An 3D object observed at an angle α off the optical axis is mapped into the image at a distance,

$$\sqrt{x^2 + y^2} = f \tan\alpha \, .$$

from the image center (see, Fig. 1.21). In our case α is always small and we can simplify $\tan\alpha \approx f\alpha$. According to Fig. 1.21, a pixel at (x, y) in the image space, $\mathbb{I}^2$, is mapped in the affine

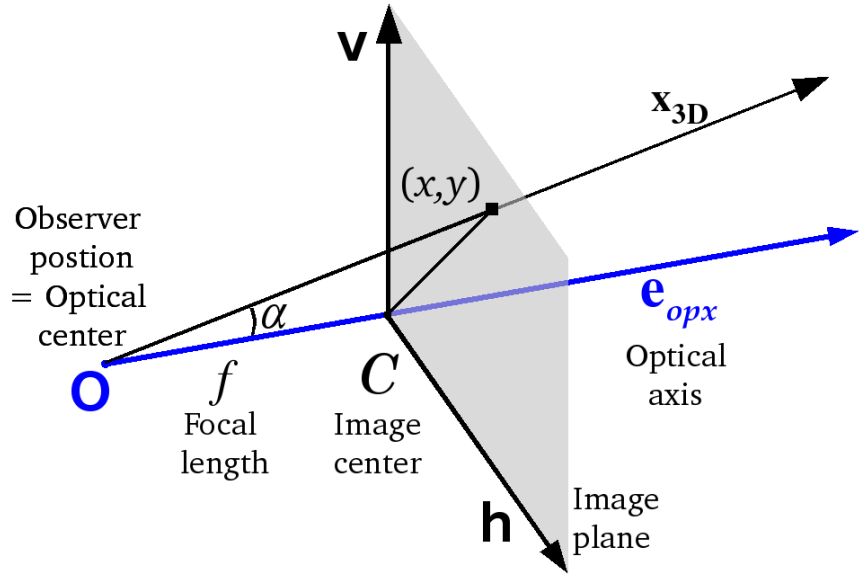

Figure 1.21: Geometry of a pinhole camera model.

space of line-of-sight vectors $\mathbf{e}_{3D}$ by, (note $\mathbf{e}_{opx}$, $\mathbf{h}$ and $\mathbf{v}$ are all unit vectors)

$$\begin{aligned} \mathbb{I}^2 \to \mathbb{R}^3 : (x,y) \to \mathbf{e}_{3D}(x,y) &= \mathbf{e}_{opx} + \frac{x\mathbf{h} + y\mathbf{v}}{\sqrt{x^2+y^2}} \tan\alpha \\ &\approx \mathbf{e}_{opx} + \frac{x\mathbf{h} + y\mathbf{v}}{\sqrt{x^2+y^2}}\alpha = \mathbf{e}_{opx} + \frac{x\mathbf{h} + y\mathbf{v}}{f} \end{aligned} \tag{1.7}$$

If x and y are given in pixels, $\dfrac{\alpha}{\sqrt{x^2+y^2}}$ is the image plate scale Λ in radian per pixel instead of $\dfrac{1}{f}$. Finally, the ray in 3D space associated with image pixel (x,y) is given by

$$\mathbf{x}_{3D}(s) = \mathbf{O} + s\left[\mathbf{e}_{opx} + (x\mathbf{h} + y\mathbf{v})\Lambda\right] \tag{1.8}$$

where $\mathbf{O} \in \mathbb{R}^3$ is the optical center position and $s \in \mathbb{R}^+$ represents the variable distance along the ray. And $\mathbf{O}$ can be identified with the spacecraft position.

Chapter 2
Motivation and Goals of the Thesis

This work started in January 2008 during a period of minimum of solar activity. At this time, coronal holes were located at the poles, which is the most favorable situation for observing polar plumes. Moreover, in 2007-2008, the two STEREO spacecraft began to have a suitable separation angle providing, for the first time, observations of the Sun from two different viewpoints simultaneously, which makes 3D stereoscopic reconstruction of coronal objects possible. The data collected by the STEREO spacecraft during this time is therefore ideally suited to study polar plumes in EUV and their 3D structure.

Motivation

Plume formation and contribution of plumes to other phenomena in the solar corona are still under debate. The knowledge of the polar plume 3D geometry would greatly help the understanding of some of the affected physical processes:

- Measuring the outflow velocity in plumes is of great interest to understand their contribution to the fast solar wind. Acknowledging the 3D plume orientation enables the estimation of the outflow velocity from Doppler measurements from tracking density irregularities in the plane of the sky.

- Determining the magnetic structures at the plume foot-points and their locations with regard to the chromospheric network helps to study the formation and evolution of plumes. By reconstructing the 3D geometry, it becomes possible to trace the plume axis back to its foot-point on the surface of the Sun where the magnetic properties of plume foot-points can be identified.

- Several types of plume cross section shape are proposed in the literature: plume network, curtain plume and beam plume. To determine the shape it is essential to reconstruct their 3D geometry.

- Plumes are optically thin, so that their observations are an integral along the line of sight. In order to study their temporal behavior, it is important to know their 3D axis location especially for the plumes showing an intermittent evolution.

- The identification of relations between plumes and other solar phenomena such as bright points, jets, network edges, coronal holes, can be easily misled by a wrong location of both objects. 3D reconstruction can help to confirm the spacial relation between different objects.

The 3D reconstruction of polar plumes is not straightforward. Although plumes appear to be brighter in coronal images and are rooted in solar coronal holes, they are quite diffuse and cannot be associated closely to a foot-point even if it lies on the visible part of the solar surface. Plumes and inter-plume regions are not sharply bounded. Therefore advanced methods to identify them and to reconstruct their 3D shape need to be elaborated.

Advanced Image Processing Tools

In solar physics, automated image processing techniques have become unavoidable for many observational studies. Aschwanden (2010) lists a number of reasons for this development. One reason is the significant increase of the data quantity: SOHO/EIT produces approximately one image (1024×1024 pixels) every 20 minutes at one wavelength while an instrument more than 10 years younger, SDO/AIA, produces an image (4096×4096 pixel) every 10 seconds at one wavelengths. Another reason that particularly motivated our work is the objectivity in the analysis. Automated methods facilitate a perfect repetition of the procedure on each image independently and with high precision. For studying time series with statistical significance, automated techniques based on sophisticated computer algorithms are also indispensable.
As already said, plumes are faint objects and coronal images have several types of noise and artifacts. An automatic plume detection is not straightforward and requires advanced image processing tools.

Advanced 3D Reconstruction Tools

Studies of the 3D structure of polar plumes reported in the literature used different image processing techniques. Each of these techniques has to cope with the difficulty that plumes are numerous and diffuse. Llebaria et al. (1998) elaborated a time intensity diagram with SOHO/EIT and SOHO/LASCO data. In the resulting diagram, plumes are not well distinguishable. Barbey et al. (2008) proposed tomographic techniques using SOHO/EIT data and encountered, additionally, the problem of real-time evolution of plumes and the differential rotation of the Sun. Finally Feng et al. (2009) traced the 3D orientation of plumes using STEREO/EUVI data and stereoscopy, which required a good identification of plumes in different images.

Goals

The purpose of this thesis is to study polar plumes in EUV images taken during the minimum of solar activity from three different spacecrafts, STEREO-A, B and SOHO.
As a first step, we automatically identify the projected plumes in a series of images. We develop a tool based on the Hough and the wavelet transform, which considers the finite width of the

plume and the low plume signal to noise ratio. With this tool we analyze the temporal evolution of the average orientation of the plumes over a time range of about a year.
Secondly, we identify the 3D geometry from three different view directions. We use two well elaborated 3D reconstruction tools: tomography and stereoscopy. We adapted these tools for polar plume objects, modifying them to take account of the differential rotation of the Sun and the data from the three spacecrafts.
Finally, we discuss the plume cross section shapes in relation to their temporal evolution, their location with regard to coronal holes and other events such as jets.

Research program of the present thesis

The structure of this thesis is as follows. In Part II, image processing and 3D reconstruction techniques are introduced. In order to extract plume structures from 2D EUV images, an automated plume detection tool is designed (Chapter 3). Based on the automated plume detection tool, stereoscopic and tomographic reconstruction techniques are elaborated for plume structures (Chapter 4). In Part III, the plume extraction and 3D plume reconstructions are performed by using the real EUVI/EUVI and SOHO/EIT data. The temporal evolution of the projected plume orientation is analyzed from 2D EUV images and discussed in Chapter 5. By combining the 3D geometry with plume observations over an extended time range, plume lifetime, location and cross section shape are obtained and discussed in Chapter 6. In the end, the final part of this thesis summarizes the main results and gives an outlook for future work (Part IV).

Part II

Image Processing & 3-D Reconstruction Techniques

Chapter 3
Image Processing Tools

In this chapter, we describe some techniques to process STEREO/EUVI and SoHO/EIT images. The purpose is to establish a tool capable of automatically identifying plumes in a series of EUV images. A suitable tool is the *wavelet transform*, described in Section 3.2. In contrast to classical detection methods, it allows the simultaneous identification of the shape, location and orientation of an object in the image. Another method is the *Hough transform*, described in Section 3.3. This transform is particularly suited for extracting straight lines from an image. Plumes are faint, straight features in EUV images with a variable width. The basic Hough transform is not well adapted to finite-width objects. Therefore, we propose here to combine the Hough transform with the wavelet transform, which we call *Hough-wavelet transform*. It is described in Section 3.4.

In this chapter, we present the main idea of each method and give a series of examples to show how sensitive and robust each method is. However, for more mathematical details, we refer the reader to Appendix A and to the references given in the text.

3.1 The Image as a 2D Signal

Here, we consider an image as a 2D signal represented by a function f defined on the real plane $\mathbb{R}^2$: $f : \mathbb{R}^2 \to \mathbb{R}$. The signal f is said to have *finite energy* if $f \in L^2(\mathbb{R}^2)$ where L^2 is the Hilbert space and L^n is defined as

$$L^n(\mathbb{R}^2) = \{f : \mathbb{R}^2 \to \mathbb{R} \; ; \; \|f\|^n = \left(\int_{\mathbb{R}^2} |f(\mathbf{x})|^n \, d^2\mathbf{x} \right)^{1/n} < \infty \} \, , \tag{3.1}$$

for $n = 1, 2$. By working in the Hilbert space $L^2(\mathbb{R}^2)$, we have access to all facilities provided by the existence of an inner product. This inner product is

$$\forall f, g \in L^2(\mathbb{R}^2), \quad \langle f|g\rangle = \int_{\mathbb{R}^2} f(\mathbf{x}) g(\mathbf{x}) \, d^2\mathbf{x}, \quad \langle f|f\rangle = \|f\|^2 \; . \tag{3.2}$$

A simple example of a 2D signal is a grayscale image where each position $\mathbf{x} = (x, y)$ is associated with a value called intensity.
The 2D signal f can be decomposed by the Fourier transform into its sine and cosine components.

In this way, the signal f is converted from its spatial domain to its Fourier domain in which each point represents a particular frequency contained in the spatial domain. This transformation is formally given by

$$\widehat{f}(\mathbf{k}) = \int_{\mathbb{R}^2} f(\mathbf{x})\ e^{-i\mathbf{k}\cdot\mathbf{x}}\ d^2\mathbf{x}\,, \tag{3.3}$$

$$f(\mathbf{x}) = \frac{1}{2\pi}\int_{\mathbb{R}^2} \widehat{f}(\mathbf{k})\ e^{i\mathbf{k}\cdot\mathbf{x}}\ d^2\mathbf{k}\,, \tag{3.4}$$

with $\mathbf{x} = (x, y) \in \mathbb{R}^2$ in spatial domain and $\mathbf{k} = (k_x, k_y) \in \mathbb{R}^2$ in Fourier domain.

In practice, 2D signals are images, which are discrete functions f_{nm} defined on a finite grid $[0, N] \times [0, M]$ and bounded positive $0 \leq f_{nm} \leq B$, for $0 < B < \infty$. For a sampling period $T \in \mathbb{R}_0^+$ identical in x and y direction, the function f_{nm} is discretized on the set of points $\mathbf{x}_{nm} = (x_{nm}, y_{nm})$ with $0 < n < N$ and $0 < m < M$ such as

$$f_{nm} = \int_{\mathfrak{P}(\mathbf{x}_{nm})} f(\mathbf{x})\, d^2\mathbf{x}\,,$$

where $\mathfrak{P}(\mathbf{x}_{nm}) = \{\mathbf{x}\,;\ |x - x_{nm}| < \frac{T}{2}, |y - y_{nm}| < \frac{T}{2}\}$ is the support of a pixel. Under certain conditions of discretization[1] (See Mallat, 1998), the inner product (3.2) becomes

$$\langle f|g\rangle = T^2 \sum_{(n,m)\in\mathbb{Z}^2} f(\mathbf{x}_{nm})g(\mathbf{x}_{nm})\,.$$

The Fourier transform is also discretized,

$$\widehat{f_{kl}} = \sum_{n=0}^{N-1}\sum_{m=0}^{N-1} f_{mn}\ \exp\left(-i\,\frac{2\pi}{N}\,(km + ln)\right)\,, \tag{3.5}$$

$$f_{mn} = \frac{1}{N^2}\sum_{k=0}^{N-1}\sum_{l=0}^{N-1} \widehat{f_{kl}}\ \exp\left(i\,\frac{2\pi}{N}\,(km + ln)\right)\,. \tag{3.6}$$

This transformation is performed by the Fast Fourier Transform (FFT). For N^2 values of f_{mn} or $\widehat{f_{kl}}$ the FFT reduces the number of operations to $O(N^2 \log^2 N)$ instead of $O(N^4)$ for the usual discrete calculation.

A region of an image is said to be regular if the intensity within this region contains smooth variations, as opposed to singularities within an image that are sharp variations in intensity. The degree of regularity of an image f can be measured by computing the pointwise *Hölder exponent* $h(\mathbf{x}_0)$ at each point $\mathbf{x}_0$ (Mallat, 1998). This exponent gives precisely the degree of regularity: a function f is said to be *Hölder regular* at $\mathbf{x}_0$ if

$$|f(\mathbf{x}) - f(\mathbf{x}_0)| \sim \|\mathbf{x} - \mathbf{x}_0\|^{h(\mathbf{x}_0)}\,, \tag{3.7}$$

[1] The observed images need to be well discretized with regard to the Shannon-Nyquist sampling theorem.

where $\|\mathbf{x}\| = \sqrt{x^2 + y^2}$ and for $\mathbf{x}$ in the neighborhood of $\mathbf{x}_0$ such that $\|\mathbf{x} - \mathbf{x}_0\| < \epsilon$. The larger the $h(\mathbf{x}_0)$, the more regular is the image around $\mathbf{x}_0$. For example, a n times differentiable function can be approximated by a polynomial, P_n, obtained from the 2D Taylor series of f around $\mathbf{x} = \mathbf{x}_0$,

$$f(\mathbf{x}) = f(\mathbf{x}_0) + \frac{\partial f(\mathbf{x}_0)}{\partial x}(x - x_0) + \frac{\partial f(\mathbf{x}_0)}{\partial y}(y - y_0) + \cdots + O(\|\mathbf{x} - \mathbf{x}_0\|^n) .$$

For this function, $h(\mathbf{x}_0) \geq n$. Conversely a function locally similar to a Dirac function, and therefore not differentiable, gives $h(\mathbf{x}_0) = 0$. So the smaller $h(\mathbf{x}_0)$, the more singular is the image around $\mathbf{x}_0$. Appendix A.1 provides a precise definition of $h(\mathbf{x}_0)$.

3.2 Continuous Wavelet Transform

3.2.1 Family of Wavelets and Wavelet Transform

An image f of finite energy, as defined in Section 3.1, can be analyzed by comparing it with a known function called a *wavelet*. This wavelet acts on the image like a probe, scanning the image and zooming into it (Fig. 3.1). We consider only the case of real-valued wavelets. In this section, we give a brief overview on wavelets based on the work of Torrésani (1995), Mallat (1998) and Antoine et al. (2004). We consider only the case of real-valued wavelets.

A wavelet is a function $\psi(\mathbf{x}) \in L^2(\mathbb{R}^2)$ with a wave-like oscillation, which decays sufficiently quickly towards infinity and has zero mean,

$$\widehat{\psi}(0) = 0 \quad \Leftrightarrow \quad \int_{\mathbb{R}^2} \psi(\mathbf{x})\, d^2\mathbf{x} = 0.$$

A strict definition is given in Appendix A.2. A family of wavelets $\psi_{\mathbf{b},a,\theta}$ is generated from ψ by elementary operations, i.e., translation by $\mathbf{b} \in \mathbb{R}^2$, rotation by an angle $\theta \in [0, 2\pi[$ and dilatation by a factor $a \in \mathbb{R}_0^+$ (Fig. 3.2). These three elementary transformations yield the family of wavelets,

$$\psi_{\mathbf{b},a,\theta}(\mathbf{x}) = \frac{1}{a}\psi\left(\frac{r_\theta^{-1}(\mathbf{x} - \mathbf{b})}{a}\right). \tag{3.8}$$

In Fourier, the family of wavelets becomes,

$$\widehat{\psi}_{\mathbf{b},a,\theta}(\mathbf{k}) = a\, \widehat{\psi}\left(a\, r_\theta^{-1}(\mathbf{k})\right)\, e^{-i\mathbf{b}\cdot\mathbf{k}} \quad . \tag{3.9}$$

The image is then analyzed with a wavelet function:

Definition 3.2.1. *For a known wavelet function ψ, the* continuous wavelet transform *of an image $f \in L^2(\mathbb{R}^2)$ is the inner product (3.2) of f and $\psi_{\mathbf{b},a,\theta}$ seen as a function of $(\mathbf{b}, a, \theta)$:*

$$W_\psi[f](\mathbf{b}, a, \theta) = \langle \psi_{\mathbf{b},a,\theta} | f \rangle = \frac{1}{a^{3-n}} \int_{\mathbb{R}^2} \psi\left(\frac{r_\theta^{-1}(\mathbf{x} - \mathbf{b})}{a}\right) f(\mathbf{x})\, d^2\mathbf{x} , \tag{3.10}$$

$$= \left\langle \widehat{\psi}_{\mathbf{b},a,\theta} | \widehat{f} \right\rangle = \frac{1}{a^{1-n}} \int_{\mathbb{R}^2} \widehat{\psi}\left(a\, r_\theta^{-1}(\mathbf{k})\right)\, e^{-i\mathbf{b}\cdot\mathbf{k}}\ \widehat{f}(\mathbf{k})\, d^2\mathbf{k} , \tag{3.11}$$

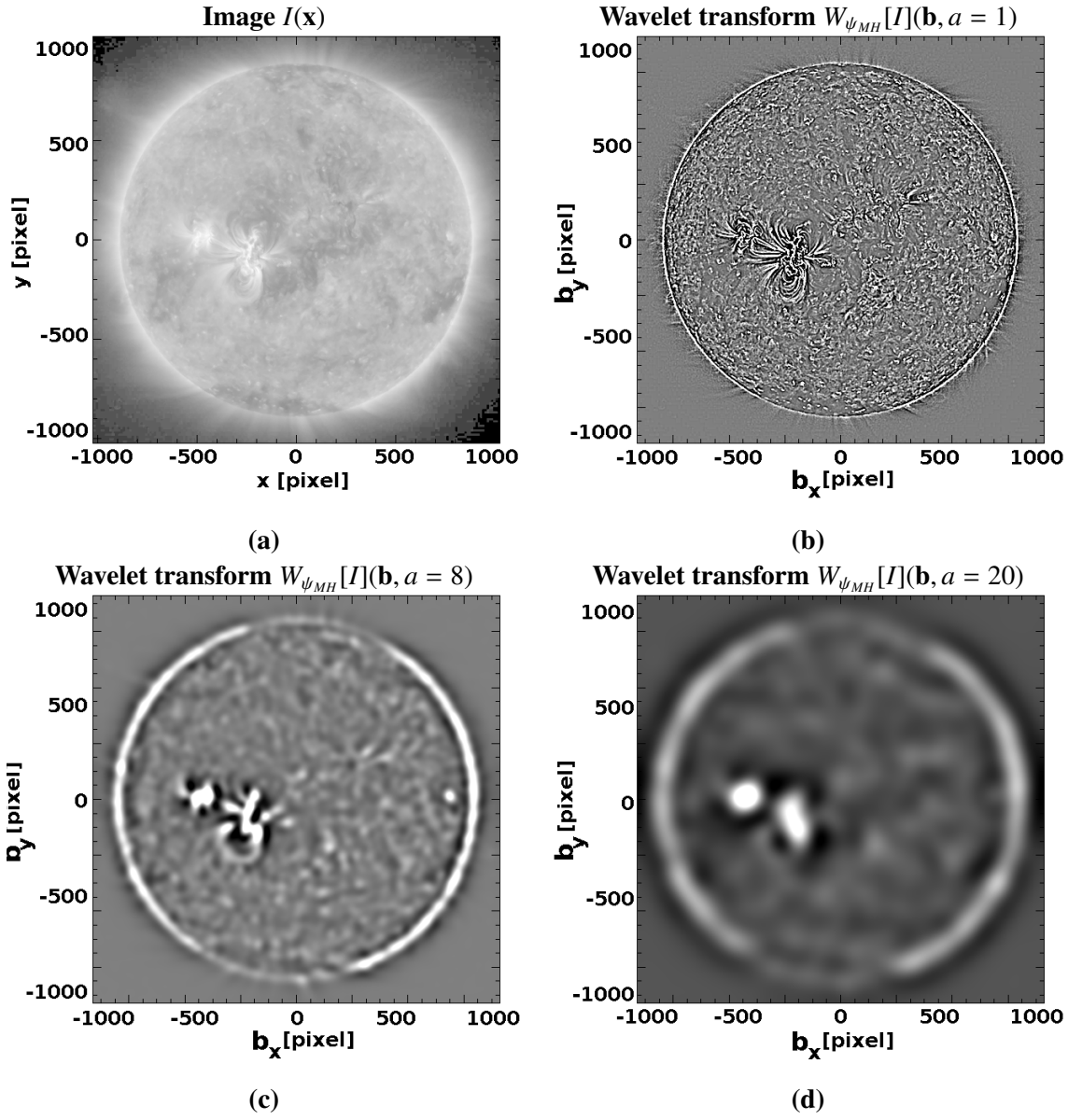

Figure 3.1: Wavelet transform with the Mexican Hat wavelet: (a) The original image, STEREO/EUVI-A (1st of May 2007 at 171Å). (b)-(c) Wavelet transform for the scale a =1, 8 and 20.

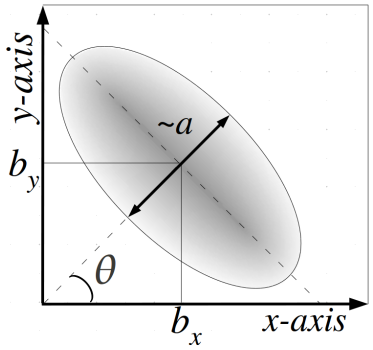

Figure 3.2: Wavelet transform parameters $(\mathbf{b}, a, \theta)$ in the image domain (x, y).

where $\psi_{\mathbf{b},a,\theta}$ is the family of wavelets generated from ψ and $n = 1$ or 2 in normalization L^1 and L^2 respectively.

The choice of $n = 1$ has the advantage of giving more weight to the small scales. It produces an enhancement at the high frequency part of the image, and thus emphasizes its singularities. For mathematical reasons, $n = 2$ normalization is more often selected.
Three main properties of the continuous wavelet transform are ,

Proposition 3.2.2. *For a wavelet, ψ, any image, $f \in L^2(\mathbb{R}^2)$, satisfies*

$$(1) \qquad f(\mathbf{x}) = \frac{1}{c_\psi} \int_{\mathbb{R}^2} \int_{\mathbb{R}_0^+} \int_0^{2\pi} \psi_{\mathbf{b},a,\theta}(\mathbf{x}) W_\psi[f](\mathbf{b}, a, \theta)\, d^2\mathbf{b}\, \frac{da}{a^3}\, d\theta\,,$$

$$(2) \qquad \int_{\mathbb{R}^2} \int_{\mathbb{R}_0^+} \int_0^{2\pi} W_\psi[f](\mathbf{b}, a, \theta) d^2\mathbf{b}\, da\, d\theta = 0\,,$$

$$(3) \qquad \int_{\mathbb{R}^2} |f(\mathbf{x})|^2\, d^2\mathbf{x} = \frac{1}{c_\psi} \int_{\mathbb{R}^2} \int_{\mathbb{R}_0^+} \int_0^{2\pi} \left|W_\psi[f](\mathbf{b}, a, \theta)\right|^2\, d^2\mathbf{b}\, \frac{da}{a^3}\, d\theta\,.$$

where c_ψ is a constant and $0 < c_\psi < +\infty$.

The constant c_ψ is given in Appendix A.2, and it is called the admissibility condition. The first property ensures a successful inverse wavelet transform, which guarantees that during a transformation no information is added or lost from the original image. The second property means that the integral over all coefficients of the wavelet transform vanishes, which is trivial since ψ has zero integral. The last property is the Plancherel formula showing that there is an isometry from the space of images into the space of transforms. The proof of properties (1) and (3) can be found in, e.g., Torrésani 1995 and Antoine et al. 2004.

There are several functions, which can be chosen as wavelets. One characteristic of a wavelet is the number of vanishing moments n:

$$\int_{\mathbb{R}^2} \psi(\mathbf{x})\, x^\alpha\, y^\beta\, d^2\mathbf{x} = 0 \quad \text{for} \quad 0 \le \alpha + \beta \le n\,. \tag{3.12}$$

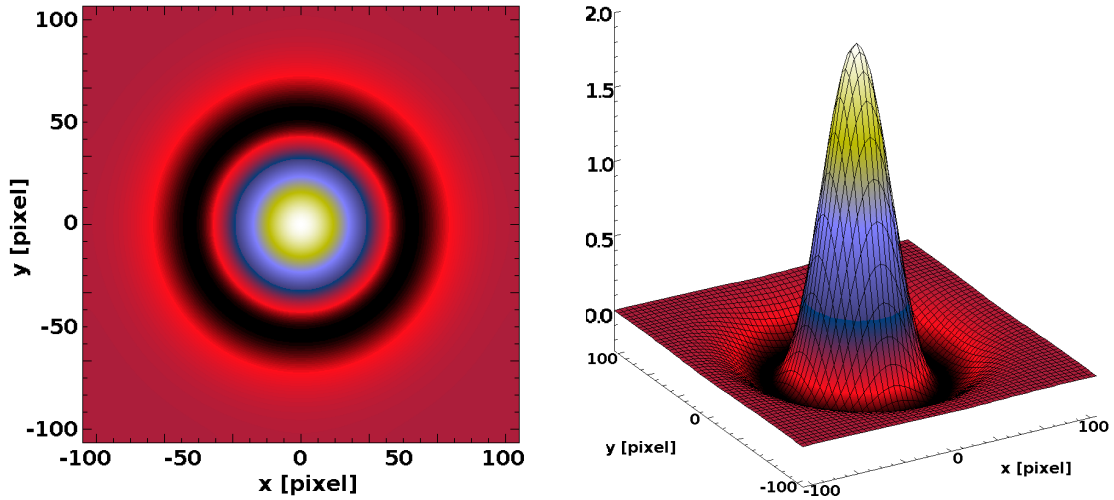

Figure 3.3: Mexican hat wavelet for a scale a =8. (a) An image representation where the color goes from black to white going from -0.3 to 2.0. (b) A 3D representation of the wavelet.

This means that the wavelet coefficients vanish for polynomials of degree smaller or equal to n. For an image, which can be decomposed into a Taylor series, the wavelet is insensitive to all terms of degree $\leq n$ (since the wavelet transform is linear). We choose a wavelet, which has two vanishing moments and therefore is sensitive to the polynomial terms of degree $n > 2$. It is the *Mexican Hat wavelet* and is defined as the Laplacian of a Gaussian:

$$\psi_{MH}(\mathbf{x}) \equiv -\frac{\partial^2}{\partial \mathbf{x}^2} e^{-\frac{\|\mathbf{x}\|^2}{2}} = (2 - \|\mathbf{x}\|^2)\, e^{-\frac{\|\mathbf{x}\|^2}{2}}, \tag{3.13}$$

$$\widehat{\psi}_{MH}(\mathbf{k}) = \|\mathbf{k}\|^2\, e^{-\frac{\|\mathbf{k}\|^2}{2}}. \tag{3.14}$$

Fig. 3.3 shows an example of this wavelet for a scale a =8. Fig. 3.4 (b)-(a) show the wavelet coefficients evaluated with the Mexican Hat wavelet for an image composed of a Gaussian peak and a background following a parabola in x-direction (Fig. 3.4 (a)). The background gives no contribution to the wavelet coefficients since it has degree $n = 2$. While the Gaussian peak, which has a degree $n > 2$, is well detected by the wavelets transform. In this example, the inverse wavelet transform reconstructs only the Gaussian peak, the rest is set as background equal to zero.

The Mexican Hat is an efficient wavelet for a fine pointwise analysis. It is easy to compute numerically since the function and its Fourier transform are analytic and real. Also the Mexican Hat is essentially localized in a disk. This Mexican Hat has been used in solar physics for, e.g., estimating the size of super granules in Delouille et al. (2005).

In Fig. 3.1, we give an example of the wavelet transform with the Mexican Hat on a EUV image of the corona for the scales a =1,8 and 20. At small scales, the wavelet detects all thin structures

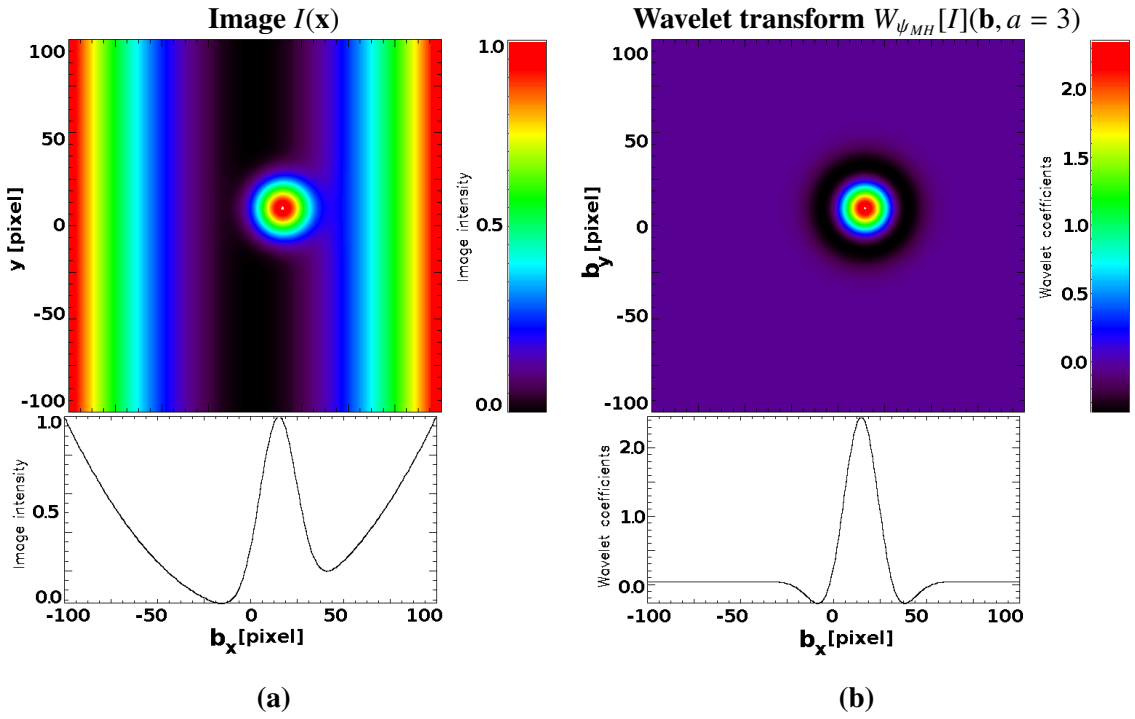

Figure 3.4: (a) An image (256×256 pixel) composed of a Gaussian peak on a background following a parabola in X-direction. Below a cut at $Y = 12$. (b) The result of the wavelet transform with the Mexican Hat wavelet for the scale $a = 5$. Below a cut at $b_Y = 12$ showing that the Mexican wavelets is blind to polynomials of degree ≤ 2.

of the corona, at larger scales the wavelets detect the limb, larger loops and small active regions, at even larger scales, only the main active regions are detected.

3.2.2 Implementation

In practice, the image that we are studying is an image defined on a grid $[0, N] \times [0, N]$. Integrations are replaced by Riemann summations and Fourier transforms are replaced by discrete FFTs (Fast Fourier Transforms). We calculate the wavelet transform in Fourier space (3.11), i.e.

$$W_\psi[f](\mathbf{b}, a, \theta) = \int_{\mathbb{R}^2} \widehat{\psi}\left(a\, r_\theta^{-1}(\mathbf{k})\right)\, e^{i\mathbf{b}.\mathbf{k}}\, \widehat{f}(\mathbf{k})\, d^2\mathbf{k}\,, \tag{3.15}$$

which is simply the inverse Fourier transform of $\widehat{\psi}\left(a\, r_\theta^{-1}(\mathbf{k})\right)\, \widehat{f}(\mathbf{k})$, where the wavelet in Fourier space is given by (3.9). This reduces the number of operations compared to a wavelet transform in the spatial domain from $O((N+1)^4 N_a N_\theta)$ to $O((N+1)^2 N_a N_\theta \log(N+1))$. For the Mexican Hat wavelet, (3.15) becomes

$$W_{\psi_{MH}}[f](\mathbf{b}, a) = \int_{\mathbb{R}^2} \|a\mathbf{k}\|^2\, e^{-\frac{\|a\mathbf{k}\|^2}{2}}\, e^{i\mathbf{b}.\mathbf{k}}\, \widehat{f}(\mathbf{k})\, d^2\mathbf{k}\,. \tag{3.16}$$

Because the FFT assumes a periodic image, the above approach produces *edge effects*, whenever the wavelet is shifted so close to the boundary of f that the wavelet support reaches beyond this boundary. This effect increases with the scale a. We minimize this effect by restricting the shift $\mathbf{b}$ so that the numerical support of the wavelet lies always inside the image.

The finite size and resolution of the image limits the range of scales, which can reasonably be applied. At small scales a, the wavelet ψ_{MH}, needs to be well resolved on the image grid. In Fourier space this is equivalent to the condition that the numerical support of $\widehat{\psi}$ is smaller than the Nyquist range of the image. We chose the following limits a_{min} and a_{max} for scale a:

$$\text{num supp}\left(\widehat{\psi}_{MH}\right) < \frac{2\pi}{N}L \qquad \Leftrightarrow \qquad a_{min}^2\left(\frac{2\pi}{N}L\right)^2 \exp\left(-\frac{1}{2}a_{min}^2\left(\frac{2\pi}{N}L\right)^2\right) < 10^{-5},$$

for $L = N$ pixels. By this test we conclude that the smallest scale that we can consider is $a_{min} = 0.64$ pixels. On the other hand, the scale a must not be chosen so large that its numerical support of ψ_{MH} is bigger than the image size.

$$\text{num supp}\left(\psi_{MH}\right) < \frac{N}{2} \qquad \Leftrightarrow \qquad \left(2 - \left(\frac{N/2}{a_{max}}\right)^2\right) \exp\left(-\frac{1}{2}\left(\frac{N/2}{a_{max}}\right)^2\right) < 10^{-5}\ .$$

By definition, the wavelet has zero mean and its Fourier transform is zero at the origin,

$$\widehat{\psi}_{MH}(0) = 0 \qquad \Leftrightarrow \qquad a_{min}^2\left(\frac{2\pi}{N}L\right)^2 \exp\left(-\frac{1}{2}a_{min}^2\left(\frac{2\pi}{N}L\right)^2\right) < 10^{-5}.$$

The numerical support of the Mexican Hat wavelet (3.13) is about 7 times the scale (see Fig. 3.3), which gives us an upper limit for choosing the scale.

3.2.3 Examples

Here we illustrate the wavelet analysis by some selected examples that we have created and then solved analytically. In order to judge the suitability of this multi-scale method for detecting objects at different scales, we look at its spectrum:

$$\mu(a,\theta) \equiv \int_{\mathbb{R}^2} \left|W_\psi[f](\mathbf{b},a,\theta)\right|^2\ d^2\mathbf{b}\ . \tag{3.17}$$

This quantity has been defined for the first time in the context of the study of self-similar functions in order to detect symmetry, both in terms of dilatation and rotation (Vandergheynst, 1998; Antoine et al., 1999). Our purpose is to use it in order to calculate wavelet coefficients at different scales. Since we use an isotropic wavelet, (3.13), $\psi_{\mathbf{b},a,\theta}$ is independent of θ, hence (3.17) can be simplified by,

$$\mu(a) \quad = \quad \int_{\mathbb{R}^2} \left|W_\psi[f](\mathbf{b},a)\right|^2\ d^2\mathbf{b}\ . \tag{3.18}$$

Furthermore, the wavelet spectrum can be rewritten with the wavelet transform in Fourier space (3.11). For the Mexican Hat wavelet (3.14) this becomes

$$\begin{aligned}
\mu(a) &= \int_{\mathbb{R}^2}\int_{\mathbb{R}^2} \widehat{\psi}_{\mathbf{b},a}(\mathbf{k})\,\widehat{f}(\mathbf{k})\,d^2\mathbf{k}\int_{\mathbb{R}^2} \widehat{\psi}_{\mathbf{b},a}(\mathbf{k}')\,\widehat{f}(\mathbf{k}')\,d^2\mathbf{k}'\,d^2\mathbf{b} \\
&= \int_{\mathbb{R}^2}\int_{\mathbb{R}^2}\int_{\mathbb{R}^2} \|a\mathbf{k}\|^2\, e^{-\frac{\|a\mathbf{k}\|^2}{2}} |a\mathbf{k}'|^2\, e^{-\frac{|a\mathbf{k}'|^2}{2}} e^{i\mathbf{b}\cdot(\mathbf{k}-\mathbf{k}')}\,\widehat{f}(\mathbf{k}')\,\widehat{f}(\mathbf{k})\,d^2\mathbf{k}\,d^2\mathbf{k}'\,d^2\mathbf{b} \\
&= \int_{\mathbb{R}^2}\int_{\mathbb{R}^2} \|a\mathbf{k}\|^2|a\mathbf{k}'|^2\, e^{-\frac{\|a\mathbf{k}\|^2}{2}}\, e^{-\frac{|a\mathbf{k}'|^2}{2}}\,\frac{1}{2\pi}\delta(\mathbf{k}-\mathbf{k}')\,\widehat{f}(\mathbf{k}')\,\widehat{f}(\mathbf{k})\,d^2\mathbf{k}\,d^2\mathbf{k}' \\
&= \int_{\mathbb{R}^2} \|a\mathbf{k}\|^4\, e^{-\frac{\|a\mathbf{k}\|^4}{4}} \left|\widehat{f}(\mathbf{k})\right|^2\, d^2\mathbf{k}\,, \qquad (3.19)
\end{aligned}$$

which simplifies the calculation later.

Example Let $I(\mathbf{x})$ be an image composed of a Gaussian peak of width σ and amplitude A:

$$I(\mathbf{x}) = \frac{A}{2\pi\sigma^2}\, e^{\frac{-\|\mathbf{x}\|^2}{2\sigma^2}}, \quad \hat{I}(\mathbf{k}) = \frac{A}{\sigma}\, e^{\frac{-\sigma^2}{2}\|\mathbf{k}\|^2}.$$

This can serve as a model of a bright point; as seen in EUV images. The wavelet spectrum, is then

$$\mu(a) = \int_{\mathbb{R}^2}\int_{\mathbb{R}^2} \|a\mathbf{k}\|^4\, e^{-\frac{\|a\mathbf{k}\|^4}{4}}\,\frac{A^2}{\sigma^2}\, e^{\frac{-\sigma^4}{4}\|\mathbf{k}\|^4}\, d^2\mathbf{k} = \frac{2\pi\, a^4A^2}{\sigma^2(a^2+\sigma^2)^3}. \qquad (3.20)$$

This function has a maximum at scale $a_{\mathrm{M}} = \sqrt{2}\,\sigma$ matching the size of the Gaussian peak.

Fig. 3.5 (a) shows an example for two Gaussian peaks of width $\sigma = 1$ and 2. The normalized wavelet spectrum for these is plotted in Fig. 3.5 (b). The curves have a maximum at $a = 1.4142$ and at $a = 2.8284$ for the Gaussian peak widths $\sigma = 1$ and 2 respectively. Fig. 3.5 (c) shows the argument of the wavelet coefficients: $\arg\{\max_a[W_\psi[f](\mathbf{b},a)]\}$. Fig. 3.5 (d) displays the values of a_{M} calculated for each positions.

Example Cosmic ray hits on an EUV image are highly singular objects and are not correlated with the rest of the image. To model this, we take a 2D Dirac function $\delta(\mathbf{x})$ defined as

$$\delta(\mathbf{x}) = \lim_{\sigma\to 0}\,\frac{1}{2\pi\sigma}\, e^{\frac{-\|\mathbf{x}\|^2}{2\sigma^2}}.$$

From example with the amplitude $A = \sigma$, it is easy to see that the wavelet spectrum is

$$\mu(a) = \int_{\mathbb{R}^2} \left|W_\psi[\delta](\mathbf{b},a)\right|^2\, d^2\mathbf{b} = \lim_{\sigma\to 0}\,\frac{2\pi a^4\sigma^2}{\sigma^2(a^2+\sigma^2)^3} = \frac{2\pi}{a^2}\,. \qquad (3.21)$$

Therefore, the wavelet spectrum curve of cosmic ray hits and of Gaussian noise have the same spectral slope, both decrease as a^{-2}. At scales $a \gg$ support of a perturbation in an image, its contribution of the spectral density decreases with a^{-2} irrespective of the slope of the perturbation.

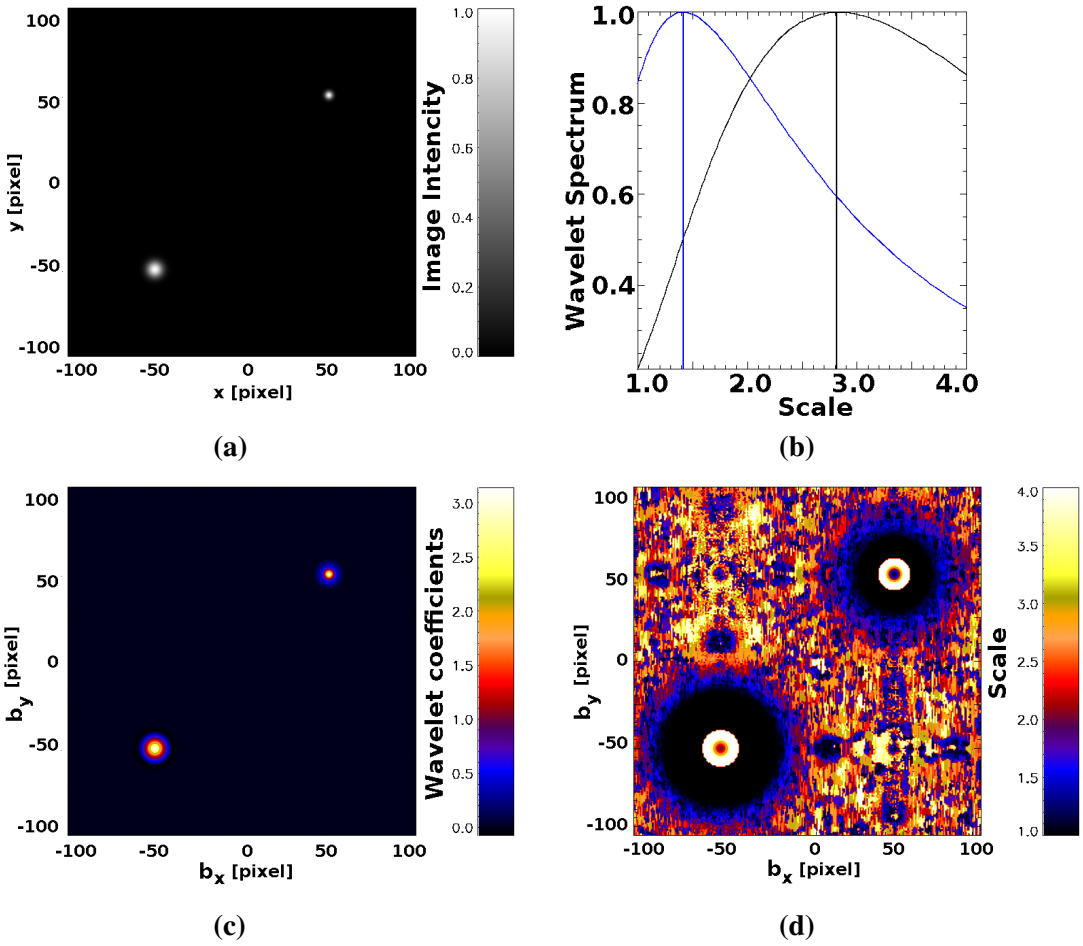

Figure 3.5: (a) Image (256×256 pixel) containing two Gaussian peaks of width $\sigma = 1$ and 2. (b) Normalized wavelet spectrum for each one of these Gaussians. The blue curve corresponds to the Gaussian of width $\sigma = 1$ and the black curve corresponds to the Gaussian of width $\sigma = 2$. (c) The wavelet transform at scale a_{M} computed separately for each pixel. (d) The value a_{M} found for each pixel.

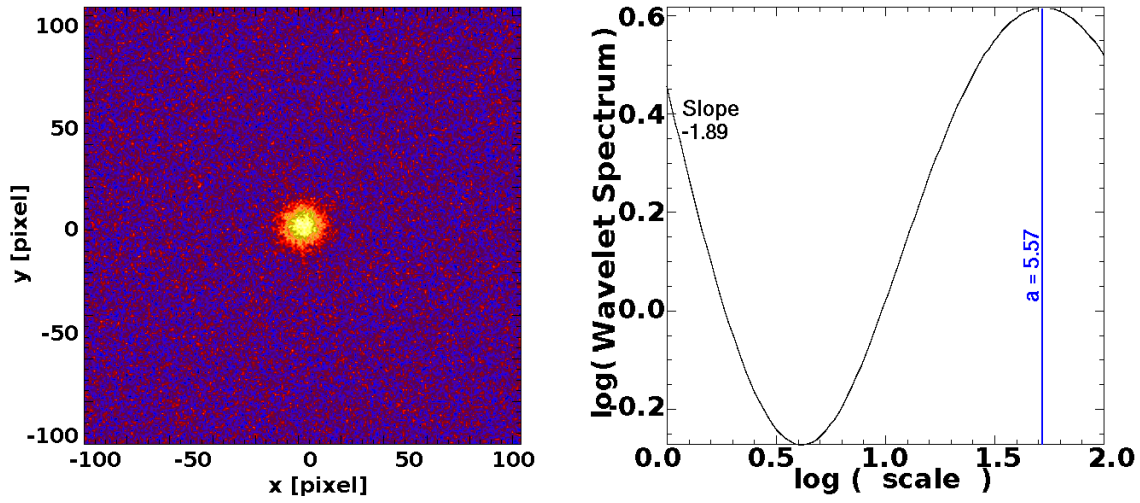

(a) (b)

Figure 3.6: (a) A Gaussian signal (256×256 pixel) with a Gaussian noise. (b) The wavelet spectrum in log scale: At small scales, the noise is dominant and the curve shows a decay while at higher scales, the Gaussian signal is dominant and the curve shows a maximum.

Example Consider Gaussian white noise signal $N(\mathbf{x})$, with expectation values of zero and variance σ^2. This noise can serve as a model for the noise in the EUV image taken by a CCD camera.
In the case of white noise $N(\mathbf{x})$ and for an isotropic and real wavelet ψ, the wavelet spectrum has a finite variance. The decay of this variance is proportional to a^{-2} (Mallat and Hwang, 1992). Indeed, $N(\mathbf{x})$ can be considered as a set of Dirac functions, which have a variance $\langle\, N(\mathbf{u})N(\mathbf{v})\,\rangle = \sigma^2\delta(\mathbf{u}-\mathbf{v})$, and the wavelet spectrum is then

$$\begin{aligned}\mu(a) &= \langle\, |W_\psi[N](\mathbf{b},a)|^2\,\rangle \\ &= \int_{\mathbb{R}^2} \sigma^2\delta(\mathbf{u}-\mathbf{v})\ \psi\left(\frac{\mathbf{x}-\mathbf{u}}{a}\right)\psi\left(\frac{\mathbf{x}-\mathbf{v}}{a}\right) d^2\mathbf{u}\, d^2\mathbf{v} \\ &= \frac{\sigma^2\|\psi\|}{a^{-2}}\,. \end{aligned} \tag{3.22}$$

Fig. 3.6 (a) shows a Gaussian signal of width $\sigma = 4$ with a Gaussian noise. The wavelet spectrum in log scale is shown in Fig. 3.6 (b). We see that at small scales, the noise is dominant and the curve shows a decay of about -2 on a $\log - \log$ plot. While at larger scales, the Gaussian signal is dominant with a peak for the scale $a = 5.57$. Fig. 3.7 shows the same procedure applied on a region outside the solar disk, which contains mainly noise and compression artifacts. At small scales, the noise is dominant, but the curve do not shows a slope > -2 on the log-log plot. We can conclude that the noise outside the solar disk is not purely a Gaussian noise, but slightly more regular. At larger scales, the compression effect shows two different optimum scales at $a = 2.50$ and at $a = 10.40$.

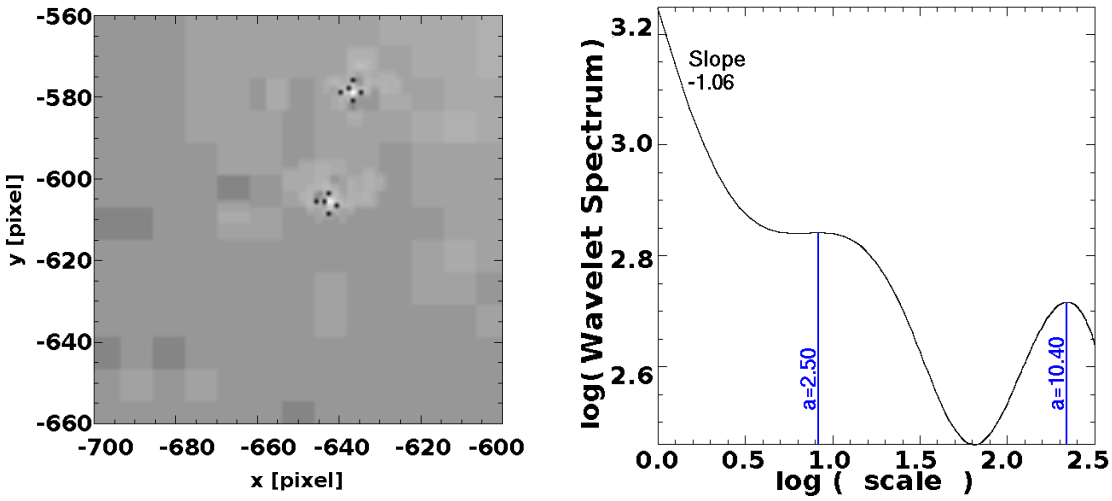

(a) (b)

Figure 3.7: (a) An off-disk subframe of the original image STEREO/EUVI-A show in Fig. 3.1 (a) with two cosmic ray hits surrounded by compression artifact. (b) The wavelet spectrum of (a) in log scale.

3.3 Hough Transform

3.3.1 Hough Transform as Wavelet Transform

Hough transform is a suitable method for extracting straight, elongated objects in an image. Basically it is the integral transform of an image along slanted lines (Toft, 1996). The location and orientation of the lines are denoted by two parameters, the inclination θ and the distance from the origin ρ as described in Fig. 3.8.

Definition 3.3.1. *For a given image* $f(\mathbf{x}) \in L^2(\mathbb{R}^2)$*, the* Hough transform $H_\delta[f](\rho,\theta)$ *is defined by*

$$H_\delta[f](\rho,\theta) \quad = \quad \int_{\mathbb{R}^2} f(\mathbf{x})\, \delta\left(\mathbf{u}_\theta \cdot \mathbf{x} - \rho\right)\, d^2\mathbf{x}, \tag{3.23}$$

where δ *is the Dirac function,* $\theta \in [0, \pi[$ *and* $\rho \in \mathbb{R}$ *and* $\mathbf{u}_\theta = (\cos\theta \;\; \sin\theta)$.

$H_\delta[f](\rho,\theta)$ can be looked upon as another image axis ρ and θ spanning the Hough space. In this work ρ is positive for $\theta \in [0, \pi/2[$ and negative for $\theta \in [\pi/2, \pi[$.

We call Hough image the coefficients of the Hough transform from new image $H_\delta[f](\rho,\theta)$. In this representation,

- a line $L_{\rho_o,\theta_o} \equiv \rho_o = x\cos_o\theta + y\sin\theta_o$ in the image (x,y)-space becomes a dot in the Hough (ρ,θ)-space at coordinate (ρ_o,θ_o). Reciprocally, all dots in the Hough space correspond to lines in the image space.

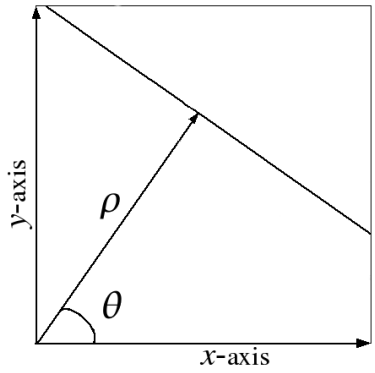

Figure 3.8: Hough transform parameters (ρ, θ) in the image space (x, y).

- a dot $(x_o, y_o) = (\rho_o \cos\theta_o, \rho_o \sin\theta_o)$ in (x, y)-space becomes a sinusoid $\rho = \rho_o \cos(\theta_o - \theta)$ in the Hough space. Reciprocally, all sinusoids in Hough space correspond to dots in (x, y)-space.

Fig. 3.9 illustrates these few cases.

In solar physics, the Hough transform was used for the first time by Llebaria and Lamy (1999) to detect plumes in white light cornagraph images, then later by Robbrecht and Berghmans (2004) for the automated recognition of coronal mass ejections (CMEs) in near real time data.

The Hough transform can be seen as a special wavelet transform (Holschneider, 1993). Consider a wavelet,

$$\psi(\mathbf{x}) = \delta(\mathbf{e} \cdot \mathbf{x}) \tag{3.24}$$

which is a δ-distribution along the line $\mathbf{e} \cdot \mathbf{x} = 0$ perpendicular to vector unit $\mathbf{e}$. Note that it is not a wavelet strictly speaking, since it does not have a zero mean. Nevertheless, the function (3.24) can be used as a wavelet by adding some additional criteria, (for more details see Holschneider, 1993). The Hough transform is then rewritten as a wavelet transform,

$$\begin{aligned} W_\delta[f](\mathbf{b}, a, \theta) &= a \int_{\mathbb{R}^2} f(\mathbf{x})\, \delta\left([r_\theta\, \mathbf{e}] \cdot \mathbf{b}\right)\, d^2\mathbf{x} \\ &= a H_\delta[f]([r_\theta\, \mathbf{e}] \cdot \mathbf{b}, \theta)\,, \end{aligned} \tag{3.25}$$

where we have defined the vector $\mathbf{u}_\theta = r_\theta\, \mathbf{e} = (\cos\theta\,, \sin\theta)$ and the parameter $\rho = [r_\theta\, \mathbf{e}] \cdot \mathbf{b}$.
The Fourier slice theorem (Natterer, 2001), gives the link between the image in Fourier transform $\widehat{f}$ and the Fourier transform of the Hough transform $\widehat{H_\delta[f]}$:

Theorem 3.3.2. (Fourier Slice Theorem) *Let $f(\mathbf{x})$ be a function $\in L^2(\mathbb{R}^2)$. Then for all θ we have,*

$$\widehat{H_\delta[f]}(\xi, \theta) = \widehat{f}(\xi \mathbf{u}_\theta)\,.$$

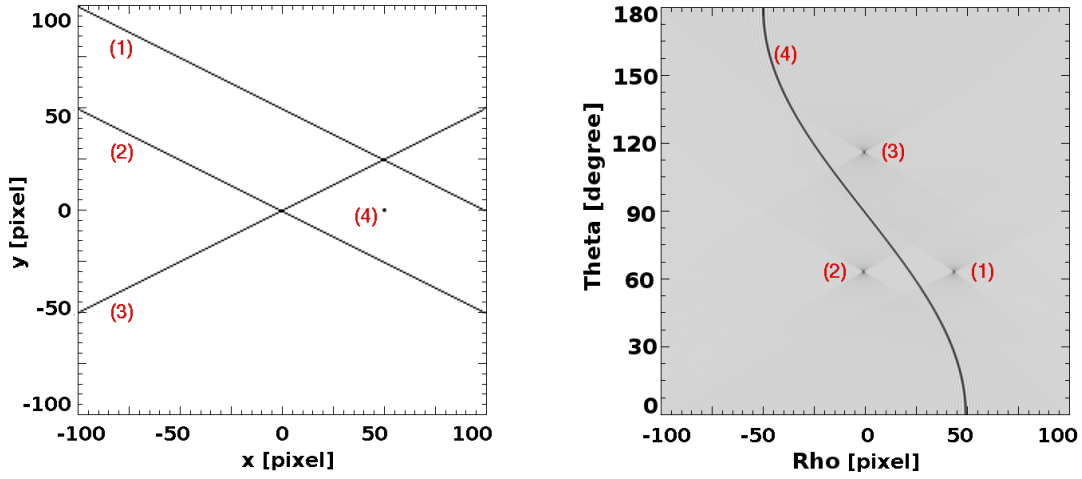

(a) (b)

Figure 3.9: (a) Image (256×256 pixel) composed with three lines and one point. (b) Hough transform of the image. The three lines in the image are associated with a dot, and the dot in the image is associated with a sinusoid.

3.3.2 Hough Transform for Plume Analysis

In this thesis, we use the Hough transform to localize the axes of polar plumes in EUV images. In order to get rid of border effects caused by the solar limb, we map the solar polar region $I(x, y)$ to cylindrical coordinates, see Fig. 3.10 (a): We call the distance from the center of the Sun r and the angle with respect to the projected rotation axis ϕ i.e.:

$$\begin{cases} r = \sqrt{x^2 + y^2} \\ \phi = \arctan\left(\dfrac{x}{y}\right) \end{cases} . \tag{3.26}$$

The image of the polar region $I(x, y)$ from r_1 to r_2 and from $-\phi_0$ to ϕ_0 is then mapped in cylindrical coordinates (s_r, s_ϕ),

$$\breve{I}(s_r, s_\phi) = I(x(s_r, s_\phi), y(s_r, s_\phi)) . \tag{3.27}$$

The new coordinate system (s_r, s_ϕ) is defined by (Fig. 3.10 (b)),

$$\begin{cases} s_r = \dfrac{(r - r_c)}{\Delta r} \\ s_\phi = \dfrac{\phi}{\Delta\phi} \end{cases} , \tag{3.28}$$

where $r_c = \dfrac{r_1 + r_2}{2}$ and Δr, $\Delta\phi$ are normalization factors. In (s_r, s_ϕ)-space, a line is defined by the Hough parameter (ρ, θ),

$$\begin{pmatrix} \cos\theta \\ \sin\theta \end{pmatrix}^\top \cdot \begin{pmatrix} s_\phi \\ s_r \end{pmatrix} = \rho . \tag{3.29}$$

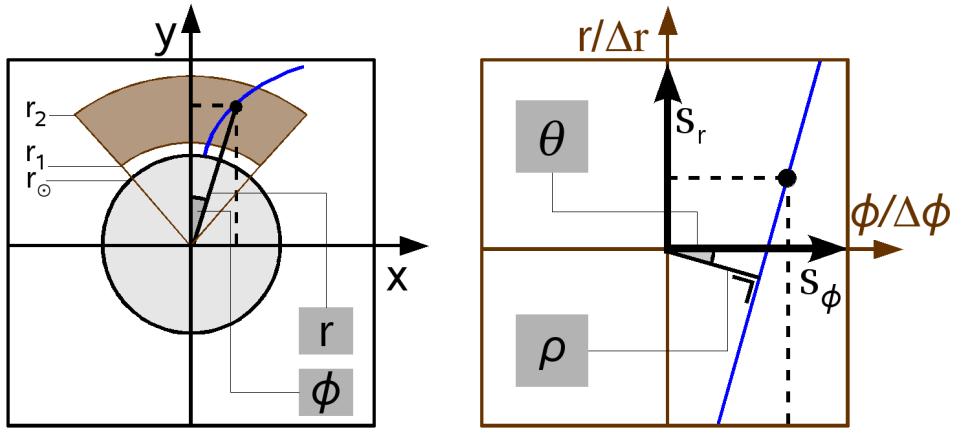

(a) **(b)**

Figure 3.10: (a) Original image in Cartesian coordinates (x, y). (b) Mapped image in cylindrical coordinates (s_r, s_ϕ).

These lines are curves in the original image in Cartesian coordinates (x, y),

$$\boxed{\begin{pmatrix} \cos\theta \\ \sin\theta \end{pmatrix}^{\top} \cdot \begin{pmatrix} \arctan(x/y)\,(\Delta\phi)^{-1} \\ \left(\sqrt{x^2+y^2} - r_c\right)(\Delta r)^{-1} \end{pmatrix} = \rho\,.} \tag{3.30}$$

For a plume peak (ρ_0, θ_0) in Hough-space, its axis in the original image is defined by the curve given in (3.30).

3.3.3 Implementation

As in Section 3.2.2 the image is defined on a grid $[0, N] \times [0, N]$. We compute the Hough transform in Fourier space. With the Fourier Slice Theorem 3.3.2, we have

$$H_\delta[f](\rho, \theta) = \int_{\mathbb{R}} \widehat{f}(\xi \mathbf{u}_\theta)\, e^{i\xi\rho}\, d\xi.$$

which is the 1-D inverse Fourier transform of the Fourier slice image f. It reduces the number of operations from $O((N+1)^4 N_\rho N_\theta)$ to $O((N+1)^2 N_\rho N_\theta \log(N+1))$.

3.3.4 Examples

Here we illustrate the Hough analysis with some relevant examples.

Example As the first example consider a Gaussian of width σ and amplitude A centered at the origin as in example Section 3.2.3,

$$I(\mathbf{x}) \;=\; \frac{A}{2\pi\sigma^2}\, e^{\frac{-|\mathbf{x}-\mathbf{x}_o|^2}{2\sigma^2}}, \quad \hat{I}(\xi \mathbf{u}_\theta) = \frac{A}{\sigma}\, e^{\frac{-\sigma^2}{2}(\xi \mathbf{u}_\theta)^2} e^{i\xi \mathbf{x}_o \cdot \mathbf{u}_\theta}\,. \tag{3.31}$$

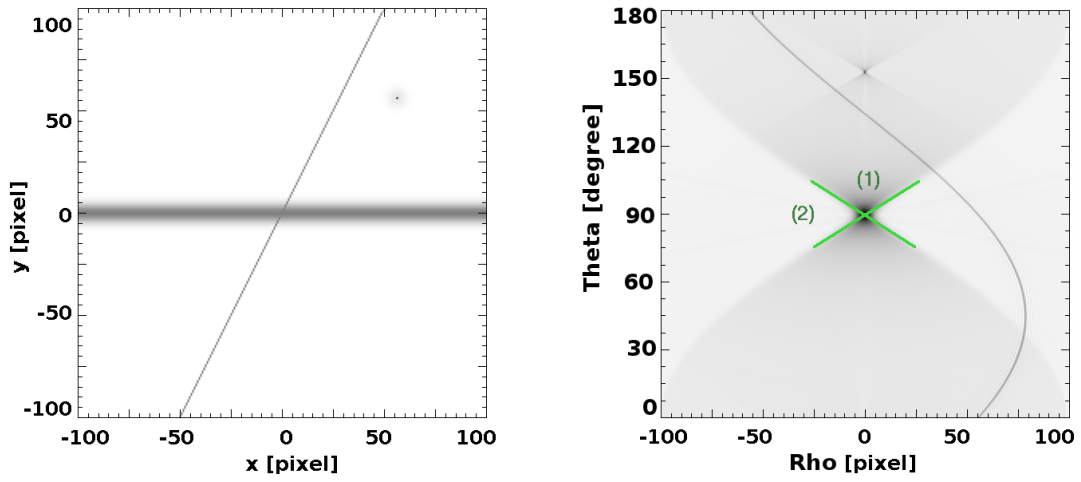

(a) **(b)**

Figure 3.11: (a) Image (256×256 pixel) composed with a line, a Gaussian peak and a Gaussian line. (b) The Hough transform of the image. The green curves are $\rho = \frac{N}{2}\cos\theta$ and $\rho = -\frac{N}{2}\cos\theta$. The region (1) at $\theta = 90°$ refers to (3.39), region (2) refers to (3.35) for $|\rho| < \frac{N}{2}\cos\theta$.

Its Hough coefficients can be computed with the Fourier Slice Theorem 3.3.2,

$$\begin{aligned} H_\delta[f](\rho,\theta) &= \int_{\mathbb{R}^2} \frac{A}{2\pi\sigma^2}\, e^{\frac{-|\mathbf{x}-\mathbf{x}_o|^2}{2\sigma^2}}\, \delta\left(\mathbf{u}_\theta\cdot\mathbf{x}-\rho\right)\, d^2\mathbf{x} \\ &= \frac{A}{\sigma}\int_{\mathbb{R}} e^{\frac{-\sigma^2}{2}(\xi\mathbf{u}_\theta)^2}\, e^{i\xi\rho}\, e^{i\xi\mathbf{x}_o\cdot\mathbf{u}_\theta}\, d\xi \\ &= \frac{A}{\sigma\sqrt{2\pi}}\, e^{\frac{-|\rho-\mathbf{x}_o\cdot\mathbf{u}_\theta|^2}{2\sigma^2}}. \end{aligned} \tag{3.32}$$

The solution corresponds to a sinusoid in the (ρ,ϕ)-space, which is not surprising since for $\sigma\to 0$, we obtain $H_\delta[f](\rho,\theta) = \delta(\rho - \mathbf{x}_o\cdot\mathbf{u}_\theta)$, which is simply the sinusoid $\rho = \mathbf{x}_o\cdot\mathbf{u}_\theta$ as described above.

The image in Fig. 3.11 (a) is composed of a δ-shaped line, a Gaussian peak and two Gaussian lines. Fig. 3.11 (b) shows its Hough coefficients. By extention, we can understand that a Gaussian line in the image-space is transformed into a Gaussian peak in Hough-space.

Example Let an image contain a Gaussian line along the x-axis of width σ and an amplitude A,

$$f(\mathbf{x}) = A\exp\left(\frac{-y^2}{2\sigma^2}\right). \tag{3.33}$$

The Hough transform is calculated as follows,

$$\begin{aligned} H_\delta[f](\rho,\theta) &= \int_{\mathbb{R}^2} A\exp\left(\frac{-y^2}{2\sigma^2}\right)\, \delta\left(\mathbf{u}_\theta\cdot\mathbf{x}-\rho\right)\, d^2\mathbf{x} \\ &= \int_{\mathbb{R}^2} A\exp\left(\frac{-y^2}{2\sigma^2}\right)\, \delta\left(x\cos\theta + y\sin\theta - \rho\right)\, dx\, dy\,. \end{aligned}$$

We have for $\theta = \pi/2$,

$$\begin{aligned} H_\delta[f](\rho, \pi/2) &= \int_{\mathbb{R}^2} A \exp\left(\frac{-y^2}{2\sigma^2}\right) \delta(y - \rho)\ dx\, dy \\ &= A \int_{\mathbb{R}} \exp\left(\frac{-\rho^2}{2\sigma^2}\right) dx\,. \end{aligned} \tag{3.34}$$

For an image f defined on the finite grid $[-N/2, N/2] \times [-N/2, N/2]$, (3.34) becomes,

$$\begin{aligned} H_\delta[f](\rho, \pi/2) &\simeq A \int_{-N/2}^{N/2} \exp\left(\frac{-\rho^2}{2\sigma^2}\right) dx \\ &\simeq A\ N\ \exp\left(\frac{-\rho^2}{2\sigma^2}\right). \end{aligned} \tag{3.35}$$

For $\theta = 0$ we have,

$$\begin{aligned} H_\delta[f](\rho, 0) &= \int_{\mathbb{R}^2} A \exp\left(\frac{-y^2}{2\sigma^2}\right) \delta(x - \rho)\ dx\, dy \\ &= A\sigma\sqrt{2\pi}\,. \end{aligned} \tag{3.36}$$

For an image f defined on the finite grid, (3.36) becomes,

$$H_\delta[f](\rho, 0) \simeq A\sigma\frac{\sqrt{2\pi}}{2}\ \mathrm{erf}\left(\frac{N}{2\sigma\sqrt{2}}\right), \tag{3.37}$$

where erf is the error function[2]. Finally for $\theta \neq \pi/2$ and $\theta \neq 0$, we have

$$\begin{aligned} H_\delta[f](\rho, \theta) &= \frac{1}{|\sin\theta|} \int_{\mathbb{R}^2} A \exp\left(\frac{-y^2}{2\sigma^2}\right) \delta\left(x\frac{\cos\theta}{\sin\theta} + y - \frac{\rho}{\sin\theta}\right) dx\, dy \\ &= \frac{1}{|\sin\theta|} \int_{\mathbb{R}^2} A \exp\left(\frac{-(\frac{\rho - x\cos\theta}{\sin\theta})^2}{2\sigma^2}\right) dx \\ &= \frac{1}{\cos\theta} A\sigma\sqrt{2\pi}\,, \qquad (3.38) \\ &\simeq \frac{1}{\cos\theta} A\sigma\frac{\sqrt{2\pi}}{2}\ \mathrm{erf}\left(\frac{\rho - \frac{N}{2}\cos\theta}{\sigma\sqrt{2}\sin\theta}\right), \qquad (3.39) \end{aligned}$$

where (3.39) is evaluated for an image defined on a finite grid. As can be seen, the transform has an infinite peak at $(\rho, \theta) = (0, \pi/2)$ and finite values in the rest of the parameter space.

If we add noise to image Fig. 3.11, the Hough transform is less robust than the wavelet transform since it does not distinguish the different scales as the wavelet analysis. Fig. 3.12 illustrates this observation.

[2]The error function erf is defined as

$$\mathrm{erf}(x) = \frac{2}{\sqrt{\pi}} \int_0^x \exp\left(-z^2\right) dz\,.$$

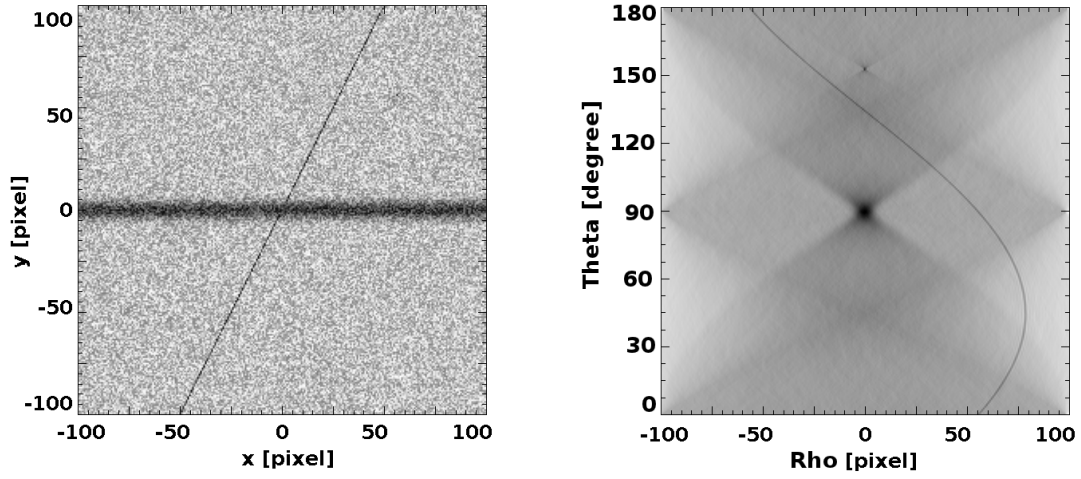

(a) **(b)**

Figure 3.12: (a) Same image (256×256 pixel) as Fig. 3.11 (a) with a Gaussian noise . (b) The Hough transform of (a).

3.4 Hough and Wavelet Transform

As we can see in Fig. 3.11, the basic Hough transform is not well adapted for faint and extended objects with finite width as the example has shown in Fig. 3.12. We propose here to combine the Hough transform, which is well adapted for infinite directional objects, and the wavelet transform, which is more robust to noise and well adapted for detecting faint objects. We call this combination the *Hough-wavelet transform*. A similar extension of the Hough transform was introduced in image processing as the *ridgelet transform* by Candès and Donoho (1999).
In solar physics, it has been used for the first time for the detection of solar polar plume in EUV images (de Patoul et al., 2011).

3.4.1 Hough-wavelet Transform

This new transformation consists of a Hough transform followed by a 1-D wavelet transform with L^1 normalization:

$$\begin{aligned}\frac{1}{a}\int_{\mathbb{R}} \psi\left(\frac{t-\rho}{a}\right) H_\delta[f](\rho,\theta)\, dt &= \frac{1}{a}\int_{\mathbb{R}}\int_{\mathbb{R}^2} \psi\left(\frac{t-\rho}{a}\right) f(\mathbf{x})\, \delta\left(\mathbf{u}_\theta \cdot \mathbf{x} - \rho\right)\, d^2\mathbf{x}\, dt \\ &= \frac{1}{a}\int_{\mathbb{R}^2} f(\mathbf{x})\, \psi\left(\frac{\mathbf{u}_\theta \cdot \mathbf{x} - \rho}{a}\right) d^2\mathbf{x}\,,\end{aligned}$$

where $\mathbf{u}_\theta = (\cos\theta\ \sin\theta)$ is a unit vector, $\theta \in [0, \pi[$ is the angle formed by the vector $\mathbf{u}_\theta$ and the x-axis, $a \in \mathbb{R}_0^+$ is the scale, and $\rho \in \mathbb{R}$ is the distance between the center of ψ and the origin. By convention, ρ is negative for $\theta \in [\pi/2, \pi[$. Fig.3.13 (a) describes (ρ, a, θ)-parameters in image coordinates. Regarding the wavelet transform, we can define a family of wavelets with the three

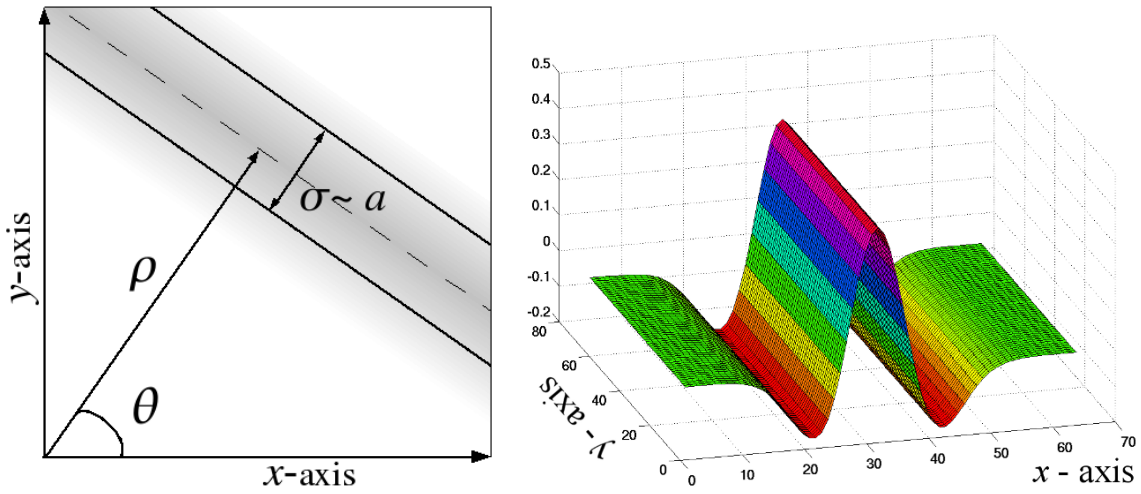

(a) (b)

Figure 3.13: (a) Geometric illustration of the Hough-wavelet parameters $\theta \in]0, \pi]$, $\rho \in [-\rho_{\max}, \rho_{\max}] \subset \mathbb{R}$ and $a \in \mathbb{R}_0^+$. The parameter a is proportional to the cross section width σ. (b) An example of a wavelet generated from the Mexican Hat mother wavelet (3.44) with the parameters $a = 8, \rho = 35$ and $\theta = 0$.

elementary transformations, i.e., translation by $\rho \in \mathbb{R}$, rotation by $\theta \in [\pi/2, \pi[$ and dilatation by $a \in \mathbb{R}_0^+$,

$$\psi_{\rho,a,\theta}(\mathbf{x}) \quad = \quad \sqrt{\frac{1}{a}}\, \psi\left(\frac{\mathbf{u}_\theta \cdot \mathbf{x} - \rho}{a}\right). \tag{3.40}$$

In Fourier space, the family of wavelets becomes,

$$\widehat{\psi}_{\rho,a,\theta}(\mathbf{k}) \quad = \quad \sqrt{a}\, \widehat{\psi}\,(a\, \mathbf{k} \cdot \mathbf{u}_\theta)\; e^{-i\mathbf{k}\rho}\,. \tag{3.41}$$

Definition 3.4.1. *For a given image f and a known wavelet ψ, the* Hough-wavelet transform *is the inner product (3.2) of f and $\psi_{\rho,a,\theta}$ as a function of (ρ, a, θ):*

$$HW_\psi[f](\rho, a, \theta) \quad = \quad \left\langle \psi_{\rho,a,\theta} | f \right\rangle = \sqrt{\frac{1}{a^{3-n}}} \int_{\mathbb{R}^2} \psi\left(\frac{\mathbf{u}_\theta \cdot \mathbf{x} - \rho}{a}\right) f(\mathbf{x})\, d^2\mathbf{x} \tag{3.42}$$

$$= \quad \left\langle \widehat{\psi}_{\rho,a,\theta} | \widehat{f} \right\rangle = \sqrt{\frac{1}{a^{1-n}}} \int_{\mathbb{R}^2} \widehat{\psi}\,(a\, \mathbf{k} \cdot \mathbf{u}_\theta)\; e^{-i\mathbf{k}\rho}\; \widehat{f}(\mathbf{k})\, d^2\mathbf{k} \tag{3.43}$$

where $\psi_{\rho,a,\theta}$ is the family of wavelets generated from ψ and $n = 1$ or 2 in normalization L^1 and L^2 respectively.

The family of wavelets generated from the Mexican Hat mother wavelet (3.44) are according to (3.40) for $n = 1$,

$$\psi^{MH}_{\rho,a,\theta}(\mathbf{x}) \quad = \quad -\frac{1}{a}\left(2 - \frac{|\mathbf{u}_\theta \cdot \mathbf{x} - \rho|^2}{2a^2}\right) \exp\left(-\frac{|\mathbf{u}_\theta \cdot \mathbf{x} - \rho|^2}{2a^2}\right). \tag{3.44}$$

Fig.3.13 (b) shows an example of this wavelet translated by $\rho = 35$, dilated by a factor $a = 8$ and not rotated ($\theta = 0$).

This method offers both advantages from the Hough transform and the wavelet transform, therefore this transform yields a multi-scale analysis robust to noise, and has the property of being invertible, and allows a perfect backward transform into the image space.

3.4.2 Hough-wavelet Transform for Plume Analysis

We use the Hough-wavelet transform to detect polar plumes in EIT and EUVI images. In practice, we map the solar polar region to cylindrical coordinates (3.28), i.e.,

$$\breve{I}(s_r, s_\phi) = I(x(s_r, s_\phi), y(s_r, s_\phi)) \; .$$

The image $\breve{I}(s_r, s_\phi)$ is then analyzed by the Mexican Hat wavelet (3.44) with the Hough-wavelet transform (3.43),

$$HW_{\psi^{MH}}[\breve{I}](\rho, a, \theta) = \int_{-s_{r0}}^{s_{r0}} \int_{-s_{\phi 0}}^{s_{\phi 0}} \breve{I}(s_r, s_\phi) \; \psi^{MH}_{\rho,a,\theta}(s_r, s_\phi) \; ds_r \; ds_\phi \; . \tag{3.45}$$

The Hough-wavelet transform (3.45) is a function of three variables (ρ, a, θ). In order to obtain a manageable tool, some of the variables need to be eliminated. Either we keep the value of some of the variables fixed or we integrate out some of the variables. Since the Hough-wavelet coefficients of an image has the property to maximize when the parameter ρ, a, and θ match in position, orientation and scale with an object in the image, we decide to keep the value of the variable a fixed in the following way: For each position (ρ, θ), we determine the optimum scale $a_{\mathrm{M}}(\rho, \theta)$ where the Hough-wavelet coefficients are maximum,

$$a_{\mathrm{M}}(\rho, \theta) = \arg\max_{a} \; [\; HW_{\psi^{MH}}[\breve{I}_t](\rho, a, \theta) \;] \; . \tag{3.46}$$

Then we condense the Hough-wavelet transform of the plume signal into the Hough-space (ρ, θ):

$$\boxed{\mathrm{H}(\rho, \theta) \equiv HW_{\psi^{MH}}[\breve{I}](\rho, a_{\mathrm{M}}, \theta) \; .} \tag{3.47}$$

Finally, we define the Hough-space intensity by the following weighted integral,

$$\boxed{\mathrm{I}(\rho) \equiv \int_0^{2\pi} \mathrm{H}(\rho, \theta) \; \mathrm{W}(\rho, \theta) \; d\theta \; .} \tag{3.48}$$

$\mathrm{W}(\rho, \theta)$ is the weight function that gives more weight in the interesting part. This function is defined later. These formulations (3.47)–(3.48) are the starting point for our futher analysis.

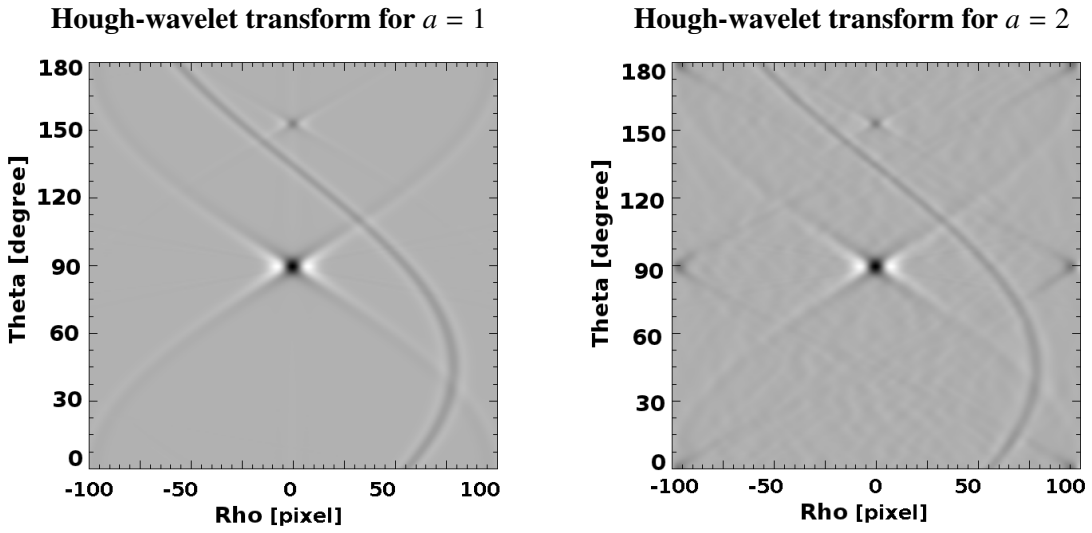

Figure 3.14: (a) Hough-wavelet transform of Fig. 3.12 (a). (b) Hough-wavelet transform Fig. 3.11 (a).

3.4.3 Implementation

As in the two previous Sections 3.2.2–3.3.3, the image is defined on a grid $[0, N] \times [0, N]$ and we compute the Hough-wavelet transform of the image f from Fourier space:

$$HW_\psi[f](\rho, a, \theta) = a \int_{\mathbb{R}^2} \widehat{\psi}(a\, \mathbf{k} \cdot \mathbf{u}_\theta)\ e^{-i\mathbf{k}\rho}\ \widehat{f}(\mathbf{k})\, d^2\mathbf{k}\ .$$

For the final plume analysis, edge effects and variable support of ψ inside the image for large values of a, ρ are taken into account by restricting the parameters ρ, a and θ.

3.4.4 Examples

We take the example given in Section 3.4.4 with the Fig. 3.12 (a). Since the Hough-wavelet transform is the Hough transform followed by a 1-D wavelet transform, we take simply the image in Fig. 3.12 (b) and compute the 1-D wavelet transform. The result is shown in Fig. 3.14. We see clearly that the method produces a better result for noisy data.

Example The Hough-wavelet transform can be analytically calculated for a Gaussian line with a certain width, σ, and an amplitude, A, (de Patoul et al., 2011). For a Gaussian line along the y-axis,

$$f(\mathbf{x}) = A \exp\left(\frac{-y^2}{2\sigma^2}\right)\ , \tag{3.49}$$

we compute the Hough-wavelet coefficients with θ orientated in the direction of the Gaussian line, $\theta_{\text{M}} = \pi/2$,

$$HW_{\psi^{MH}}[f](\rho, a, \theta_{\text{M}}) = \int_{\mathbb{R}^2} f(\mathbf{x})\, \psi^{MH}_{\rho,a,\theta_{\text{M}}}(\mathbf{x})\, d\mathbf{x} \tag{3.50}$$

$$= -\frac{Aa\sigma\sqrt{2\pi}}{(a^2+\sigma^2)^{\frac{3}{2}}}\left(\frac{\rho^2}{(a^2+\sigma^2)} - 1\right)\exp\left(\frac{-\rho^2}{2(a^2+\sigma^2)}\right). \tag{3.51}$$

At $\rho = \rho_{\text{M}} = 0$, (3.51) has its maximum:

$$HW_{\psi^{MH}}[f](\rho_{\text{M}}, a, \theta_{\text{M}}) = \frac{a}{(a^2+\sigma^2)^{\frac{3}{2}}}\, A\sigma\sqrt{2\pi}\ . \tag{3.52}$$

In terms of scale a, this function has a maximum for $a = a_{\text{M}}$:

$$\boxed{a_{\text{M}} = \sqrt{2}\sigma\ .} \tag{3.53}$$

At this optimum scale $a = a_{\text{M}}$, the Hough-wavelet coefficients have a value of

$$HW_{\psi^{MH}}[f](\rho_{\text{M}}, a_{\text{M}}, \theta_{\text{M}}) = \frac{2\sqrt{\pi}}{3\sqrt{3}}\frac{A}{\sigma}\ . \tag{3.54}$$

The Hough-wavelet coefficients are therefore proportional to the amplitude A, of the Gaussian and inversely proportional to the Gaussian width σ.

Fig. 3.15 (a) represents two Gaussian lines located at $\mathbf{x}_1 = -85.33$ pixels and $\mathbf{x}_2 = 85.33$ pixels. They have a width equal to $\sigma_1 = 4$ pixels and $\sigma_2 = 10$ pixels respectively. The Hough-wavelet transform $HW_{\psi^{MH}}[f](\rho, a, \theta)$ is calculated for scales $a = 1, \ldots 32$ pixels, $\theta = 1°, \ldots 179°$ and $\rho = -256 \cdots + 256$ pixels. In Fig. 3.15 (b)–(d) we show some examples of $HW_{\psi^{MH}}[f](\rho, a, \theta)$ for $a = 3, 7, 16$ and 32 pixels where the colorbar goes from black for the minimum value to blue, yellow, red and white for the maximum value. The Hough-wavelet coefficients of this image maximize when the parameter ρ, a, and θ match in position, orientation and scale with each Gaussian signal in the image.

The coefficients are maximum when the parameter $\theta = \theta_{\text{M}} = 90°$. A cut of the Hough-wavelet transform at $HW_{\psi^{MH}}[f](\rho, a, \theta_{\text{M}})$ is shown in Fig. 3.16 (a). In this figure we see clearly that we have two maxima for the scales $a_1 = 5.79$ and $a_2 = 14.40$, which is, according to (3.53), $\sigma_1 = 4.09$ and $\sigma_2 = 10.18$, respectively. It corresponds to a 0.02% error.
Fig. 3.16 (b) shows the Hough-wavelet transform $HW_{\psi^{MH}}[f](\rho, a_{\text{M}}, \theta)$ with a_{M} evaluated for each (ρ, θ) value. We found a local maximum at $(\rho_1, \theta_1) = (-84.61, 0.50)$ and $(\rho_2, \theta_2) = (85.76, 0.50)$, which is in agreement with our input image.
Fig. 3.16 (c) shows the Hough-wavelet transform $HW_{\psi^{MH}}[f](\rho_{\text{M}}, a, \theta)$ with ρ_{M} evaluated for each (a, θ) value and Fig. 3.16 (d) a cut at $\theta = 90°$.

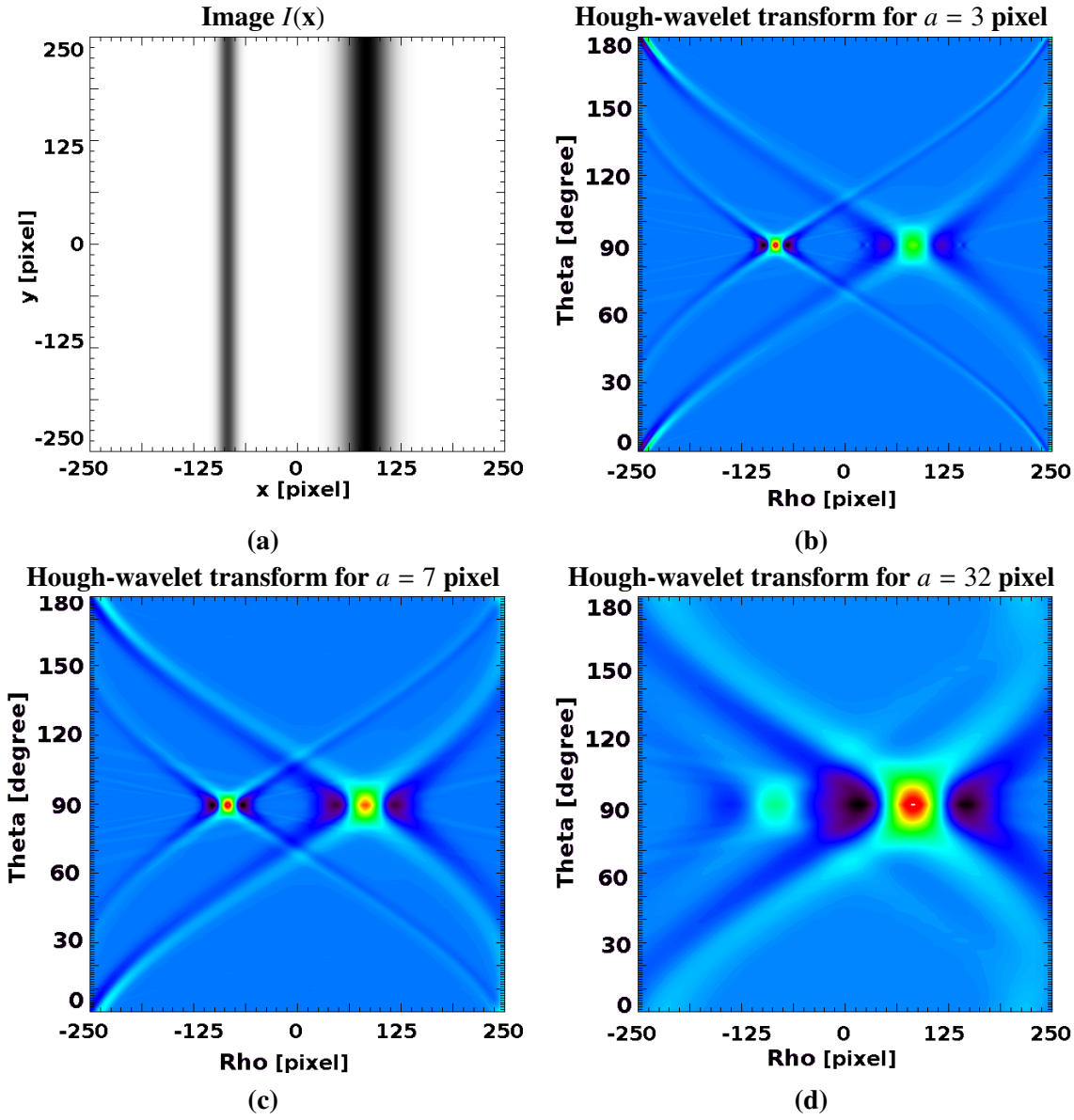

Figure 3.15: (a) Image (512×512 pixel) with two Gaussian lines located at $x_1 = -85.33$ pixels and $x_2 = 85.33$ pixels. They have a width equal to $\sigma_1 = 4$ pixels and $\sigma_2 = 10$ prixels respectively. (b) – (d) The Hough-wavelet transform $HW_{\psi^{MH}}[f](\rho, a, \theta)$ for $a = 3, 7$, and 32 pixels where the color code ranges from black for the minimum values to white for maximum values.

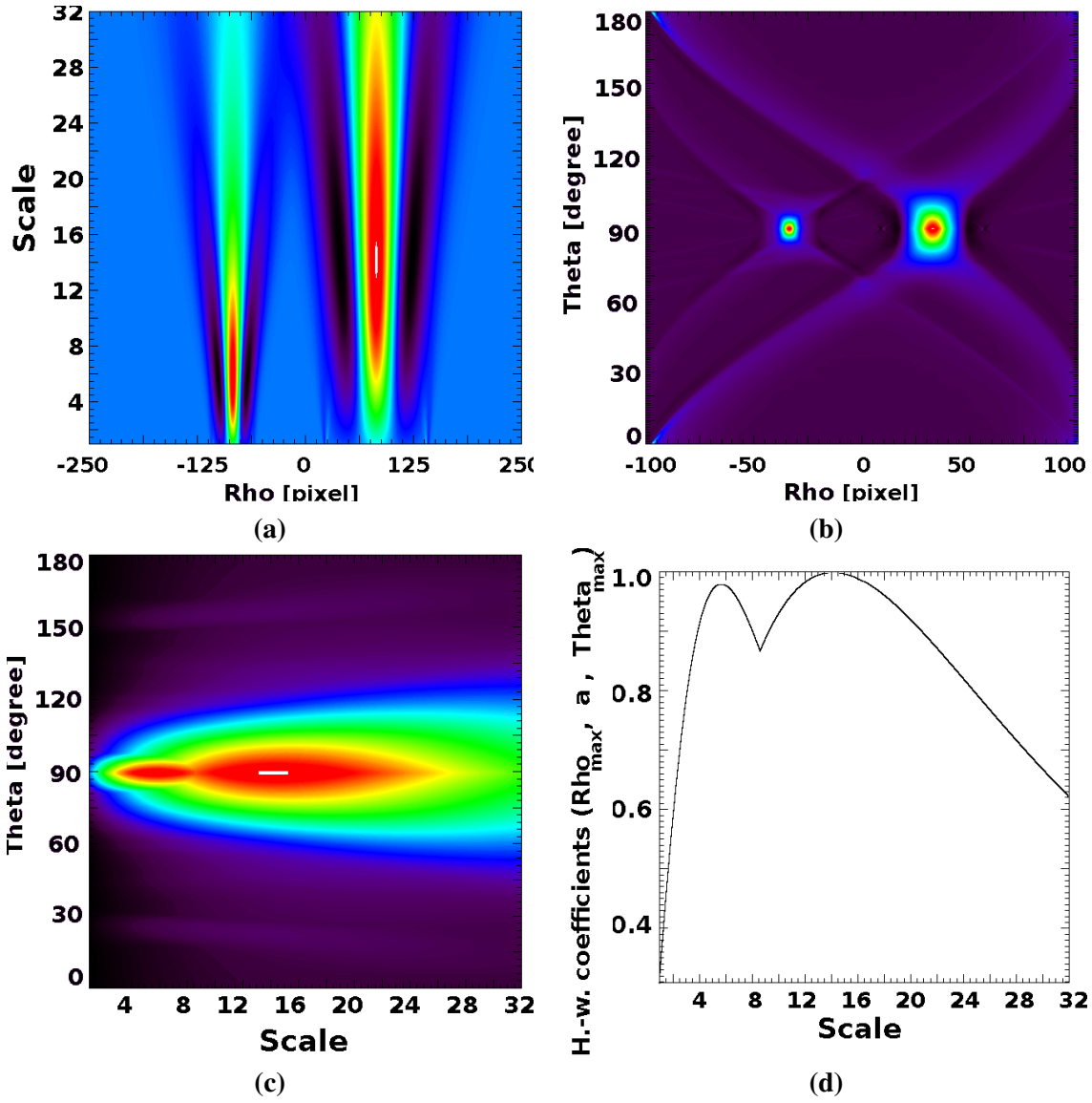

Figure 3.16: (a) A cut of the Hough-wavelet transform at $HW_{\psi^{MH}}[f](\rho, a, \theta)$ at $\theta = 90^o$ calculate the image Fig. 3.15 (a) where we see two local maxima at $(\rho_1, a_1) = (-84.61, 5.79)$ and $(\rho_1, a_1) = (85.76, 14.40)$. (b) Local maxima over the scale of the Hough-wavelet transform evaluated for each (ρ, θ) value: $HW_{\psi^{MH}}[f](\rho, a_{\rm M}((\rho, \theta)), \theta)$. (c) Local maxima over ρ of the Hough-wavelet transform evaluated for each (a, θ) value: Hough-wavelet transform $HW_{\psi^{MH}}[f](\rho_{\rm M}(a, \theta), a, \theta)$. and if (d), a cut at $\theta = 90°$.

This example can serve as a model of polar plumes in EUV images. For STEREO/EUVI images, 1 pixel is about 1.11 Mm in the plane of the sky. For SOHO/EIT we have 1 pixel is about 2.22 Mm in the plane of the sky. In the mapped image $\breve{I}(s_r, s_\phi)$, 1 pixel corresponds to $(R_\odot \Delta\phi) \times (\Delta r)$ in $(R_\odot/\text{pixel})^2$. For a plume with a Gaussian cross section of width σ, 95% of its Gaussian cross section intensity is $4 \times \sigma$. Therefore, the broadness of a Gaussian width of a radial plume is

$$a \times 4/\sqrt{2} \times \Delta\phi \text{ in } R_\odot \, .$$

Since plumes are not all radial, we see later that this formulation needs to be slightly changed in order to take into account the inclination of the plumes.

3.5 Summary and Conclusion

The purpose of this chapter is to investigate advanced image analysis techniques for solar image processing and in particular for detecting polar plumes in EUV images.

The first method we have investigated is the well established wavelet transform. We have proposed to use the Mexican Hat wavelet, which has a simple analytic expression and is robust due to its two vanishing moments. We have tested our approch with series of annalytic examples and we have compared them with the numerical solutions. From these examples we have demonstrated that how the method is sensitive and scale selective. Through the wavelet analysis we have also studied the instrumental noise in the EUVI data: cosmic ray hits and compression effect in EUV images in the off-disk part. At scales a less than 2 pixel, the wavelets detected a noise similar to a Gaussian noise and at larger scale (a = 2.5 pixel to 10.40 pixel) cosmic ray hits and compression effect were detected. We learned from these examples that for a Mexican Hat wavelet analysis on solar images, we need to clean the image from cosmic ray hits and from the compression effect and we need to choose the scale range a larger than 2 pixel.

The second method we have introduced is the Hough transform. This technique is known for its capacity to extract lines in an image. We have considered the example of a strip with Gaussian cross section and compared the analytic and numerical solutions. In case of noise, the example showed that the method is not well adapted for detecting elongated objects with low signal to noise ratio, such as plumes seen in EUV images. It is not a multi-scale method and therefore, it does not give information about the width of the plumes. However, we have shown that it is a convenient method to define the axis orientation and location.

Finally we have established a third method, the Hough-wavelet transform, which combines the advantages from both previous methods. It has the capacity to extract infinite directional objects with a finite width. It is also well adapted for detecting faint objects in images with low signal to noise ratio. This method is used to automatically extract plumes in EUV images.

Chapter 4
3D Reconstruction Tools

SOHO/EIT and STEREO/EUVI observations of the solar corona are the projection of 3D plasma structures onto an image plane. A single projection contains only partial information about the 3D object. To obtain multiple projections from different perspectives, we can take account of the solar rotation. If we consider the observations from more than one instrument, we obtain more than one nearly simultaneous view directions for looking at the Sun.

In this chapter we discuss two imaging techniques to retrieve the 3D density and geometry of an object, which is lost by the projection; (i) *stereoscopy* retrieves the depth of points in 3D space from two different projections, provided we can properly identify the points in the images; (ii) *tomography* reconstructs a volumetric object from multiple projections over half a rotation. We also discuss the difficulties and limitations of each technique in the case of coronal polar plume study. We show that using both techniques on the same data set considerably improves the results.

We start this chapter with a description of a sinogram built with Hough wavelet coefficients (Section 4.1). In Section 4.2, we describe tomographic methods. Then we present stereoscopic methods, which could be considered as a special case of tomography with only two view directions (Section 4.3). Finally, through a 3D synthetic plume model, we show that both, tomographic and stereoscopic techniques are complementary. We also show that the Hough-wavelet transform is a convenient tool, which can be used as input for the 3D reconstructions.

4.1 Sinogram

Solar coronagraph or EUV images provide the line-of-sight integration of the 3D plasma intensity, from different directions as the Sun rotates. From this 3D plasma intensity one can derive the density of the plumes. Fig. 4.1 (a) sketches the 3D plume with cross sectional planes stacked normal to the solar rotation axis. Fig. 4.1 (b) shows the image plane where each row provides the line-of-sight integration of the intensity in each of these cross sectional planes.

For a Hough-space intensity approach, the plume signals in each of the planes stacked normal to the solar rotation axis are condensed into the Hough-wavelet density $D(\mathbf{x})$ for $\mathbf{x} \in \mathbb{R}^2$, Fig. 4.1 (c).

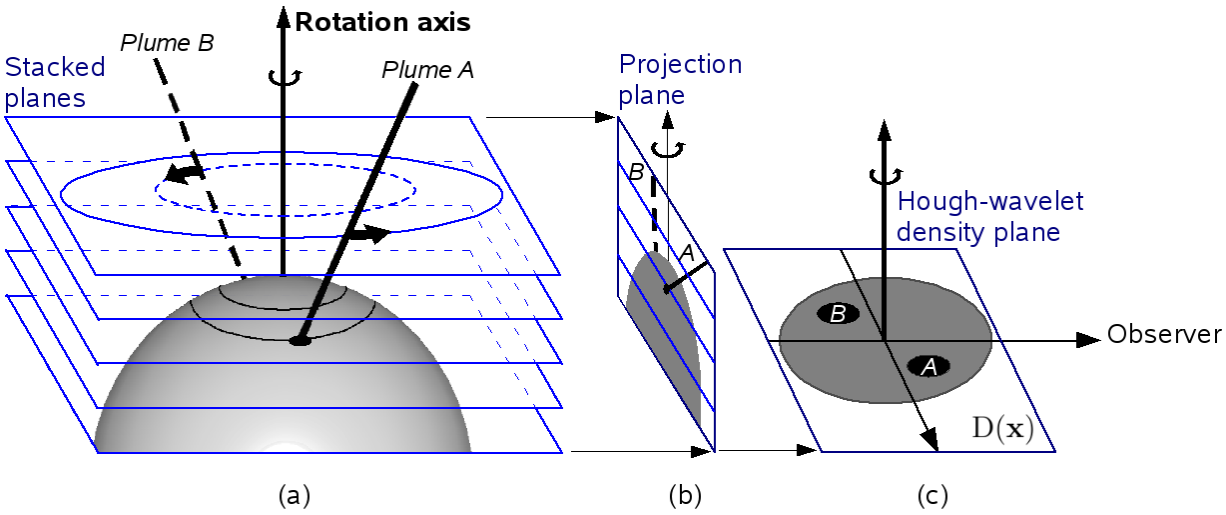

Figure 4.1: (a) Sketch of 3D plume density (two plumes) with cross section planes (in blue) stacked normal to the rotation axis. (b) The image plane, which provides the line-of-sight integration of this 3D density. (c) Hough-wavelet density, which is the condensation of the all stacked cross sectional planes.

The starting point for our analysis is the Hough-space intensity (3.48) computed for an image at time t,

$$\mathrm{I}(\rho; t) = \int_{\theta_1}^{\theta_2} \mathrm{H}(\rho, \theta; t)\, \mathrm{W}(\rho, \theta)\, d\theta\,, \tag{4.1}$$

for $\theta_1, \theta_2 \in [-\pi, \pi]$. In the following, we replace the time dependence by an angle ϑ of the view direction onto the Sun. The Hough-wavelet density $\mathrm{D}(\mathbf{x})$ integrate in the line-of-sight (LOS) direction $\mathbf{e}_{\mathrm{LOS}}(\vartheta) = (\sin\vartheta,\ \cos\vartheta)$ is

$$\mathrm{I}(\varrho, \mathbf{e}_{\mathrm{LOS}}(\vartheta)) = \int_{\mathrm{LOS}} \mathrm{D}(\mathbf{x})\, dl \tag{4.2}$$

where $\mathrm{I}(\varrho, \mathbf{e}_{\mathrm{LOS}}(\vartheta))$ is the Hough-space intensity seen by an observer offset by a distance $\varrho \in \mathbb{R}$ (see, Fig. 4.2) and l is the line-of-sight along which we integrate. The angle ϑ represents the rotation angle of the Sun relative to the observer's longitude. This angle ϑ will be specified later to take account of the Sun's differential rotation. The 2D line-of-sight vector direction $\mathbf{e}_{\mathrm{LOS}}(\vartheta)$ corresponds to the 3D ray given by (1.8) but averaged over the Hough-wavelet kernels. We can rewrite (4.2) as,

$$\mathrm{I}(\varrho, \vartheta) = \int_{\mathrm{LOS}} \mathrm{D}(\mathbf{x})\, \delta\left(\mathbf{x} - (\varrho\, \mathbf{e}^{\perp}_{\mathrm{LOS}}(\vartheta) + l\, \mathbf{e}_{\mathrm{LOS}}(\vartheta)\right)\, dl, \tag{4.3}$$

where $\mathbf{e}^{\perp}_{\mathrm{LOS}}$ is normal to $\mathbf{e}_{\mathrm{LOS}}(\vartheta)$ and for points $\mathbf{x}$ on the line-of-sight,

$$\mathbf{e}^{\perp}_{\mathrm{LOS}}(\vartheta) \cdot \mathbf{x}\ = x\cos\vartheta + y\sin\vartheta = \varrho \tag{4.4}$$

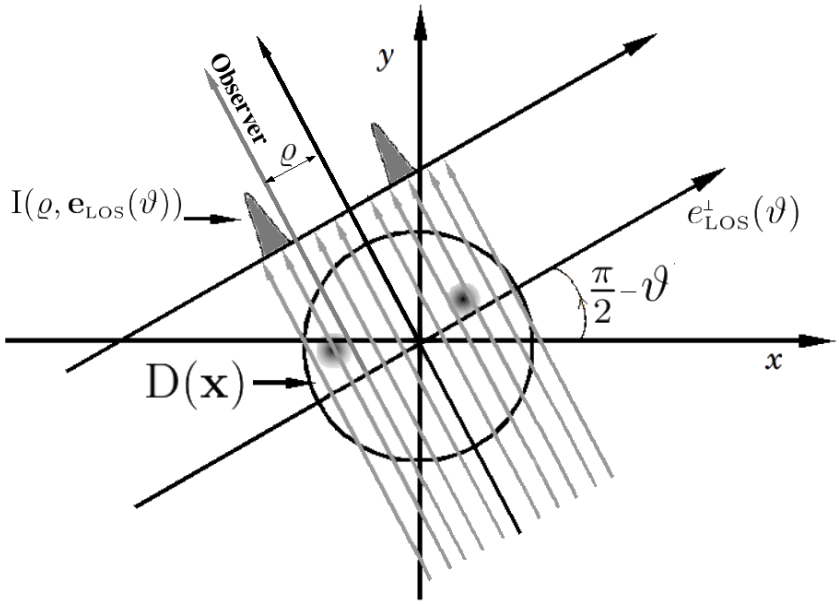

Figure 4.2: The line-of-sight projection of the Hough-wavelet density D(x) containing three Gaussian peaks. An observer, in the direction $\mathbf{e}_{\mathrm{LOS}}(\vartheta) = (\sin\vartheta,\ \cos\vartheta)$ and offset by the distance ϱ, sees the projected Hough-space intensity $\mathrm{I}(\varrho, \vartheta)$.

The function $\mathrm{I}(\varrho, \vartheta)$ is represented by a (ϱ, ϑ)-graph referred to as a *sinogram* because sinogram of a a point source in D(**x**) has a characteristic sinusoid shape. Fig. 4.3 (a) gives an example of a series of projections at $\vartheta = 70°$, 80° and 90° for a density D(**x**) containing three Gaussian peaks. The resulting sinogram for $\vartheta = 0°$ to 180° is shown in Fig. 4.3 (b).

4.2 Tomography

The inversion process to estimate the coronal density from solar cornagraph or EUV images is known as *solar rotational tomography*. The basic principle of tomography is the following: While the Sun rotates, from each row of the image, we reconstruct the 2D density on each stacked plane normal to the solar rotation axis, see Fig. 4.1 (b) (a). Since the original work by Altschuler and Perry (1972), the solar rotational tomography methods for estimating electron density of the corona have been refined considerably. A comprehensive review of its development is found in Frazin and Kamalabadi (2005).

The major problem using solar rotational tomography is that it is based on two implicit assumptions, which do not hold well with coronal observations:

- the assumption of a solid rotation of the global corona,
- the assumption of stationarity of coronal structures as the Sun rotates.

These shortcomings generally enhance the intrinsic ill-posedness of the tomography problem. One approach is to stabilize the reconstruction by smoothing the solution with a regularization

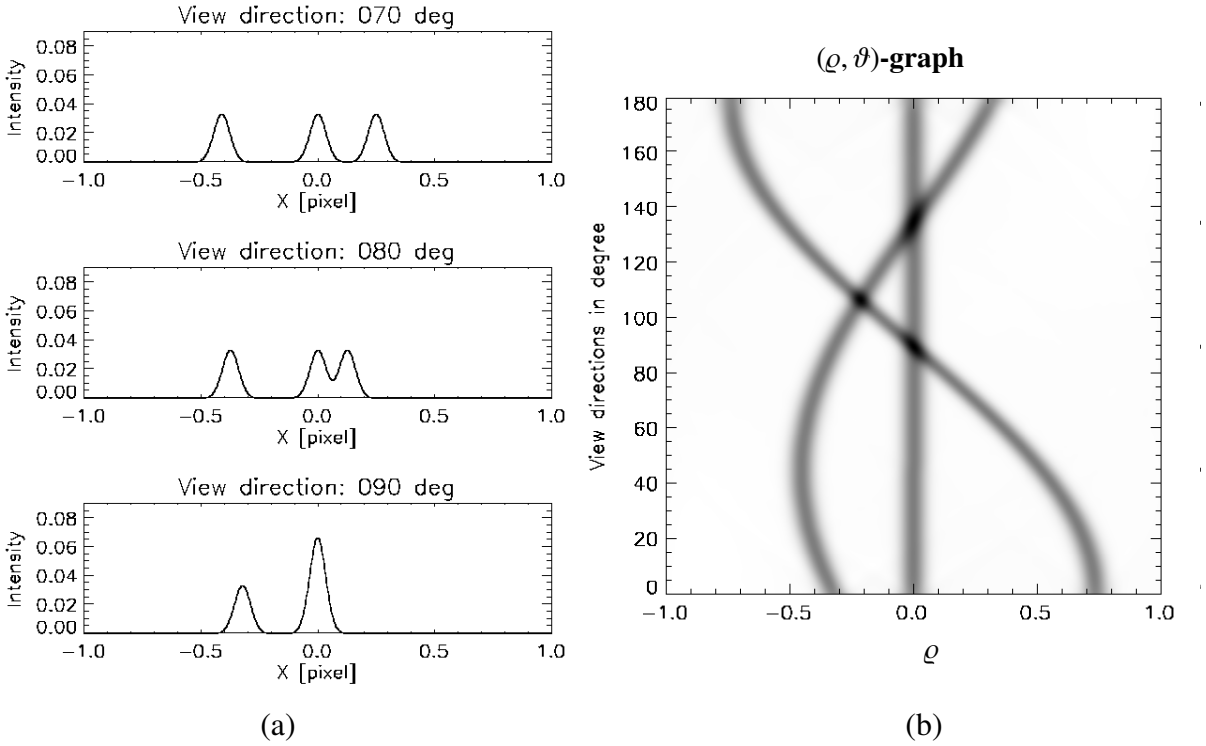

Figure 4.3: (a) Set of projections of a density D(x) taken at different angle ϑ. (b) Sinogram of D(x) where the grayscale denote the intensity.

procedure. Another approach is to constrain the solutions, for example by adding magnetic field extrapolation information (Wiegelmann and Inhester, 2003), or by adding a priori information about the location and shape of the object (e.g., Thernisien et al. (2006)).

Since plume signals are condensed into the Hough-wavelet space D(**x**) our problem is reduced to a 2D tomography case. For the tomography algorithm, we use the filtered backprojection method. In addition to the classical reconstruction procedure, we will include the known solar differential rotation in the reconstruction formula. We will demonstrate by test calculations, that including differential rotation yields a better spatial resolution than conventional reconstructions.

4.2.1 Filtered Backprojection in 2D

In order to find the Hough-wavelet density D(**x**), we need to invert the transform (4.3). The method used here is the *filtered backprojection* described in Natterer (2001). The basic backprojection reconstruction is formed by projecting each view backwards from the observer in the direction it was originally acquired, see Fig. 4.4 (a).

The preliminary backprojected image is then obtained as the superposition of all the backpro-

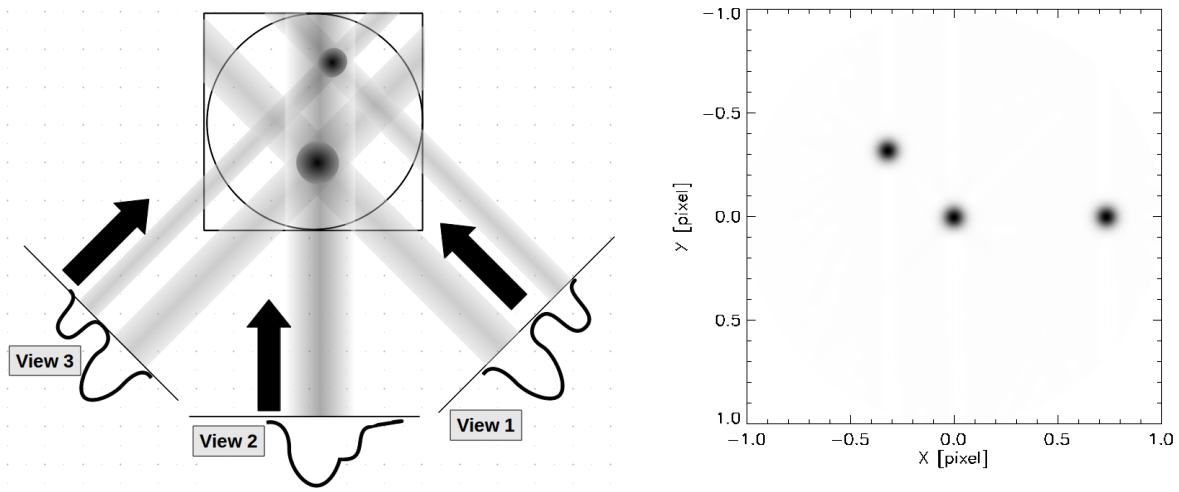

(a) (b)

Figure 4.4: (a) Basic backprojection reconstruction formed by projecting each view backward through the image in the direction it was originally acquired. (b) Backprojection reconstruction for the series of projection in Fig. 4.3 with 180 views.

jected views,

$$\tilde{\mathrm{D}}(\mathbf{x}) = \int_0^{\pi} \int_{\mathbb{R}} \delta\left(\mathbf{e}_{\mathrm{LOS}}^{\perp}(\vartheta) \cdot \mathbf{x} - \varrho\right) \mathrm{I}(\varrho, \vartheta)\, d\varrho\, d\vartheta\,. \tag{4.5}$$

where $\tilde{\mathrm{D}}(\mathbf{x})$ is an approximation of the density $\mathrm{D}(\mathbf{x})$. Fig. 4.4 (b) shows an example of backprojection reconstruction for the series of projections in Fig. 4.3. The classical backprojection procedure reconstructs a point as a diffuse circular region even with a large number of view directions. An example of the backprojection for a disk is shown in Fig. 4.5.

To improve the spatial resolution of the backprojection, each of the 1-D views is convolved with a filter before the backprojection operation. We use the filter function suggested by Natterer (2001):

$$\mathrm{F}(\varrho) = \frac{N^2}{4\pi^2} \begin{cases} \dfrac{(1-2\epsilon)\cos\varrho - 1}{\varrho^2} + \left(1 - \epsilon + \dfrac{2\epsilon}{\varrho^2}\right)\dfrac{\sin\varrho}{\varrho} & \text{for} \quad \varrho \neq 0 \\ \dfrac{1}{6} & \text{for} \quad \varrho = 0 \end{cases}, \tag{4.6}$$

where $\epsilon \in [0, 1]$. The function $\mathrm{F}(\varrho)$ is plotted for $\epsilon = 0$ and $\epsilon = 1$ in Fig. 4.6 (a) and (b) respectively. The backprojection (4.5) is then rewritten in its filtered version,

$$\mathrm{D}(\mathbf{x}) = \int_{\mathbb{R}} \int_0^{\pi} \delta\left(\mathbf{e}_{\mathrm{LOS}}(\vartheta) \cdot \mathbf{x} - \varrho\right) \int_{\mathbb{R}} F(\varrho' - \varrho) I(\varrho', \vartheta)\, d\varrho'\, d\varrho\, d\vartheta\,. \tag{4.7}$$

Fig. 4.7 (a) and (b) show the result for a disk (shown in Fig. 4.5 (a)) of the filtered backprojection with $\epsilon = 0$ and $\epsilon = 1$, respectively. In this basic example, we see that $\epsilon = 1$ gives a slightly better

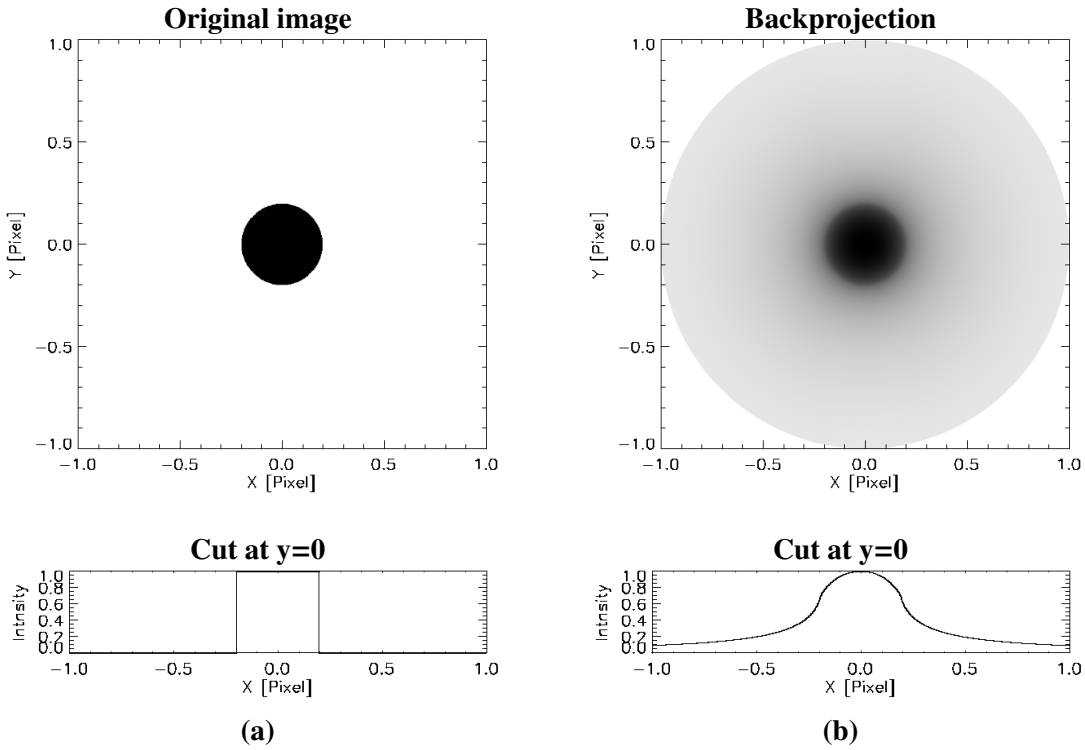

Figure 4.5: Original image in (a) and basic backprojection reconstruction in (b), calculated for 180 views. We can see that the result is very diffuse.

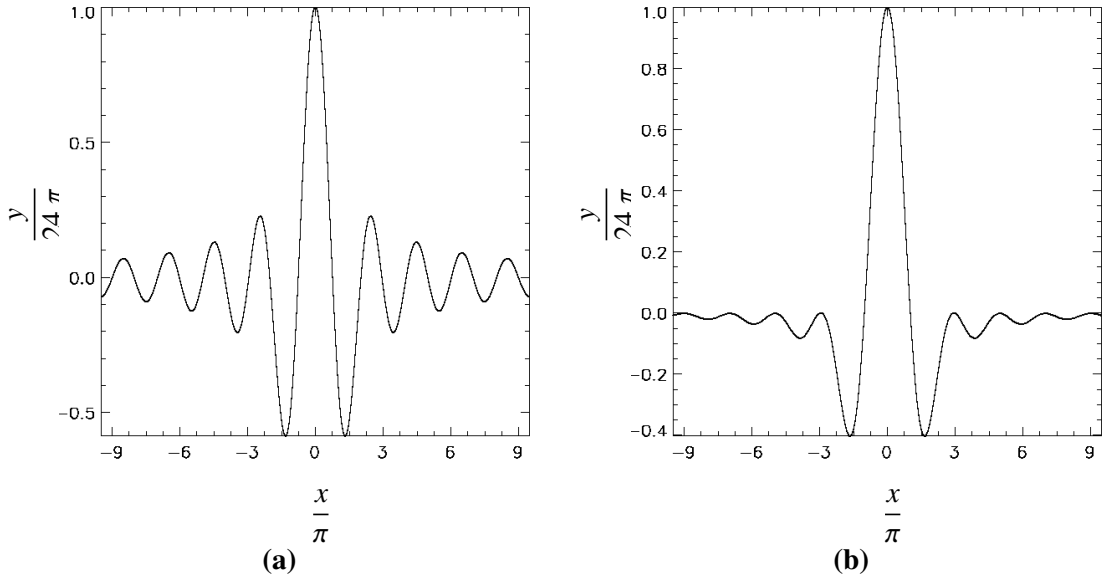

Figure 4.6: Filter function used to improve the spatial resolution of simple backprojection: for $\epsilon = 0$ in (a) and for $\epsilon = 1$ in (b)

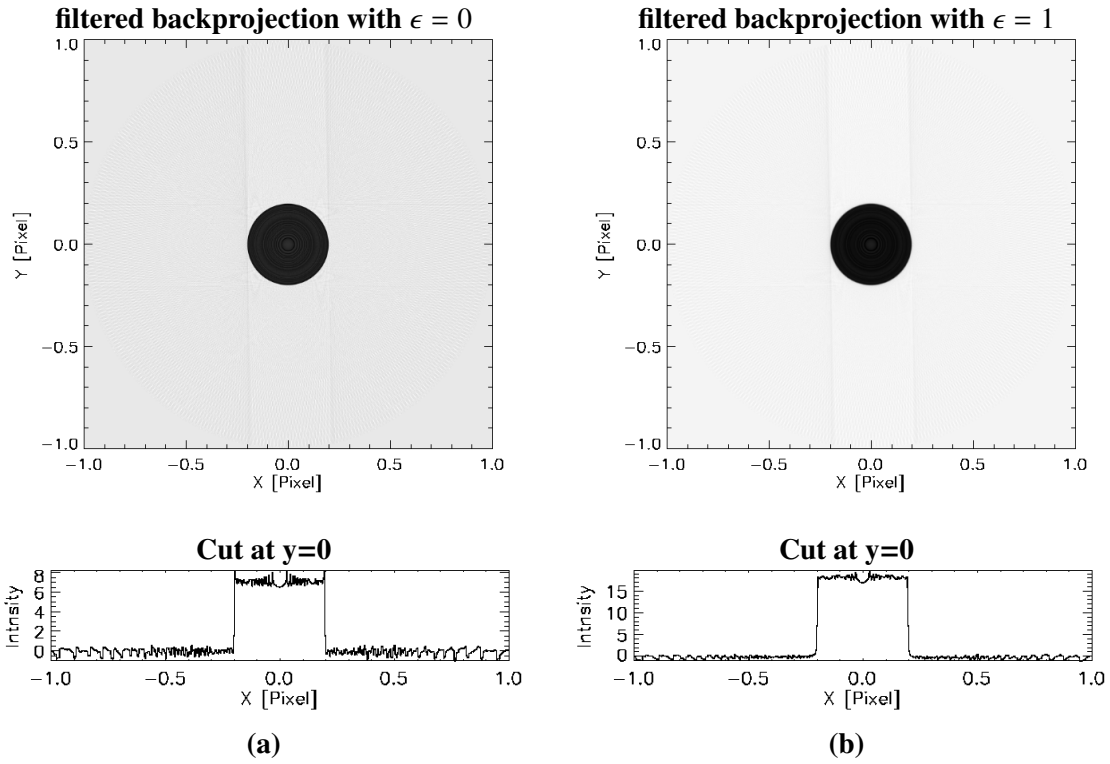

Figure 4.7: Comparison between the basic backprojection reconstruction in Fig. 4.5 and the filtered backprojection reconstruction for $\epsilon = 0$ and 1.

result, thus for the rest of the work we set $\epsilon = 1$.

Tomography requires a continuous set of view directions uniformly distributed over half a rotation. However, SOHO/EIT and SECCHI/EUVI do not produce this continuous set of views and sometimes large temporal gaps can be found in the series of images. To understand the effect on this nonuniformly pattern of view directions, we can consider the following analytical example,

$$\mathrm{D}(\mathbf{x}) = \exp(-\mathbf{x}^2)\ . \tag{4.8}$$

The sinogram (4.3) of (4.8) becomes

$$\mathrm{I}(\varrho, \vartheta) = \exp(-\varrho^2). \tag{4.9}$$

For one view direction ϑ_i, the classical backprojection (4.5) is given by

$$\tilde{\mathrm{D}}_{\vartheta_i}(\mathbf{x}) = \exp(-(\mathbf{e}^{\perp}_{\mathrm{LOS}}(\vartheta_i) \cdot \mathbf{x})^2), \tag{4.10}$$

which is a Gaussian in the direction perpendicular to $\mathbf{e}_{\mathrm{LOS}}$ and constant along $\mathbf{e}_{\mathrm{LOS}}$.

To observe the consequence of a sample set of view directions, we sum over a series of angles $\vartheta_i \in [0, \pi]$ for $i = 1, .., N$:

$$\tilde{\mathrm{D}}(\mathbf{x}) = \frac{1}{N} \sum_{i=1}^{N} \exp(-(\mathbf{e}^{\perp}_{\mathrm{LOS}}(\vartheta_i) \cdot \mathbf{x})^2)\ . \tag{4.11}$$

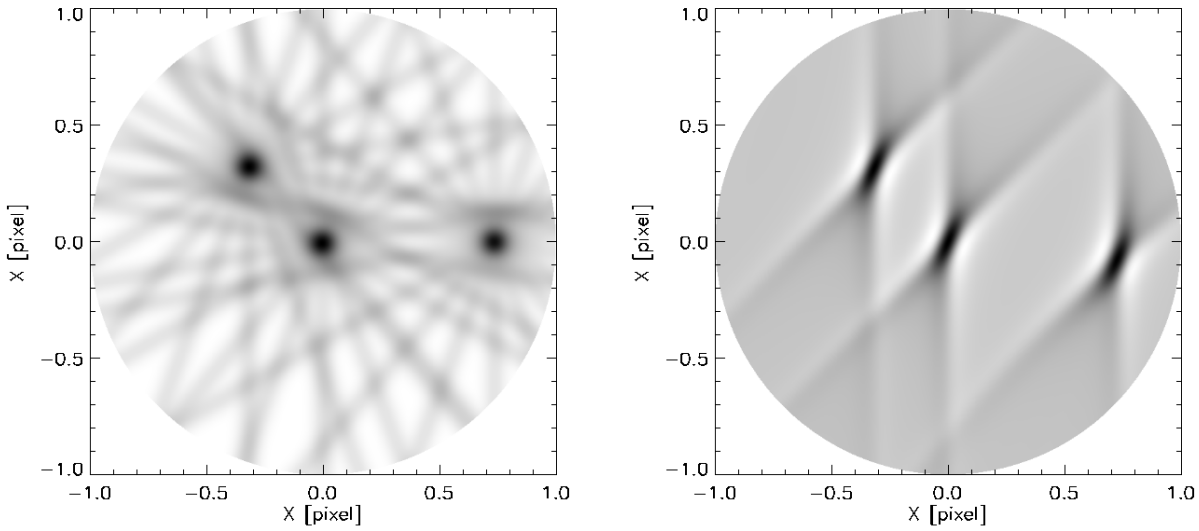

(a) (b)

Figure 4.8: (a) Backprojection result calculated for eight view directions taken every 22.5°. (b) Backprojection result calculated only from projections at $\vartheta = 0°, \ldots, 45°$.

If the number of view directions N is too low, the reconstructed density $\tilde{\mathrm{D}}(\mathbf{x})$ produces a star shape instead of a Gaussian peak given as input (4.8). Fig. 4.8 shows an example for the set views given in Fig. 4.3. The result given in Fig. 4.8 (a) shows the backprojection for only 10 view directions taken every 20°. The reconstructed objects are surrounded by artifacts, which can mislead the interpretation of $\tilde{\mathrm{D}}(\mathbf{x})$.

To observe the consequences of a denser set of view directions but distributed over only a part of the interval $[\vartheta_1, \vartheta_2] \subset [0, \pi]$, we integrate (4.10) over $[\vartheta_1, \vartheta_2]$,

$$\tilde{\mathrm{D}}(\mathbf{x}) = \int_{\vartheta_1}^{\vartheta_2} \exp(-(\mathbf{e}_{\mathrm{LOS}}^{\perp}(\vartheta) \cdot \mathbf{x})^2)\, d\vartheta. \tag{4.12}$$

The result is shown in Fig. 4.8 (b) for the filtered backprojection for $\vartheta_1 = 0°$ up to $\vartheta_2 = 45°$. The objects are reconstructed at the right positions but their shapes are heavily distorted. The major axis of the reconstructed shape is aligned along the mean view direction during the observations.

4.2.2 Tomography for Solar Differential Rotation

As seen in the Introduction (Section 1.1.1), the solar surface does not rotate as a rigid body, but shows an angular velocity varying with latitude. The differential rotation is known (1.1),

$$\omega(\beta) = 14.713 \text{ deg/day } + 2.396 \text{ deg/day } \sin^2(\beta) + 1.787 \text{ deg/day } \sin^4(\beta)\,, \tag{4.13}$$

where ω is the angular velocity in degrees per day and β is the latitude. Depending on the latitude, half a rotation takes between 17.09 days at the pole and 12.23 days at the equator[1]. Fig. 4.9

[1]This is the sidereal rotation period. Later, $\omega(\beta)$ is corrected by including the motions of each spacecraft.

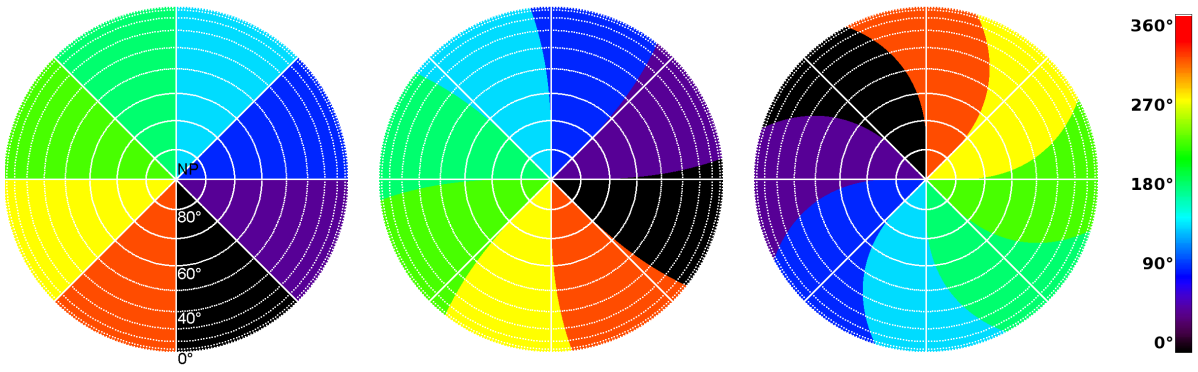

(a) (b) (c)

Figure 4.9: Distortion due to the differential rotation. a) View of the north hemisphere, in the center the rotation axis, the white curve denote the latitude and longitude. (b) shows the distortion produced by the differential rotation (4.13) after about 4.23 days (or a rotation of 45° at the pole) and (c) shows the distortion produced after about 17.09 (half a rotation at the pole).

shows the distortion produced after 4.23 days (or a rotation of 45° at the pole), and after 17.09 days (half a rotation at the pole).

To incorporate the differential rotation (4.13) in the backprojection algorithm (4.7), we have to change the relationship between ϑ and time to take into account the differential angular velocity. The line-of-sight $\mathbf{e}_{\text{LOS}}(\vartheta)$ in (4.4) becomes

$$\mathbf{e}^{\perp}_{\text{LOS}}(\omega(\beta)t) \cdot \mathbf{x} = x\cos(\omega(\beta)t) + y\sin(\omega(\beta)t) = \varrho \,, \tag{4.14}$$

where $\omega(\beta)$ is given by (4.13) and the latitude $\beta = \arcsin\left(\frac{\sqrt{(x^2+y^2)}}{R_\odot}\right)$, with $R_\odot$ the radius of the Sun. The reconstructed density $\tilde{\text{D}}(\mathbf{x})$ is then calculated according to

$$\boxed{\tilde{\text{D}}(\text{x}) = \int_{t=0}^{t=17.09 \text{ days}} \int_{\mathbb{R}} \delta\left(x\cos[\omega(\beta)\, t] + y\sin[\omega(\beta)\, t] - \rho\right) \int_{\mathbb{R}} F(\varrho - \varrho')I(\varrho, \mathbf{e}_{\text{LOS}}(\omega(\beta)\, t))\, d\varrho'\, d\varrho\, dt \,.} \tag{4.15}$$

In Section 4.4 we discuss the outcome from a simulated 3D model and see the effect if the differential rotation is not corrected. To our knowledge this is the first time that the differential rotation is included in a coronal tomography inversion.

4.2.3 Implementation

We assume the density that we are looking for is within the disk on a grid $[-N/2,-N/2]$. For each direction $\vartheta_1, \ldots, \vartheta_p$ uniformly distributed over a half-circle, the projected intensity $\text{I}(\varrho, \vartheta)$

is then sampled at $N+1$ equally spaced points ϱ_n. We define,

$$\mathbf{u}_{\vartheta_j} = (\cos\vartheta_j, \sin\vartheta_j)\,, \quad \text{for} \quad \vartheta_j = \pi\,\frac{(j-1)}{p} \quad \text{with} \quad j = 1, ..., p \tag{4.16}$$

$$\varrho_n = n \quad \text{for} \quad n = -\frac{N}{2}, ..., \frac{N}{2}. \tag{4.17}$$

For each view ϑ_j, $j = 1...p$, we calculate the convolution of $\mathrm{S}(\varrho_n, \vartheta_j)$ with the filter function (4.6):

$$v_{n,j} = \frac{1}{N/2} \sum_{m=-N/2}^{N/2} \mathrm{S}(\varrho_m, \vartheta_j)\mathrm{F}(\varrho_n - \varrho_m)\,, \tag{4.18}$$

where $\mathrm{F}(\varrho_n)$ is the filter function discretized (Natterer, 2001),

$$\mathrm{F}(\varrho_n) = \frac{N^2}{2\pi^2} \begin{cases} \dfrac{1}{4} - \dfrac{\epsilon}{6}, & \text{if } \varrho_n = 0, \\ \dfrac{-\epsilon}{\pi^2\varrho_n^2}, & \text{if } \varrho_n \neq 0 \text{ and } \varrho_n \text{ is even}, \\ \dfrac{-(1-\epsilon)}{\pi^2\varrho_n^2}, & \text{if } \varrho_{\varrho_n} \neq 0 \text{ and } \varrho_n \text{ is odd}\,. \end{cases} \tag{4.19}$$

For each reconstruction point $\mathbf{x}$, we compute the filtered backprojection (4.5). We replace the $\delta-$function by a linear interpolation to the next grid points of the δ-argument $\mathbf{e}^{\perp}_{\mathrm{LOS}}(\vartheta)\cdot\mathbf{x} - \varrho$,

$$\tilde{\mathrm{D}}(\mathbf{x}) = \frac{2\pi}{p} \sum_{j=1}^{p} \sum_{n=-N/2}^{N/2} \Big((1-u_n)\,v_{n,j} + u_n\,v_{n+1,j}\Big)\,, \tag{4.20}$$

where for each $\mathbf{x}$ and j, u_n is determined by,

$$u_n = \begin{cases} \mathbf{u}_{\vartheta_j}\cdot\mathbf{x} - \varrho_n & \text{if} \quad \varrho_n \leq \mathbf{u}_{\vartheta_j}\cdot\mathbf{x} \leq \varrho_n + 1 \\ 0 & \text{if} \quad \mathbf{u}_{\vartheta_j}\cdot\mathbf{x} < \varrho_n \quad \text{and} \quad \mathbf{u}_{\vartheta_j}\cdot\mathbf{x} > \varrho_n + 1\,. \end{cases}$$

4.3 Stereoscopy

Stereoscopy can be considered as a special case of a tomographic problem restricted to only two view directions. It needs a priori identification of characteristic points or ridges and therefore usually requires high-contrast images. As a result, the 3D position of the identified points can be inferred. Two rows in the sinogram (4.3) provide these view directions: $\mathrm{I}(\varrho, \vartheta_1)$ and $\mathrm{I}(\varrho, \vartheta_2)$ for $\vartheta_1 \neq \vartheta_2$. However, two different rows in the sinogram corresponds to observations at two different times. STEREO mission provides observations of the Sun from two different view directions simultaneously. 3D objects on the Sun are projected on the two images SECCHI/EUVI-A and B. Once we have identified the object in both images, we have to solve the inverse problem to reconstruct the 3D object.

In the Section 4.3.1, we describe the basics of triangulation and the correspondence problem. In the Section 4.3.2, we establish a new stereoscopic formulation for reconstructing positions of the 3D plumes. This method was proposed by de Patoul et al. (2011).

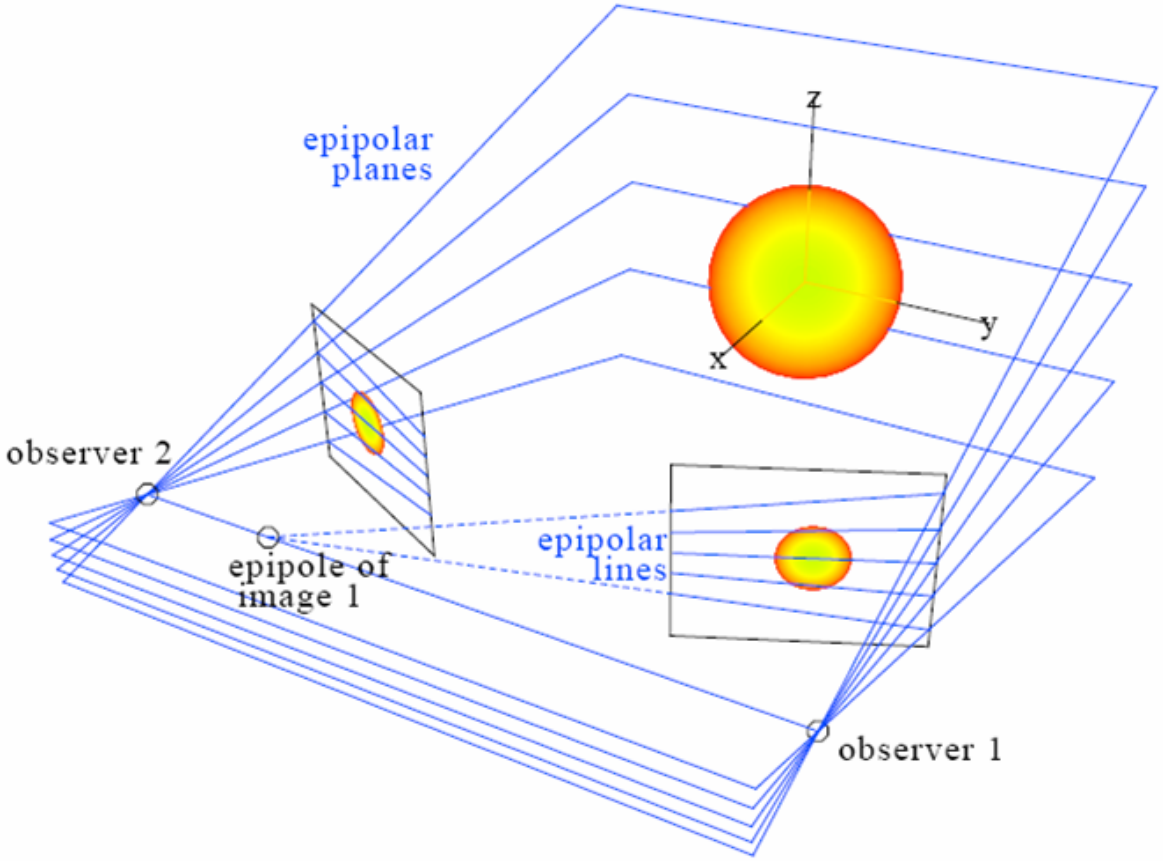

(a)

Figure 4.10: Epipolar geometry: An object on the Sun with the two observer positions defines a plane. This set of planes (in blue) are called *epipolar planes*. The intersection of an epipolar plane and the two projected images (black squares) generate two straight lines called *epipolar line*. (Inhester, 2006)

4.3.1 Triangulation and Correspondence

Stereoscopic reconstruction consists of a purely linear geometrical problem. The basics of the stereoscopy technique for the STEREO mission can be found in Inhester (2006). Here we restrict ourselves to the geometrical method for points and curve-like objects, such as bright points and polar plumes in the corona. For curve-like objects, the backprojection of the selected curves in the images along the two view directions generates two 3D projection surfaces. The intersection of these two surfaces yields a unique 3D curve in the ideal case, which is the solution to the stereoscopic reconstruction.

To calculate this intersection, the epipolar geometry can be used to transform the 3D problem into a set of 2D problems. Any object point P and the two observer positions A and B define an *epipolar plane*. Fig. 4.10 shows a set of epipolar planes, which are formed by different objects on the Sun, and two observers. The intersection of any epipolar plane with images A and B gen-

erates two straight lines (*epipolar lines*). Any point identified in one image on a certain epipolar line must occur on the same epipolar line in the other image (*epipolar constraint*). Fig. 4.11 (a) sketches an epipolar plane with two object points P_1 and P_2 and the two images A and B with the projected points $P_{A.1}, P_{A.2}$ and $P_{B.1}, P_{B.2}$ on image planes A and B, respectively. The depth of an object is proportional to the relative shift along the epipolar line of the two projections (*disparity*).
The major difficulty is to correctly identify the same object in the two stereo images. As shown in Fig. 4.11 (a), P_1 is projected to B_1 in image B and to A_2 in image A. If the correspondences between objects cannot be solved uniquely all possible combinations must be considered as a possible solution. Fig. 4.11 (b) illustrates the backprojection of all combinations and we see that we have two more *ghost* solutions (represented by the black stars).
A finite image resolution leads to reconstruction errors. The uncertainty of the position in the image of a projected object implies that we have to backproject the object along a finite width strip rather than along a line. The reconstructed intersection then yields a trapezoid containing the final 3D plume (see Fig. 4.11 (c)).

4.3.2 Triangulation with Hough-wavelet Coefficients

We will show that the Hough-space coordinates (ρ, θ) of a plume determined for two different view directions directly yields its 3D orientation. From each plume numbering by $p = 0, .., N_i$, detected in image i =A and B, we obtain a set of Hough-parameters: $(\rho_p, \theta_p)_i$. For a specific plume p identified in A and B, the 3D plume axis $\mathcal{P}$ is given by the intersection of two respective backprojection planes $\pi_A[\rho_p, \theta_p]$ and $\pi_B[\rho_p, \theta_p]$,

$$\boxed{\mathcal{P} \equiv \left\{ \mathbf{x} = \begin{pmatrix} x \\ y \\ z \end{pmatrix} ; \;\; \pi_A[\rho_p, \theta_p] \cap \pi_B[\rho_p, \theta_p] \right\}} \tag{4.21}$$

where the planes $\pi_i[\rho_p, \theta_p]$ are given by the Hough-space coordinates (ρ_p, θ_p) of a plume p found from the Hough-wavelet analysis (see Fig. 4.12),

$$\pi_i[\rho_p, \theta_p](s, t) \equiv \mathbf{O}_i + s \left(\mathbf{e}_i + \left(t \, \mathbf{u}^{\perp}_{\theta_{p,i}} + \rho_{p,i} \, \mathbf{u}_{\theta_{p,i}} \right) \Lambda \right) \quad \text{for} \quad s, t \in \mathbb{R} \,, \tag{4.22}$$

where $\mathbf{O}_i$, $\mathbf{e}_i$, $\mathbf{h}_i$ and $\mathbf{v}_i$ are given by the spacecraft position and attitude (see, Section 1.3.3), the factor Λ is defined in Section 1.3.3. Instead of (4.22) we derive in practical calculations the planes $\pi_i[\rho_p, \theta_p]$ slightly differently as we explain below.

The Hough-wavelet procedure additionally gives the scale parameter a for each plume, which is a measure of its apparent width. The scale parameter $a_{p,i}$ could then be looked upon as an effective thickness of the planes $\pi_i[\rho_p, \theta_p]$. The intersection of a pair of planes of finite thickness gives an intersection region elongated with a cross section shape of a parallelepiped.

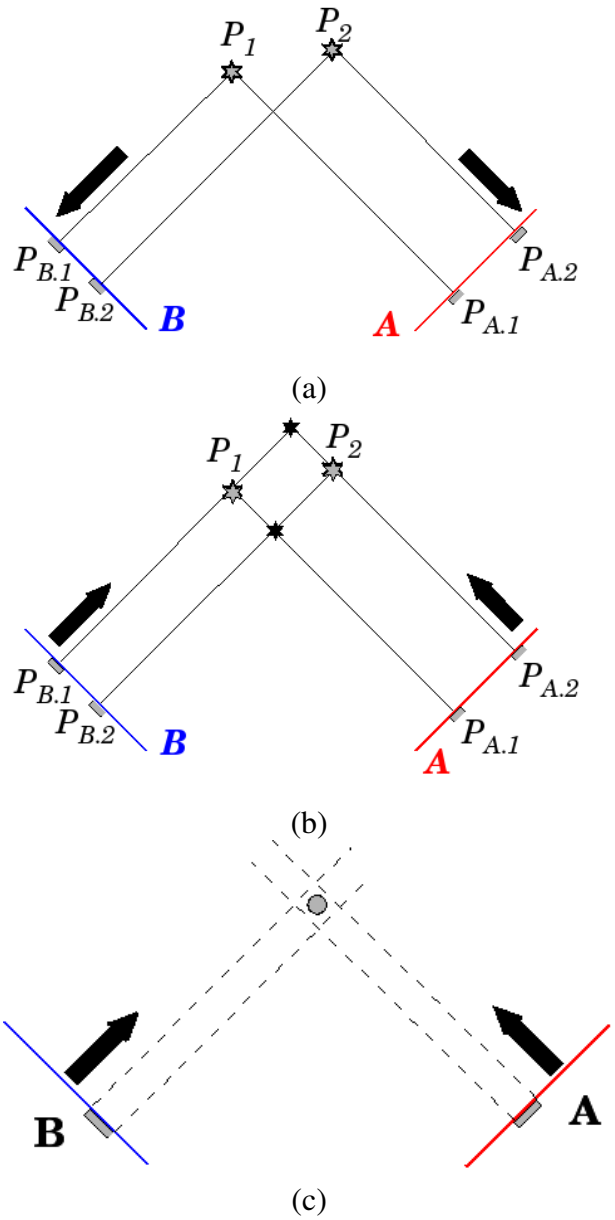

Figure 4.11: (a) Sketch of an image acquisition: P_1 and P_2 are projected into $P_{B.1}$ and $P_{B.2}$ in image B and into $P_{A.1}$ and $P_{A.2}$ in image A. If the correspondences between objects are not solved, the backprojection produces more solutions. (b) Sketch illustrating the backprojection without taking in account the correspondence, we see that we have two additional *ghost* solutions (represented by the black stars). (c) Reconstruction errors: the reconstructed surface intersection yields a column with a trapezoidal cross section containing the final 3D object.

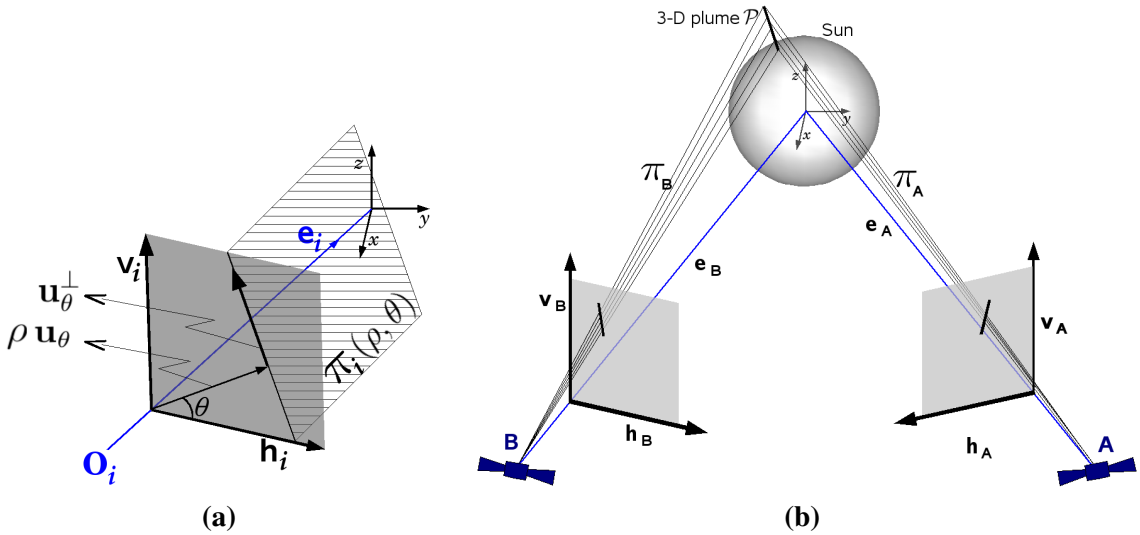

Figure 4.12: (a) Coordinate system of a 3D plan $\pi_i[\rho_p, \theta_p]$ where $\mathbf{O}_i$ is the position of the observer. The 3D unit vector $\mathbf{e}_i$ is the image view direction, $\mathbf{v}_i$ and $\mathbf{h}_i$ are the 3D unit vector directions along the edges of the image orthogonal to $\mathbf{e}_i$. In the image plane $(\mathbf{h}, \mathbf{v})$, $\rho\mathbf{u}_\theta$ is the distance between $\mathbf{O}_i$ and the line, in the direction of $\mathbf{u}_\theta = (\cos\theta, \sin\theta)$. (b) The intersection of the two plans $\pi_A[\rho_p, \theta_p]$ and $\pi_A[\rho_p, \theta_p]$ gives the 3D plume axis $\mathcal{P}$.

While computing the Hough-wavelet transform of a solar image, we eliminated the edge effects by mapping the image into cylindrical coordinates (3.28), i.e.,

$$(s_r, s_\phi) \rightarrow (x(s_r, s_\phi), y(s_r, s_\phi)) \; .$$

In the mapped image i, a plume p with Hough space coordinates $(\rho_p, \theta_p)_i$ implicitly defines the curve (3.30), i.e.,

$$\begin{pmatrix} \cos\theta_{p,i} \\ \sin\theta_{p,i} \end{pmatrix}^\top \cdot \begin{pmatrix} \arctan(x/y)\,(\Delta\phi)^{-1} \\ \left(\sqrt{x^2+y^2} - r_c\right)(\Delta r)^{-1} \end{pmatrix} = \rho_{p,i} \; . \tag{4.23}$$

Since the curves are only slightly bent, we approximate them by a secant line. Practically we find two pairs of points (x_1, y_1) and (x_2, y_2) as solution from (4.23) and redefined our projection planes (4.21) by

$$\pi_i[\rho_p, \theta_p](s,t) \equiv \mathbf{O}_i + s\;\left(\mathbf{e}_i + t\,(\mathbf{h}_i x_1 + \mathbf{v}_i y_1) + (1-t)(\mathbf{h}_i x_2 + \mathbf{v}_i y_2)\right) \; , \tag{4.24}$$

Alternatively, one could solve (4.23) for $y(x)$ and intersect the resulting, slightly curved projection surfaces instead of planes $\pi_A[\rho_p, \theta_p]$ and $\pi_B[\rho_p, \theta_p]$ (4.22).

4.4 3D model and Reconstruction

In this section we discuss the outcome from a simulated 3D model of three idealized plumes rooted at latitude $\beta = 75°, 85°, 65°$ and longitude $\lambda = 225°, 0°, 90°$ respectively and with

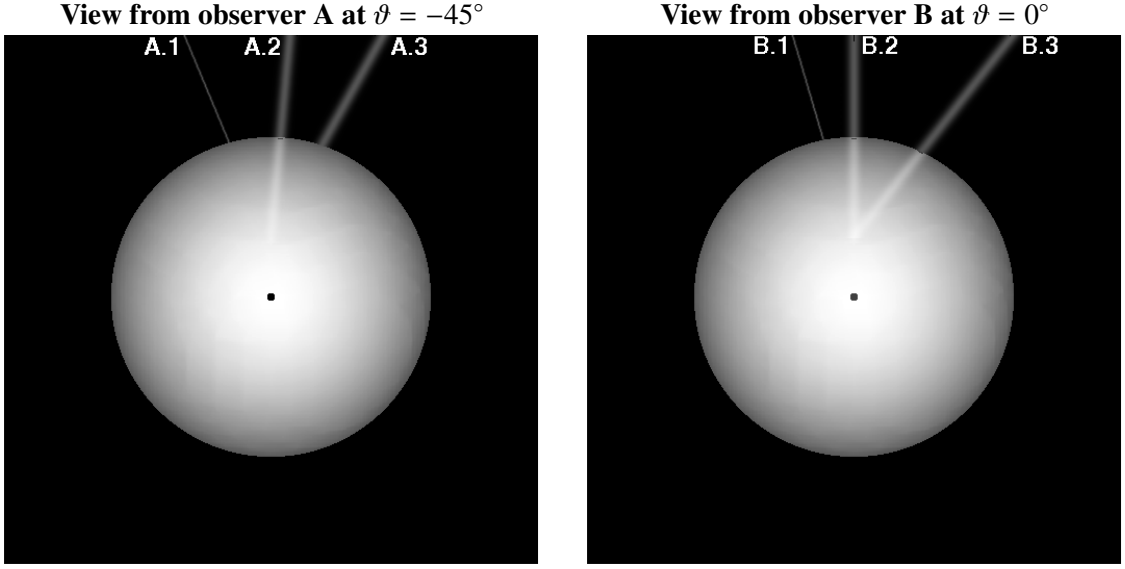

Figure 4.13: Projection of a 3D model seen by two different observers A and B.

Gaussian cross section of width $\sigma = 2$ for the plume located at (λ,β)= $(225°, 75°)$ and 10 for the two other plumes. The plumes expand super-radially with inclination ι proportional to the latitude β: $\iota = \arctan(2\tan\beta)$. For the three plumes the inclination is then given by 82.36°, 87.49° and 76.87° respectively.
We rotate the model and create a set of images $I(\mathbf{x}; t)$ by projecting the model in the same way as shown in Fig. 4.1 (a) (b). Two projections of this model are shown in Fig. 4.13. In order to study the differential rotation effect, the 3D model rotates with the differential rotation according to (4.13), i.e., the rotation angle ϑ is now dependent on latitude β: $\vartheta = \omega(\beta)t$. Moreover, in order to see the effects of non-stationarity, the object located at latitude $\beta = 75°$ has a lifetime limited to a third of a full rotation.
The discussion of this model has been partially published in de Patoul et al. (2011).

4.4.1 Sinogram

The series of images $I(\mathbf{x}; t)$ are mapped to cylindrical coordinates (3.28):

$$\breve{I}(s_r, s_\phi; t) = I(x(s_r, s_\phi), y(s_r, s_\phi); t)$$

where we have set $\Delta\phi = 0.1°$/pixel and $\Delta r = (1.01 - 1.39)/350\ R_\odot$/pixel. We identify the plumes by means of the Hough wavelet transform (3.45) for the scales $a = 1.1, .., 10$ taken with logarithmically equidistant steps, i.e.,

$$HW_{\psi^{MH}}[\breve{I}](\rho, a, \theta; t) = \int_{s_\phi=-350}^{s_\phi=350} \int_{s_r=-175}^{s_r=175} \breve{I}(s_r, s_\phi, t)\, \psi^{MH}_{\rho,a,\theta}(s_r, s_\phi)\, ds_r\, ds_\phi\ , \tag{4.25}$$

where we have restricted the angle θ to $[-35°, 35°]$ and $\rho \in [-350, 350]$ pixels. The Hough-wavelet parameters obtained for the plumes $p = 1, 2, 3$ in the images i =A, B (Fig. 4.13) are

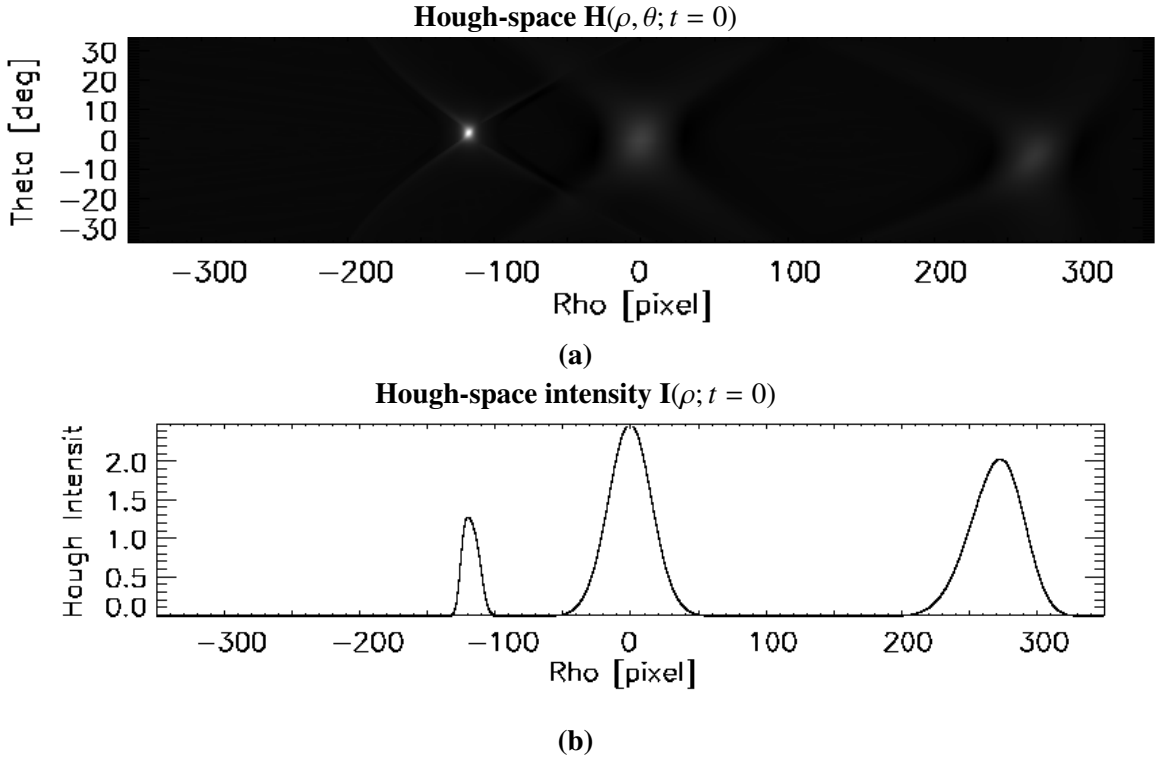

Figure 4.14: Hough-space in (a) and Hough-space intensity in (b) of the 3D plume model.

$(\rho_{p,i}, a_{p,i}, \theta_{p,i})$, see Table 4.1. Then, we obtain the Hough-space (3.47), i.e,

$$\mathrm{H}(\rho, \theta; t) = HW_{\psi^{MH}}[\check{I}](\rho, a_{\mathrm{M}}, \theta; t) \; . \tag{4.26}$$

Fig. 4.14 (a) shows the Hough-space (4.26) for the image Fig. 4.13 B. The three plume peaks are aligned along an inclination line as expected from the superadiality of the plume set as input. Finally, we compute the sinogram (4.1), i.e.,

$$\mathrm{I}(\rho; t) = \int_{-35^\circ}^{35^\circ} \mathrm{H}(\rho, \theta; t)\, \mathrm{W}(\rho, \theta)\, d\theta \; , \tag{4.27}$$

where we set the weighting function $\mathrm{W}(\rho, \theta) = 1$. Fig. 4.14 (b) shows the Hough-space intensity $\mathrm{I}(\rho; t = 0)$ for Fig. 4.13 (b). The resulting sinogram (4.27) is shown in Fig. 4.15. Note that each sinusoids show a small diviation due to the differential rotation od the model.

4.4.2 Filtered Backprojection Reconstruction

The Hough-wavelet density $\mathrm{D}(\mathbf{x})$ is then evaluated with the filtered backprojection (4.15), which use the sinogram $\mathrm{I}(\rho; t)$ (4.27) as input. The result $\tilde{\mathrm{D}}$ is shown in Fig. 4.16 (a). Since the angles $\theta_{p,i}$ are small and therefore the plumes are nearly radial, $\tilde{\mathrm{D}}$ corresponds approximately to the

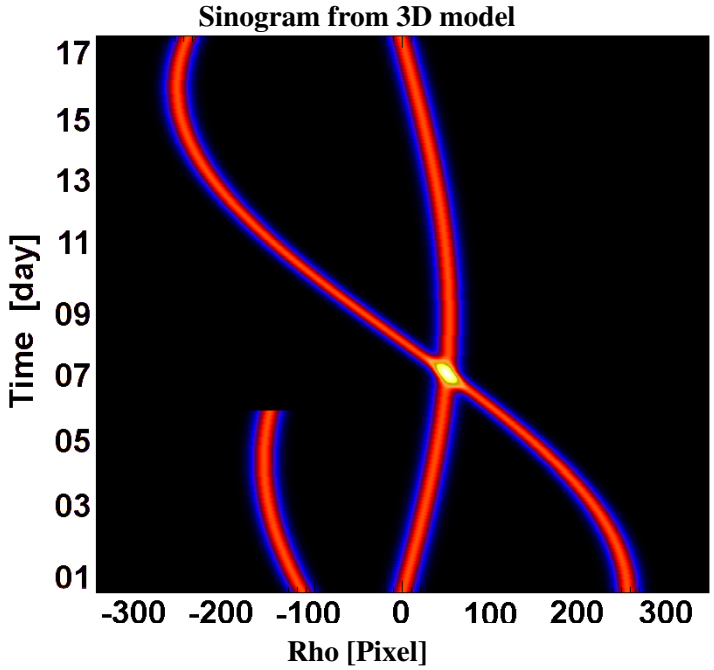

Figure 4.15: Sinogram computed for the synthetic 3D model to which Fig.4.14(a) shows a projection. One of the events lasts only for the first 60 degrees.

orthographic projection of the 3D plume density. The footpoint locations of the three plumes are well retrieved except for the plume at lower latitude. The 3D model was built with a solar differential rotation and therefore at lower latitude the objects on the surface turn faster, which explains the deviation for the location of the plume at 65° latitude. While the plume cross section close to the center corresponds to the Gaussian shape, which was set as input, the two other cross section plumes show a distortion. The distortion is due to both the solar differential rotation of the model and the fact that one plume has short lifetime (plume at 75° latitude).

Fig. 4.16 (b) shows the result computed with the filtered backprojection including the differential rotation as in (4.15). By taking differential rotation into account, we clearly improve the reconstruction. However, for a short-lived object, a similar remedy is not at hand. The shape of the reconstructed cross section is elongated with the major axis aligned along the mean view direction during the lifetime of the plume.

4.4.3 Stereoscopic Reconstruction

For our test calculations, we use two projections of the 3D model in the direction of an observer A at $\vartheta = -45°$ and an observer B at $\vartheta = 0°$. Fig. 4.13 shows the projection of the model seen by A and B.

With (4.24), we calculate the pairs of projection planes $\pi_i[\rho_p, \theta_p]$ and find the 3D axes where they intersect. Table 4.1 gives the longitudes and latitudes corresponding to the intersection of the 3D

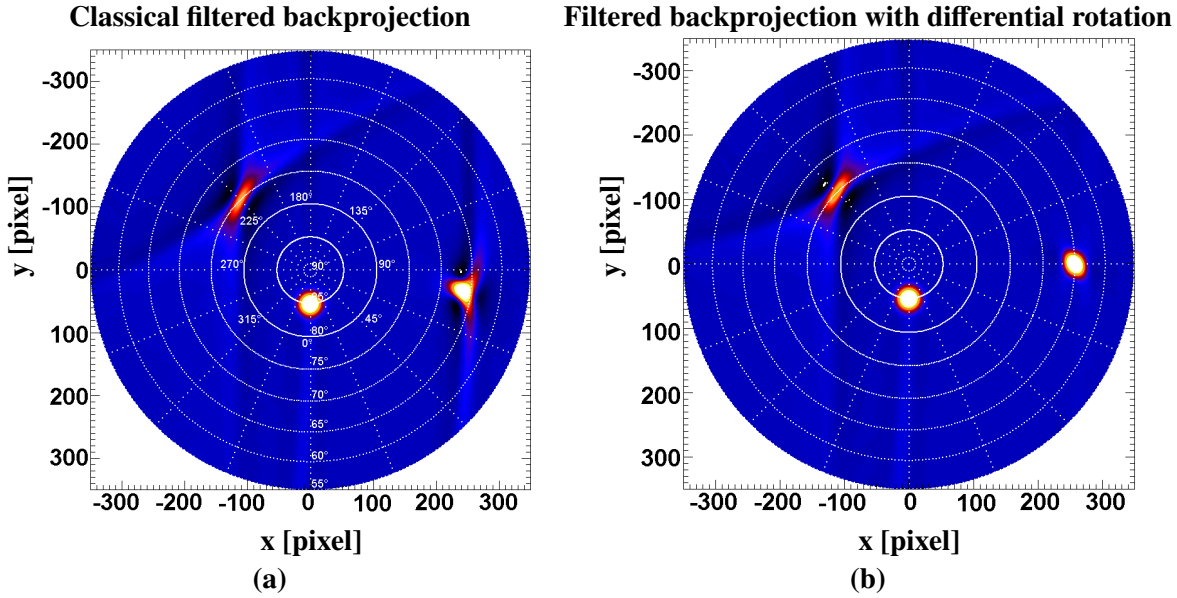

Figure 4.16: Filtered backprojection computed for 180 degree of the 3D model. The model turn clock wise and the view direction is downward the image at 0° longitude. The result is shown from 90° latitude in the center to 55° latitude. (a) Filtered backprojection computed the classical way without taking into account the differential rotation. (b) Filtered backprojection with differential rotation applied as in (4.15).

axes with the Sun surface. Since we did not select any correspondence between the objects in images A and B, we also obtain ghost solutions. Fig. 4.17 shows an orthographic projection of the Sun's north pole with the projection plane intersections:

$$\pi_A[\rho_1,\theta_1]\cap\pi_B[\rho_1,\theta_1]\ ,\quad \pi_A[\rho_2,\theta_2]\cap\pi_B[\rho_2,\theta_2] \text{ and } \pi_A[\rho_3,\theta_3]\cap\pi_B[\rho_3,\theta_3]\ .$$

The thickness of the strips corresponds to the scale width $a_{p,i}$ and the intersection of the strips marks the polygone area where the plume has to reside. There is a small deviation of few degree (an error of $\pm 0.7°$) between the location set as in put and the values in the table

One way to distinguish the true location from the ghost solutions is to compare the calculated footpoint location and axis orientation of the plume with their most probable values. We expect that plumes are orientated along the coronal magnetic field and their axes should be closely aligned along the field lines from a first-order of polar cap field model. For this purpose, we describe the plume axis orientation in terms of angles relative to the local spherical coordinates system: $\mathbf{e}_r, \mathbf{e}_\beta, \mathbf{e}_\lambda$(see Fig. 4.18). The meridian angle m and the inclination angle ι are

$$\text{Inclination angle:} \qquad \iota = \arccos(\mathbf{e}_{obs}\cdot\mathbf{e}_\beta)\ , \tag{4.28}$$

$$\text{Meridian angle:} \qquad m = \arccos(\mathbf{e}_{proj}\cdot\mathbf{e}_{obs})\ , \tag{4.29}$$

where $\mathbf{e}_{obs}$ is the direction of the 3D axes, $\mathbf{e}_{proj}$ is its projection on the meridian plane passing by the footpoint of the plume. The results of ι and m found for the 3D model are given in

p_A	p_B	$(\rho, a, \theta)_A$	$(\rho, a, \theta)_B$	ι	m	λ	β
1	**1**	**(-164.00, 2.82 4.00)**	**(-119.00, 2.82 4.00)**	**82.27**	**0.16**	**225.13**	**74.86**
2	1	(37.00, 5.66, -0.50)	(-119.00, 2.82 4.00)	81.47	0.44	325.32	71.52
3	1	(202.00, 5.66, -4.00)	(-119.00, 2.82 4.00)	76.84	0.64	344.45	56.73
1	2	(-164.00, 2.82 4.00)	(0.00, 5.66, 0.50)	80.82	1.28	179.21	69.17
2	**2**	**(37.00, 5.66, -0.50)**	**(0.00, 5.66, 0.50)**	**87.08**	**1.37**	**0.59**	**85.28**
3	2	(202.00, 5.66, -4.00)	(0.00, 5.66, 0.50)	79.08	1.26	0.72	64.84
1	3	(-164.00, 2.82 4.00)	(-268, 5.66, -5.00)	–	–	–	–
2	3	(37.00, 5.66, -0.50)	(-268, 5.66, -5.00)	79.04	0.14	129.64	59.12
3	**3**	**(202.00, 5.66, -4.00)**	**(-268, 5.66, -5.00)**	**77.74**	**0.88**	**89.86**	**64.67**

Table 4.1: Stereoscopic solutions for the 3D model. The first two columns are the plume numbers identified in image A and B. The next two columns give the Hough-wavelet parameters associated. ι is the inclination angle of the 3D axes and m is the meridian angle. The last two columns give the longitude and latitude of the plume footpoints. The bolt rows are the plume set as input for the 3D model. The dash lines are the case where no intersection with the sphere were found or the intersection was too low in latitude.

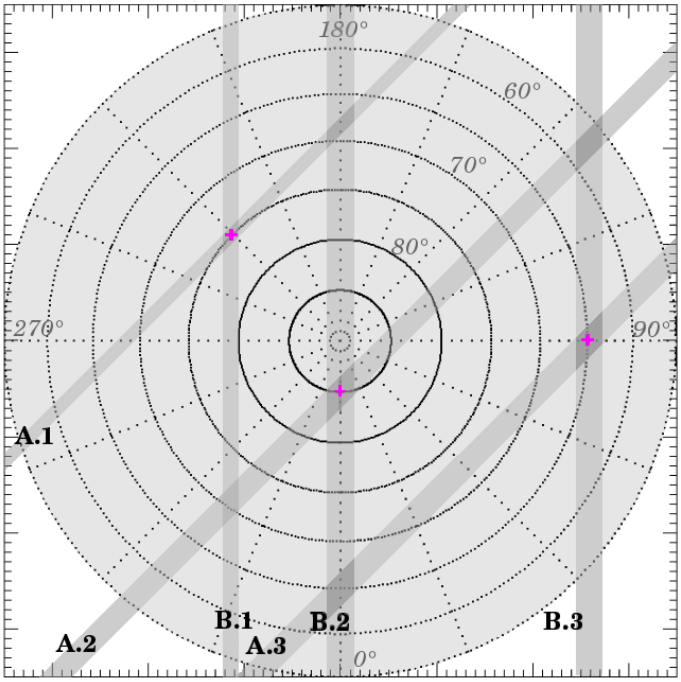

Figure 4.17: Stereoscopic solutions from Table 4.1. View from the top of the Sun. The intersection of the strips gives the parallelepiped, within which the plume has to reside. The red crosses indicate the footpoint positions of the three plumes of the 3D model. Since we did not make any correspondence between the objects in image A and B, we have ghost solutions.

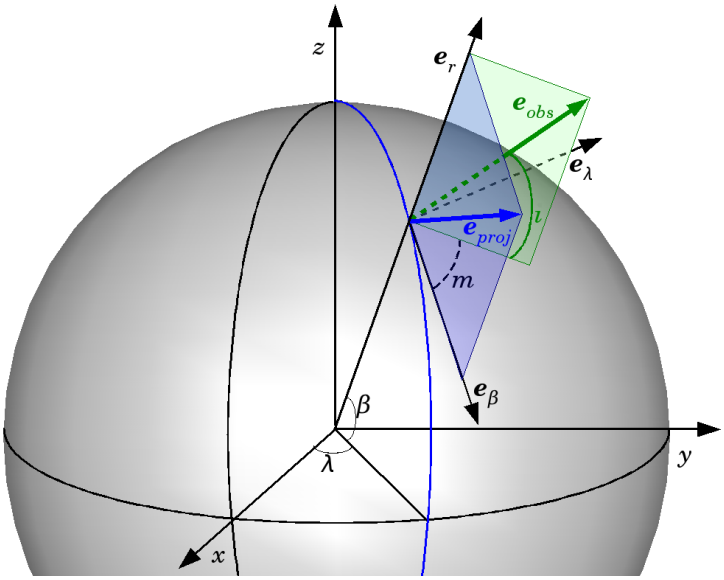

Figure 4.18: Local spherical coordinate ($\mathbf{e}_r, \mathbf{e}_\beta, \mathbf{e}_\lambda$) system at the footpoint of a plume. $\mathbf{e}_{obs}$ is the plume axis orientation, m is its meridian angle, ι is its inclination angle and $\mathbf{e}_{proj}$ is its projection on the meridian plane.

Table 4.1. For the inclination angle, we have an error of ±1.12° and for the meridian angle we have an error of ±1.50°. The ghost can only be identified this way if the values for m and ι deviate from expected field deviation by about 3 times these errors. Moreover, we show later that the polar coronal flux distribution is not symmetric with respect to the heliospheric. The cap field inclination in the corona may well differ from symmetric field by 4-5°, which increases the error bar. Adding a third view direction to the stereoscopic analysis could drastically reduce the number of ghost solutions. The second way to verify the stereoscopy results is to compare them with tomography results as shown in Fig. 4.19. For solar plumes analysis, we will quantify the correspondence between plume combinations by considering all these aspects.

4.5 Summary and Conclusion

In this chapter we developed two imaging techniques to retrieve the 3D orientation and shape of coronal plumes. We use tomography to reconstruct the density and cross section shape of plumes and stereoscopy to retrieve their orientation axes.

Since plumes are faint in EUV images, first we identify them in EUV images by the means of the Hough-wavelet transform presented in Chapter 3. We have shown here that Hough-wavelet transform is a convenient tool to be used as input for the 3D reconstructions.

The tomographic reconstruction proposed here is the filtered backprojection using the Hough-wavelet coefficients as input instead of the image intensity. This approach has the advantage of

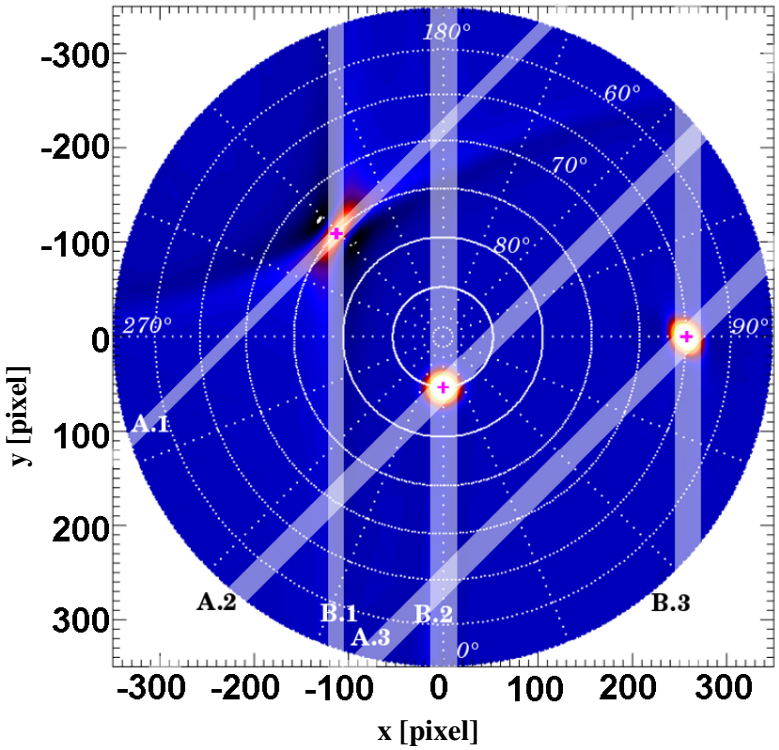

Figure 4.19: Tomography result where we overlap stereoscopy result.

reducing our problem to 2D. With the help of a simulated 3D plume model, we have discussed the error in the outcomes of filtered backprojection when the implicit assumptions – solid rotation of the global corona and stationarity of the coronal structures as the Sun rotates – do not hold. We have seen that the non-stationarity of plume structures produces a distortion of the plume cross section in the direction of the observer. Since the differential rotation is known, we have included it in the tomography formulation.

The stereoscopic procedure has also been reformulated in order to use the Hough-wavelet parameters for the reconstruction of the 3D plume axes. We have shown in the 3D plume model that it is not straightforward to solve the correspondence problem. Additional criteria are necessary to sort out the correct solutions such as footpoint locations, and most probable inclination and meridian angles of the plume axes.

Finally we have shown that both, tomographic and stereoscopic techniques are complementary to identify 3D plume structures for solving the correspondence problem and non-stationarity.

Part III

Plume Study

Chapter 5
Plume Identification and Temporal Evolution in 2D

Polar plumes are elongated, 3D plasma structures above coronal holes lasting for a few days up to a few weeks. They co-rotate with the solar corona and therefore change their aspect with respect to a fixed observer throughout the rotation.

In this chapter, we analyze their projections in sequences of EUV images, at 171 Å taken nearly simultaneously by the three spacecraft telescopes STEREO/EUVI A and B, and SOHO/EIT. An example of these images are shown in Fig. 5.1.

In Section 5.1, we describe a number of image pre-processing procedures which need to be carried out before applying an identification algorithm. In Section 5.2, we identify plumes close to the limb from 1.01 $R_\odot$ to 1.39 $R_\odot$ in a single image with the Hough-wavelet method presented in Chapter 3. Finally, in Section 5.3, we apply the method to the data set obtained from one year of observation and perform a sinogram. The identification result is then compared to a basic dipole magnetic field model of the Sun.

5.1 Image Pre-Processing

A number of image pre-processing procedures are necessary for suppressing most of the instrumental and non-solar features in the image. It is also necessary to calibrate the images in order to be suitable for directly comparing them within a time series. For solar data, Aschwanden (2010) gave a long list of aspects that need to be taken into account in the pre-processing process. As mentioned previously, EUVI and EIT data are calibrated by the standard calibration programs *secchi_prep* and *eit_prep* from the SolarSoft library (Freeland and Handy, 1998). Afterwards, we apply two more procedures necessary for our analysis, which is described here.

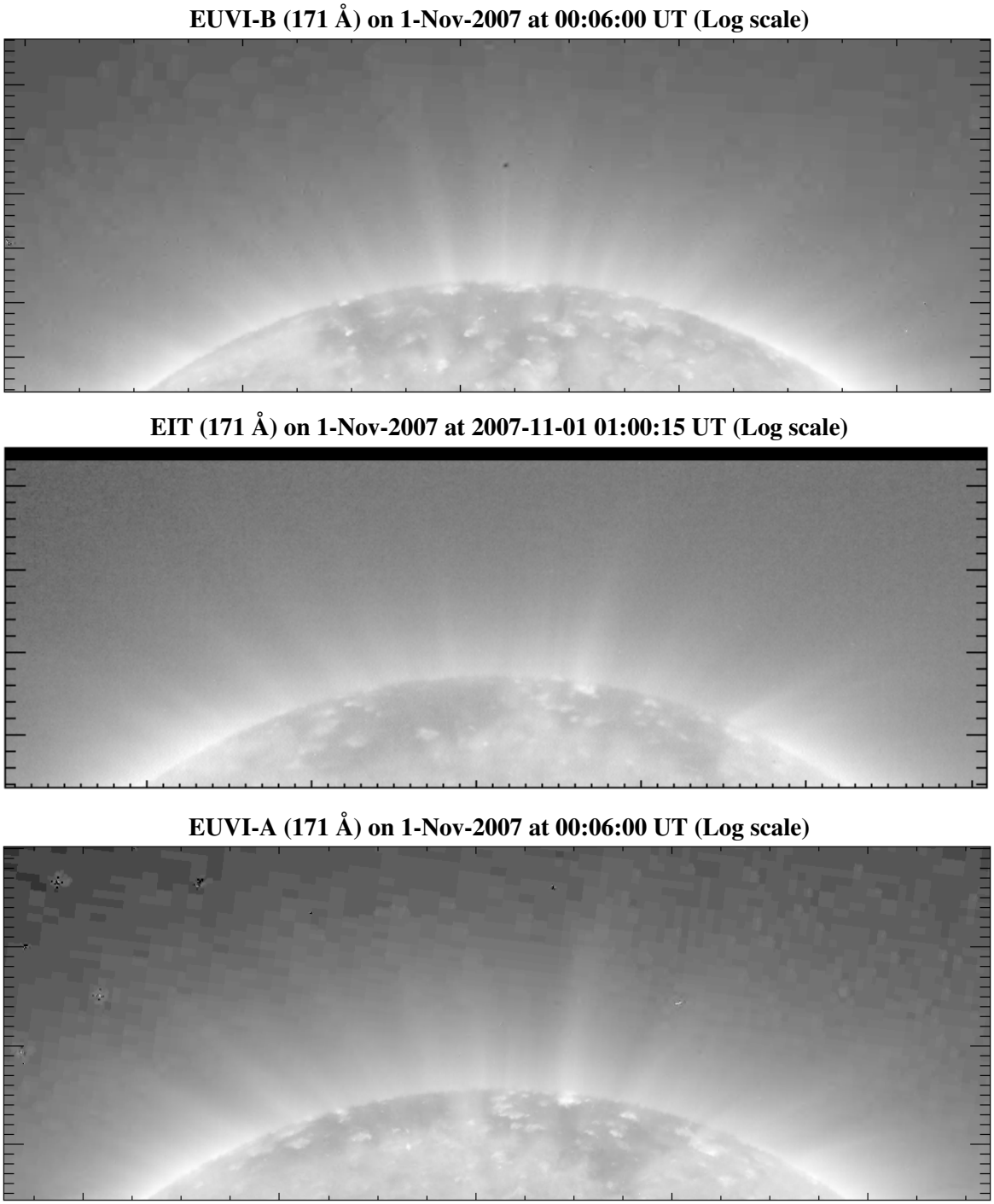

Figure 5.1: Intensity map of the solar corona during the minimum of the solar cycle.

5.1.1 Non-solar Feature Removal

In the introduction (Section 1.3.2), we presented different types of noise affecting the image which remain after the calibration procedure. The photon noise and read-out noise are isotropic and they act at smaller scales and lower intensities compared to plume features. By choosing the Hough-wavelet method, which is a directional multiscale analysis, and by considering scales large enough, these two types of noise do not affect the results.

The cosmic ray hits, which show a particularly high intensity compared to the off-disc intensity level, can disturb the results. We remove cosmic ray hits by using a method proposed by de Patoul et al. (2011): it employs a basic median filter with a box of 5×5 pixels iterated three times on the image. Cosmic ray pixels are considered to have values larger than 3σ of the median-filtered image neighborhood. These pixel values are subsequently compared with those of the image observed at the previous time to clearly identify the pixel as cosmic ray and not as a persistent local enhancement due to a solar event. Pixels identified as cosmic ray hits are simply replaced by the local median value.

Another method has been proposed by Jacques (2004) and Antoine et al. (2002). They use as an hypothesis that a cosmic ray hit is comparable to a Dirac function which is uncorrelated to its neighborhood. They identify them by analyzing the local regularity of the signal by the means of the Hölder exponent. The method gives good results on EIT data. However, since EUVI uses ICER compression, sharp high intensity features such as cosmic ray hits are affected by the aliasing effect and therefore no longer appear as Dirac points. For consistency of the study we apply the basic method given by de Patoul et al. (2011) to the data from the three instuments EUVI-A, B and EIT.

Additionally, a few pixels with negative values have been found after looking at several images. Some of them are found in the corners, where noise dominates the signal. Since they are far away from the region of interest, they are excluded from the study. However, some of these pixels with negative values were found in the neighborhood of a cosmic ray hit probably due to the image compression. To remove them, we simply use the same procedure as for the cosmic ray hits.

Finally, the missing blocks in EIT data remain a problem. The header usually gives the number of missing blocks, but not their locations. We do not add any special procedure to correct the missing blocks. We will see by an example that one or two missing blocks in the region of interest do not affect the global results significantly. However, if we have more missing blocks, the results become inconsistent and the whole image needs to be rejected.

5.1.2 Contrast-enhancement Technique

As we can see in Fig. 5.1, plumes appear very faintly in EUV images. To overcome this aspect, we use the contrast-enhancement procedure proposed by de Patoul et al. (2011). A background image $B(\mathbf{x})$, where $\mathbf{x}$ represents pixels in a 2D image, is accumulated from a set of images $I(\mathbf{x};t)$

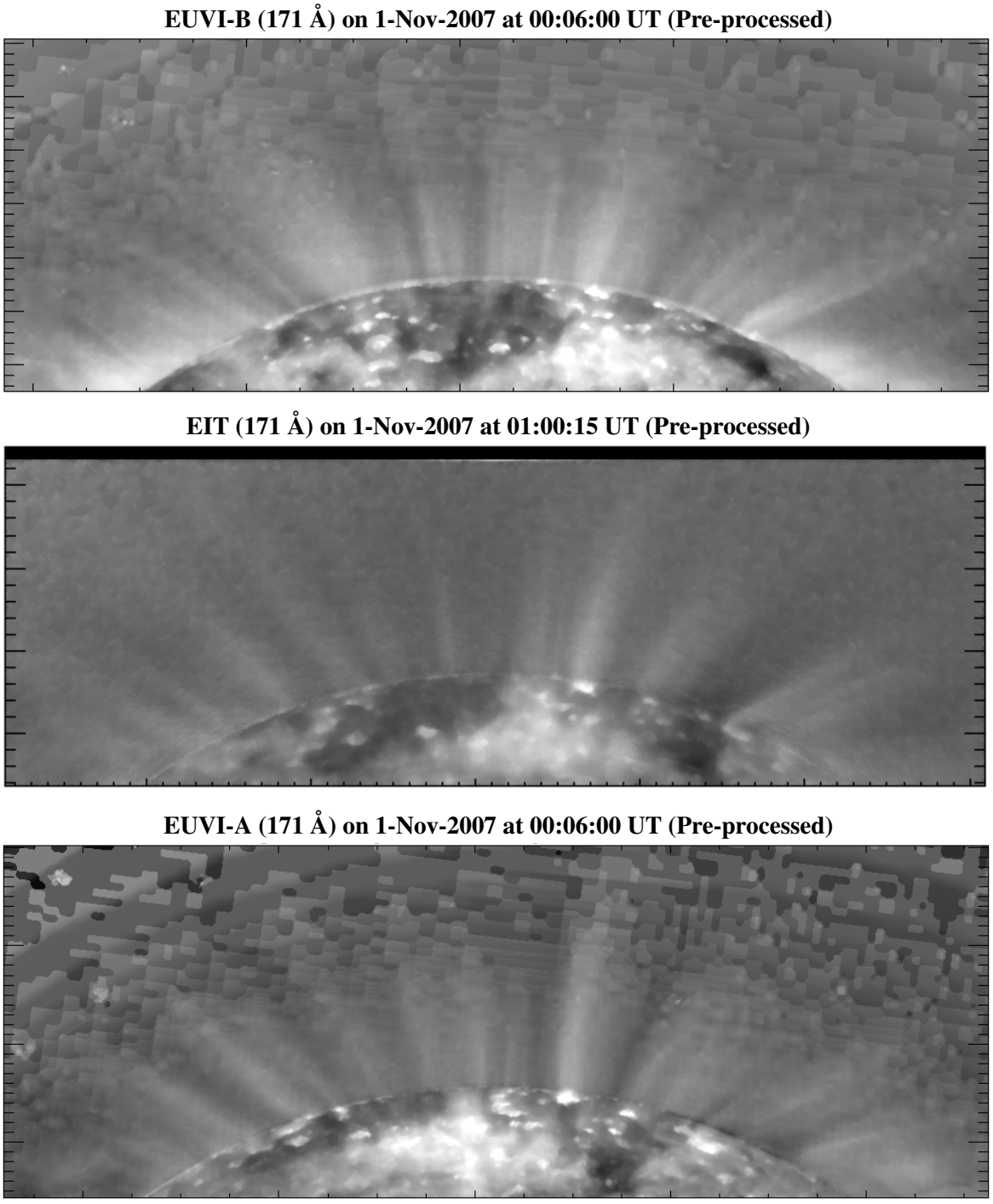

Figure 5.2: Same images as shown in Fig. 5.1 after applying the cosmic ray hits removal and contrast-enhancement procedures.

observed at time t according to the following prescription:

$$B(\mathbf{x}, t) = \min_{t' \in [t-15 \text{ days}\,,\; t+15 \text{ days}]} \{\ \text{median}_{t'' \in [t'-12 \text{ hours}\,,\; t'+12 \text{ hours}]}\ \ I(\mathbf{x}, t'')\ \}.$$

From each image $I(\mathbf{x}; t)$, a new enhanced image $\tilde{I}(\mathbf{x}; t)$ is obtained from,

$$\tilde{I}(\mathbf{x}; t) = \begin{cases} \dfrac{I(\mathbf{x}; t) - B(\mathbf{x})}{B(\mathbf{x})} & \text{for } \mathbf{x} \text{ such as } I(\mathbf{x}; t) \geqslant 0, \\ -1 & \text{for } \mathbf{x} \text{ such as } I(\mathbf{x}; t) < 0. \end{cases} \tag{5.1}$$

A slightly more sophisticated background subtraction and contrast enhancement for different scale features using Haar wavelets, has been proposed by Stenborg and Cobelli (2003) and Stenborg et al. (2008). However, by using the Haar wavelet, the image intensity is locally modified and it cannot be ruled out that the intensity of a plume is changed inhomogeneously or that the plume is even entirely suppressed. Keeping the background subtraction method simple the procedure gives, nevertheless, a satisfactory enhancement of the plume signal in EUV images (see Fig. 5.2).

5.2 Plumes in the Hough-wavelet Space

Once the images are pre-processed, we apply the multiscale analysis in the same way as presented in the example in Section 4.4. We consider subframes of the pre-processed images $\tilde{I}(\mathbf{x}; t)$, which represent the solar polar cap, for the radial distance r from $r_1 = 1.01\ R_\odot$ to $r_2 = 1.39\ R_\odot$ and for the angles $\phi \in [-35°, 35°]$ from the northern solar rotation axis and $\phi \in [145°, 215°]$ in the southern pole. When we map the subframes to cylindrical coordinates (3.28), i.e.,

$$\breve{I}(s_r, s_\phi; t) = \tilde{I}(x(s_r, s_\phi), y(s_r, s_\phi); t) \qquad \text{with} \qquad (s_r, s_\phi) = \left(\frac{(r - r_c)}{\Delta r}, \frac{\phi}{\Delta \phi} \right),$$

we set the normalization factors to $\Delta\phi = 0.1°/\text{pixel}$ and $\Delta r = 0.001\ R_\odot/\text{pixel}$. r_c was chosen to be $r_c = (r_1 + r_2)/2 = 1.2\ R_\odot$.

The mapped images are then analyzed with the Hough-wavelet transform (3.45), for ρ restricted to $[-350, 350]$ pixels, $\theta \in [-35°, 35°]$ and the scales $a \in [2.00, 10.00]$ pixels varied in logarithmically equidistant steps: The minimum scale, of 2.0 pixels, is small enough to identify thin structures, but large enough to exclude the effective noise from our multiscale analysis. For these selected scales, an equivalent Gaussian width plume structure in the plane of the sky in the original image coordinates (x, y) corresponds to 6.32 Mm for the minimum scale $a = 2.0$ pixels. It corresponds to 43.89 Mm for the maximum scale $a = 10.0$ pixels (see Section 3.4.4), which is reasonable considering the plume observations in the literature (Wilhelm et al., 2011).

Then, for each position (ρ, θ) we determine the optimum scale, a_{M}, (3.46). We obtain the Hough-space (3.47), i.e.,

$$\text{H}(\rho, \theta; t) = HW_{\psi^{MH}}[\breve{I}](\rho, a_{\text{M}}, \theta; t)\ .$$

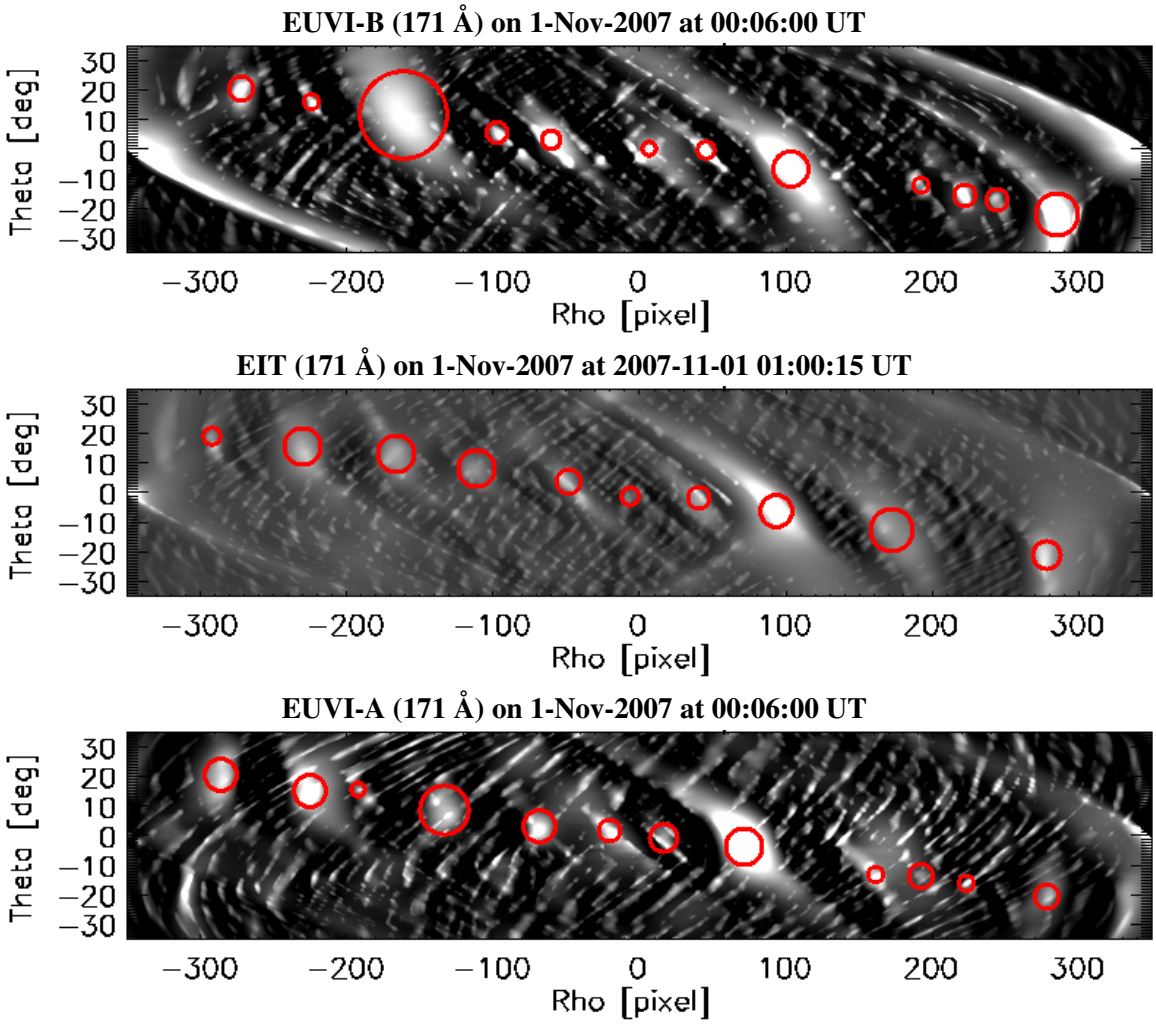

Figure 5.3: Hough-wavelet transform of the image in Fig. 5.2 at the optimum scale a_{M}. The red circles are centered on the local maxima over different scales of the Hough-wavelet coefficients and their radii are proportional to a_{M}.

Fig. 5.3 shows an example of the Hough-space computed for EIT, EUVI-A, and EUVI-B images taken on 1st of November 2008. The centers of the red circles correspond to the local maxima for each of the plume peaks, and the radii of the red circle are proportional the optimum scale a_{M}.

Since the plume peaks located at (ρ, θ) in Hough-space corresponds to straight lines (3.29) in (s_r, s_ϕ)-space, i.e,

$$\begin{pmatrix} \cos\theta \\ \sin\theta \end{pmatrix}^{\top} \cdot \begin{pmatrix} \phi/\Delta\phi \\ (r - r_c)/\Delta r \end{pmatrix} = \rho \ .$$

we can determine the relation between ρ and the latitude $\beta = 90^\circ - |\phi|$,

$$\beta(r) = 90^\circ - \left| \frac{\Delta\phi}{\cos\theta} \left(\rho - \frac{(r - r_c)}{\Delta r} \sin\theta \right) \right| . \tag{5.2}$$

Therefore, for small θ we have $\beta \simeq 90^\circ - |\Delta\phi\ \rho|$ which is $\beta \simeq 90^\circ - 0.1\ |\rho|$ in our coordinate system.

As the Hough-wavelet transform is invertible, the inverse transform is unique. A plume peak with coordinates $(\rho_0, a_{\rm M}(\rho_0, \theta_0), \theta_0)$ in the Hough-wavelet space corresponds to a strip in (s_r, s_ϕ) of width proportional to $a_{\rm M}$ inclined by an angle θ_0 at distance ρ_0 from $(r_c, 0)$. Fig. 5.4 shows the inverse transform where the yellow lines indicate the ridge of the detected plume peaks and the green curves represent the width of the plume given by the scale. The yellow curves are not straight because the Hough-wavelet transform was applied to the image after the mapping to cylindrical coordinates. Fig. 5.5 shows the result for the north and the south pole. The yellow curves are the ridges of the detected plumes (same as Fig. 5.4 for the north pole). The red lines are the prolongations of the reconstructed plume axes. We see that plumes are close to linear structures, which converge approximately at a point on the solar rotation axis more than half the way between the center of the Sun and the poles. This is typical for near-dipole magnetic field lines.

In Hough-space, the plume peaks are aligned along an inclined line as we can see in Fig. 5.3. This is due to the super-radial inclination of the plumes. If we assume that the plume peaks are aligned along a straight line, we have

$$\theta \ = \ u \ \rho \ + \ v \, . \tag{5.3}$$

The slope u is in units of degree/pixel and gives an estimation of the superadiality of the plumes in the plane of the sky. The intercept v in degrees is the inclination of the plumes rooted in the rotation axis. The ρ-intercept (i.e. $-v/u$) gives the positions where plumes are radial. A zero ρ-intercept value means that the dipole magnetic axis is aligned with the rotation axis of the Sun on the projected images. To evaluate u and v, we use the Hough transform method in its conventional way, which is the identification of lines in an image. For the EUVI-A image in Fig. 5.3, we obtain a slope of $u = -0.15$ degrees/pixel and the ρ-intercept= $-v/u = 4.45 \pm 0.5$ pixels, which corresponds to $\phi = 0.44^\circ \pm 0.05^\circ$. In the following section, we estimate u and v for a larger series of images and see their evolution over a year.

5.3 Time Series and Sinogram

We consider a sequence of EUVI and EIT images taken at 171 Å during 12 months from May 2007 to March 2008 (see Table 5.1). We also look at the data in February 2011 to test our procedure. The time cadence for the EUVI images was on average 20 minutes. Whereas the cadence for EIT images was on average 6 hours, except when there was a campaign with a

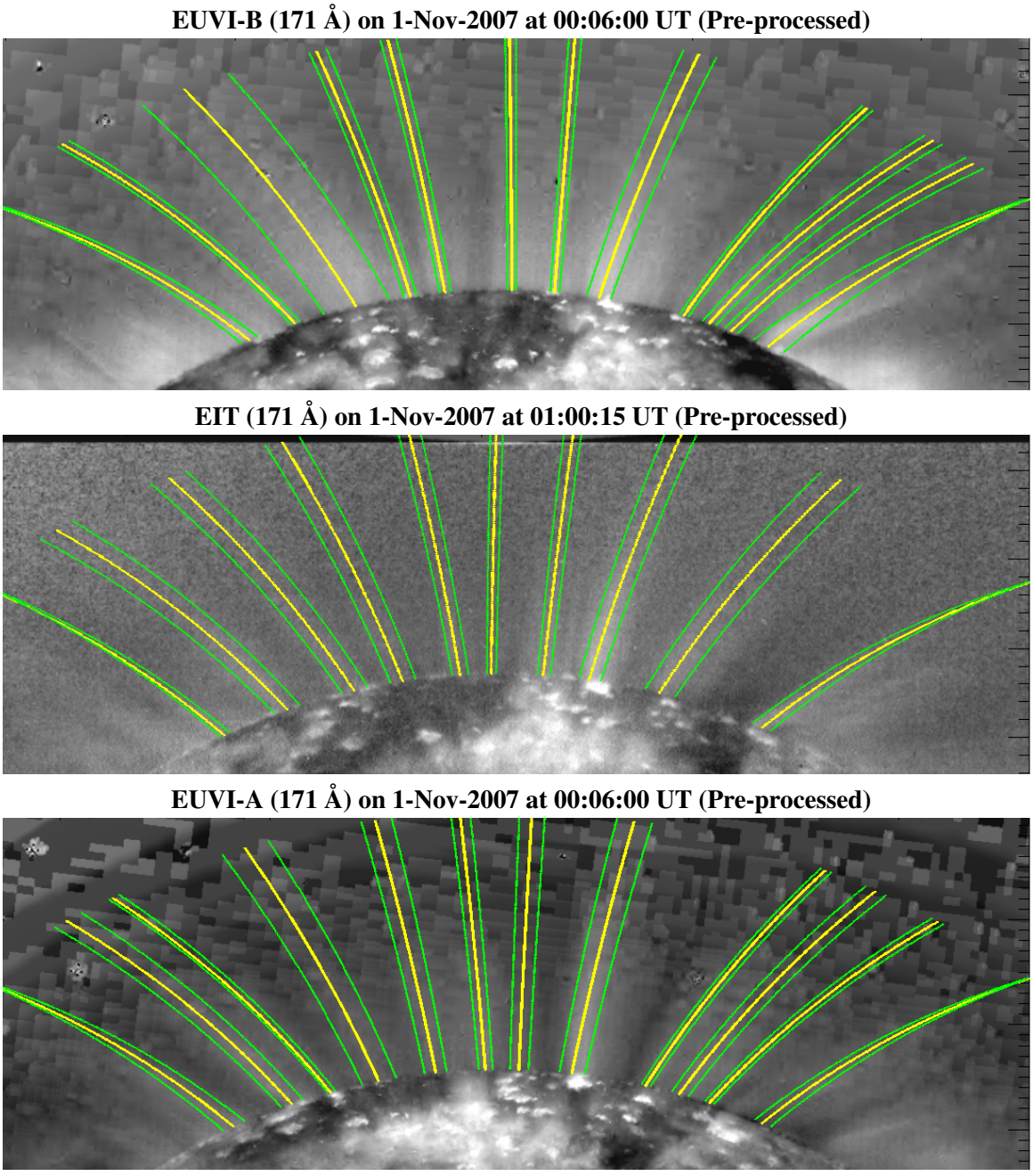

Figure 5.4: The Hough-wavelet backward transformation of polar plumes on the coronal image. The yellow lines correspond to local maxima in the Hough-space and the green lines to the computed width of the plume.

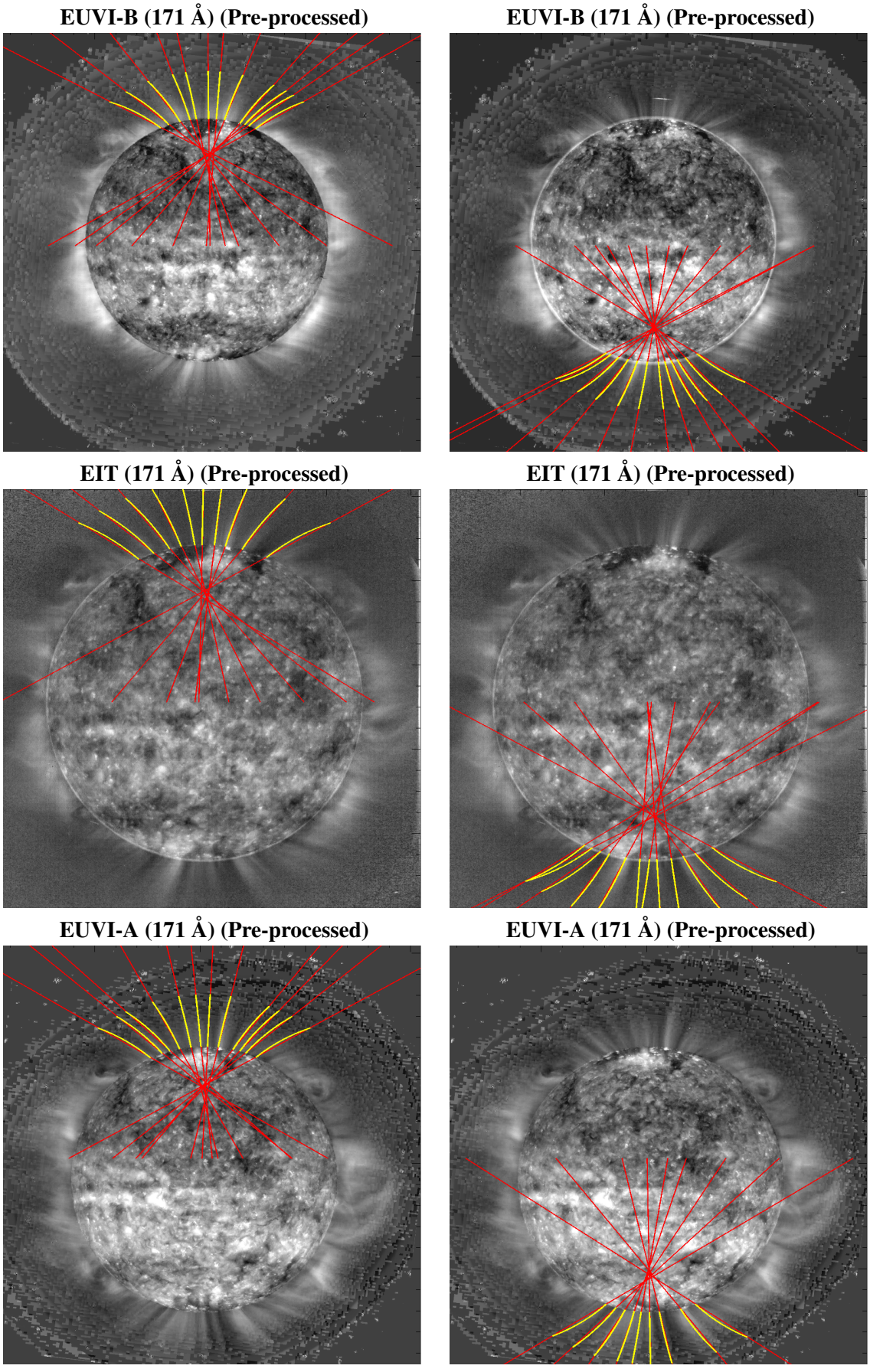

Figure 5.5: Solar images from Fig. 5.4 with the Hough-wavelet backward transformation results in yellow and the prolongation of the reconstructed plume in red.

Time	STEREO-B lon.°, lat.°	SOHO-E lon.°, lat.°	STEREO-A lon.°, lat.°	Separation Angle [degree]		
				B-E	E-A	B-A
2007-05-01	-1.84, -4.66	0.00, -4.21	4.19, -3.74	1.89	4.21	6.08
2007-06-01	-3.68, -1.48	0.00, -0.72	6.78, 0.23	3.76	6.84	10.60
2007-07-01	-6.12, 1.82	0.00, 2.82	9.75, 4.03	6.19	9.81	16.01
2007-08-01	-09.20, 4.79	0.00, 5.75	13.02, 6.75	9.21	12.97	22.19
2007-09-01	-12.61, 6.75	0.00, 7.19	15.99, 7.26	12.52	15.87	28.39
2007-10-01	-15.87, 7.29	0.00, 6.74	18.19, 5.59	15.76	18.13	33.89
2007-11-01	**-18.83, 6.24**	**0.00, 4.43**	**19.65, 2.18**	**18.83**	**19.74**	**38.57**
2007-12-01	-21.05, 3.75	0.00, 0.94	20.49, -1.75	21.22	20.66	41.88
2008-01-01	-22.63, 0.14	0.00, -2.95	21.11, -5.27	22.84	21.18	44.02
2008-02-01	-23.54, -3.62	0.00, -5.98	21.76, -7.18	23.57	21.65	45.23
2008-03-01	-23.85, -6.26	0.00, -7.23	22.59, -6.99	23.71	22.41	46.11
2008-04-01	-23.87, -7.30	0.000, -6.53	23.87, -4.69	23.70	23.83	47.53
2008-05-01	-24.04, -6.39	0.00, -4.14	25.75, -1.06	24.04	25.90	49.94
2011-02-01	**-92.64, 4.64**	**0.00, -5.99**	**86.72, -4.44**	**93.10**	**86.28**	**179.33**
2011-03-01	-94.57, 1.62	0.00, -7.22	87.45, -1.00	94.73	87.34	182.07

Table 5.1: Positions of STEREO-A, B and the Earth. The longitude and latitude are given in HEEQ (Heliocentric Earth EQuatorial) coordinates. The last three columns are the separation angles between the instruments STEREO-A, EIT-E and STEREO-B. (http://stereo-ssc.nascom.nasa.gov/where/). The two bolded lines correspond to the period or time used to compute the sinograms in Fig. 5.7 and Fig. 5.8.

special cadence of two minutes, for example at the end of November 2007. The Hough-wavelet procedure described above is applied to these series of data. Since the EIT data has a much lower time cadence than the one from EUVI data, we also study the EIT images containing missing blocks. Fig. 5.6 shows an example of plume identification when the image contains a missing block. In this example, we see that the identification is robust despite the data gaps. However, if no plume peaks in the Hough-space can be identified or if the slope formed by plume peaks is too far from the expected line (5.3), we discard the image.

The Hough-space for the whole time series can be concisely represented by the Sinogram (4.1), i.e.,

$$\mathrm{I}(\rho; t) = \int_{-35^\circ}^{35^\circ} \mathrm{H}(\rho, \theta; t)\, \mathrm{W}(\rho, \theta)\, d\theta \,,$$

where $\mathrm{H}(\rho, \theta; t)$ is the Hough-space intensity and $\mathrm{W}(\rho, \theta)$ the weight function. A similar sinogram to study plumes was proposed for the first time by Llebaria et al. (1998) using the basic Hough coefficients as input, while here we use the weighted Hough-space. We choose weight function that is Gaussian, which gives more weight along the plume peaks given by (5.3),

$$\mathrm{W}(\rho, \theta) = \exp\left(\frac{-\ (\theta + \rho\ u)^2}{2\sigma^2}\right) . \tag{5.4}$$

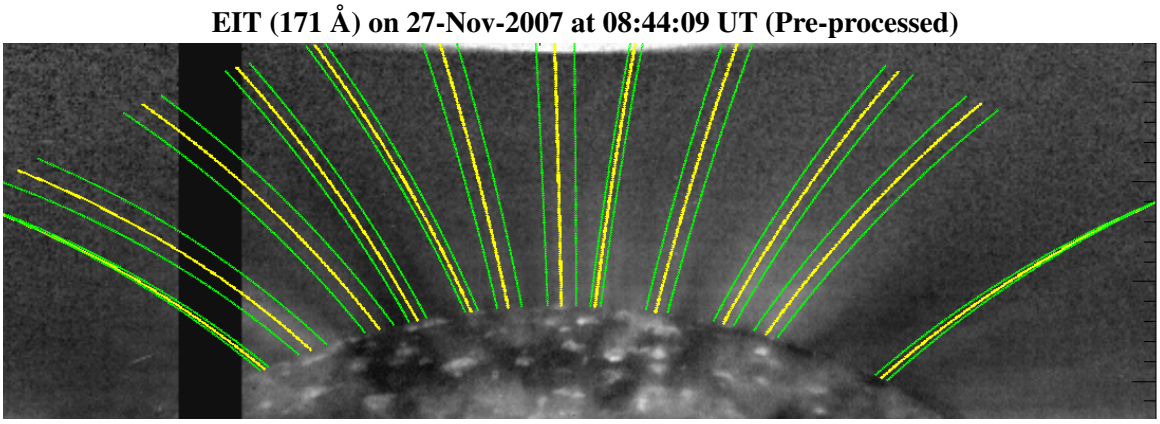

Figure 5.6: The backward transformation of polar plumes on the coronal image with missing blocks (in black).

Fig. 5.7 shows the resulting sinogram obtained from EUVI-B, EIT and EUVI-A. The black lines correspond to the missing data and to the inconsistent data in the case of EIT. Note that EIT has a lower time cadence.
Each row of the sinogram corresponds to a specific view directions at a specific time. In the EUVI-B sinogram, Fig. 5.7, the blue curve correponds to the view direction of the STEREO-B on the 1st of November 2007. After a rotation of 18.8°, which is the separation angle between STEREO-B and EIT, the blue curve is distorted in the EIT sinogram becouse of the solar differential rotation. And after a rotation of 38.6° (i.e. separation angle between STEREO-B and STEREO-A), the blue curve is more distorted since the angle is larger. If the corona would be stationary, we would see exactly the same intensity along each of the blue curves in Fig. 5.7 (EUVI-B), (EIT) and (EUVI-A). The green and red curves are the corresponding view direction for EIT and STEREO-A respectively on the 1st and the 18th of November 2007.
Each sinusoid in Fig. 5.7 corresponds to the intensity of plumes. In Chapter 6, we analyze whether the intensity along a single sinusoid represents the same plume.

In February 2011, STEREO A and B had a separation angle of 180° and therefore saw the same corona (outside the disk). We can therefore test how much of the difference in Fig. 5.7 is due to different data quality. We compute the sinogram for 17.1 days taken from the first of February 2011, Fig. 5.8. We can see that the results are nearly identical.

We evaluate the slope u and the intercept v of (5.3), for north pole and south pole of each image. Fig. 5.9 shows the result for ρ-intercept. In blue we have the results for EUVI-B, in green for EIT and in red for EUVI-A. The shift between the three different instruments is due to the different view directions. The regular variation of the ρ-intercept follows the periodicity of the rotation of the Sun which is about 34 days for a full rotation at the pole. The variation can be explained if the magnetic field dipole is not aligned with the rotation axis and the angle varies with time. Comparing the results for the north and the south pole, we see that the dipole axis is not straight and does not show a perfect opposite phase. The average value of ρ-intercept is

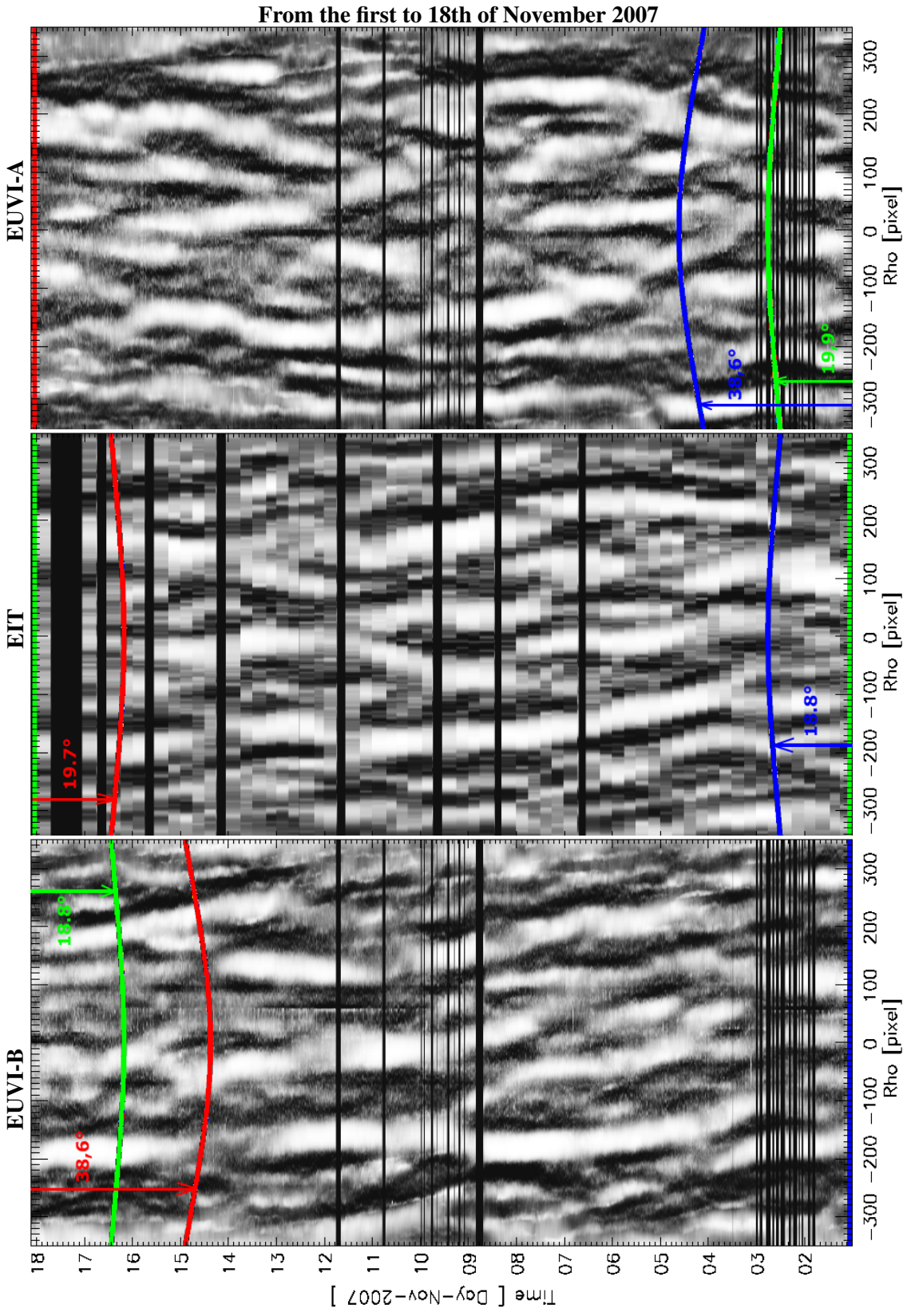

Figure 5.7: Sinogram, from the 1st to 18th of November 2007. The black lines are the missing data. The blue, green and red curves correspond to the view directions of STEREO-B, SOHO and STEREO-A respectively observed at a spcific time (see text).

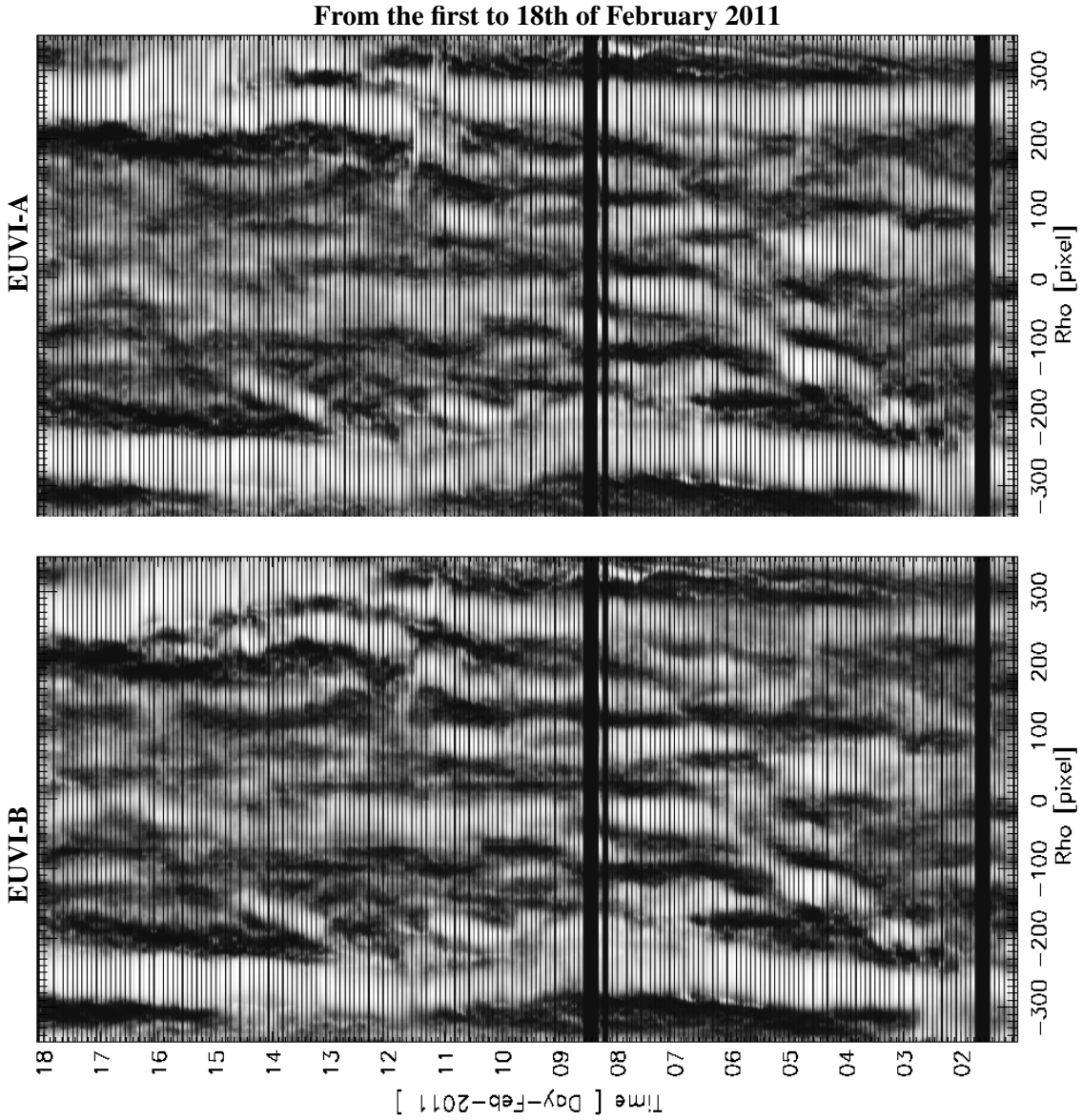

Figure 5.8: Sinogram of 18 days taken from the first of February 2011. The black lines are the missing data.

$< -u/v >= -0.23 \pm 4.83$ pixels for the north pole and $< -u/v >= -0.12 \pm 69.00$ pixels for the south pole. With (5.2), the ρ-intercept corresponds to a latitude varying between 84° and 90° with an average angle $< \phi >$ of $-0.02° \pm 0.48°$ and $-0.01° \pm 6.90°$ for the north and the south, respectively.

The results found for the slope are shown in Fig. 5.10. The average slope is $< u >= -0.15° \pm 0.001°$/pixel and $< u >= 0.12° \pm 0.014°$/pixel for the north and the south, respectively. The slope gives the estimation of the plume inclination. Fig. 5.10 shows also a faster variation, compared

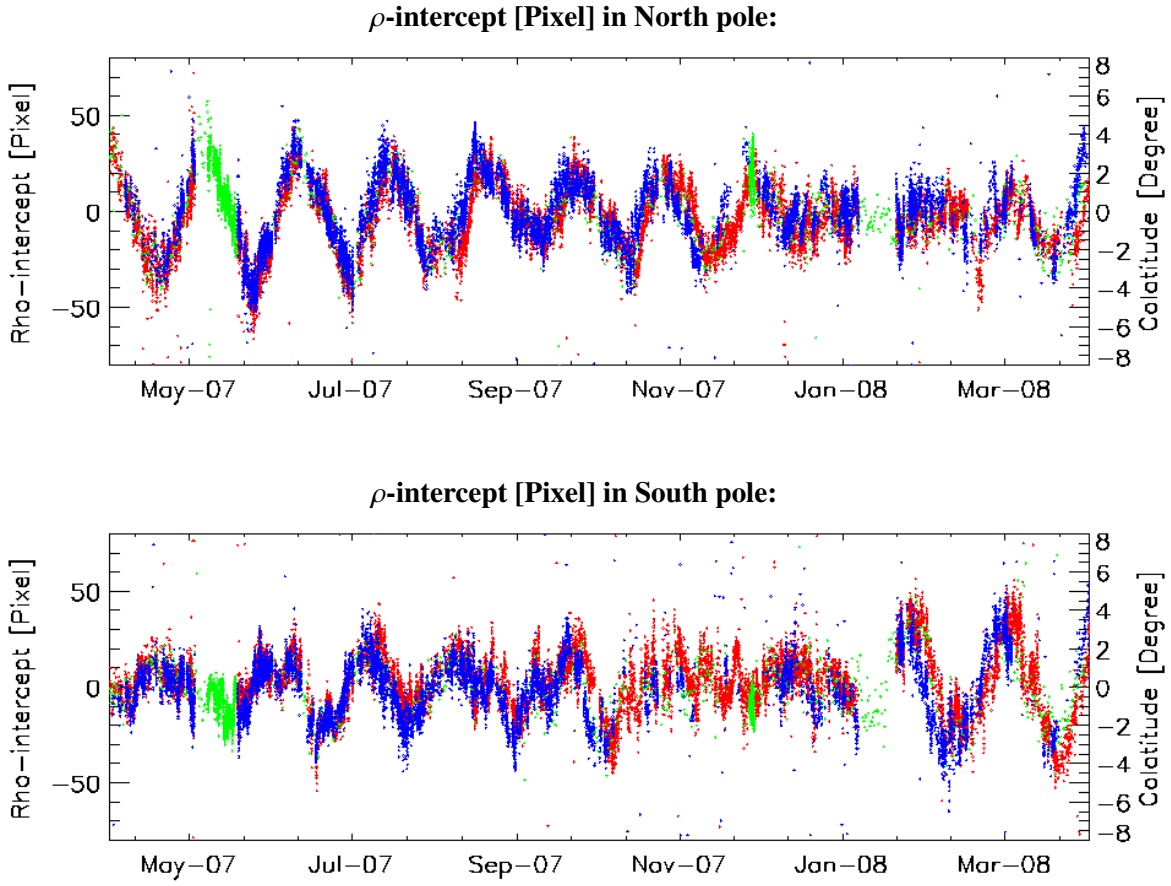

Figure 5.9: ρ-intercept, $-v/u$, evaluated for each image for the North pole (top) and the South (bottom). EUVI-B results are in blue, EIT results are in green and EUVI-A results are in red.

to the ρ-intercept, which can be related to the "breathing" of the open polar flux. This variation is most likely due to the global evolution of the solar magnetic field and the southward or northward shift of the Heliospheric current sheet (Virtanen and Mursula, 2010; Erdős and Balogh, 2010). To compare this with the first order of a dipole, we can study the relation between latitude β and inclination angle ι. For a dipole, we have (Jackson, 1975),

$$\tan(\beta) = \frac{1}{2}\,\tan(\iota), \tag{5.5}$$

and, in our coordinate system, the relation between the latitude β and the inclination at height $r = r_c$ is,

$$\beta_{r_c} = 90^\circ - \left|\frac{\Delta\phi}{\cos\theta}\frac{\theta - v}{u}\right| . \tag{5.6}$$

where we have inserted (5.3) in (5.2). We consider a symmetric pole and take $v = 0$. Fig. 5.11

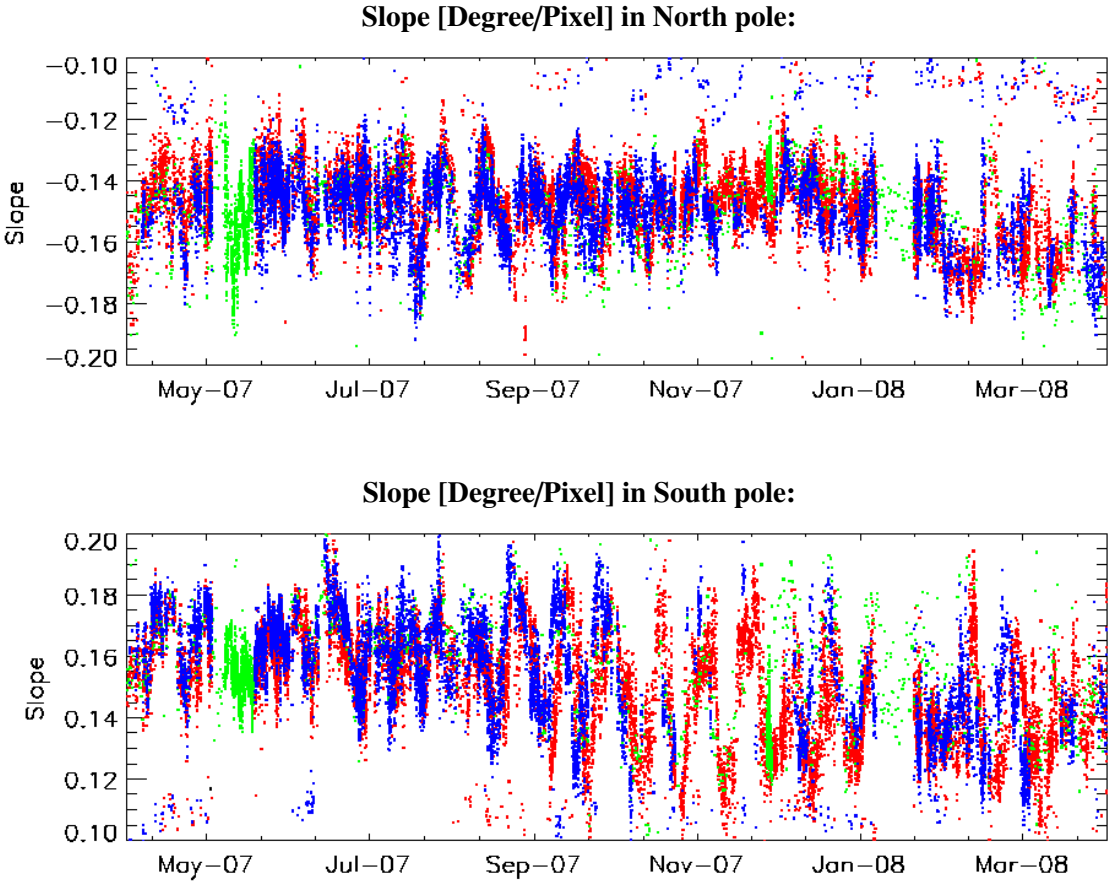

Figure 5.10: Slope, u, evaluated for each image for the North pole (top) and the South (bottom). EUVI-B results are in blue, EIT results are in green and EUVI-A results are in red.

plots the inclination angle versus the latitude for a dipole (in black) and for the observations in blue and red for the north and the south, respectively. For this plot we have taken the average values of the slope $< u >$ for the north and for the south pole. As we can see, the plume orientation is more horizontal than a dipole magnetic field which is in agreement with Feng et al. (2009).

5.4 Summary and Conclusion

In this chapter we have shown that the Hough-wavelet transform is an appropriate method to identify the 2D plumes in solar EUV images. We have identified the northern and southern plumes from May 2007 to April 2008, close to the limb from 1.01 to 1.39 $R_{\odot}$.

In order to study the temporal evolution of plume intensity, we built a sinogram which is a plume

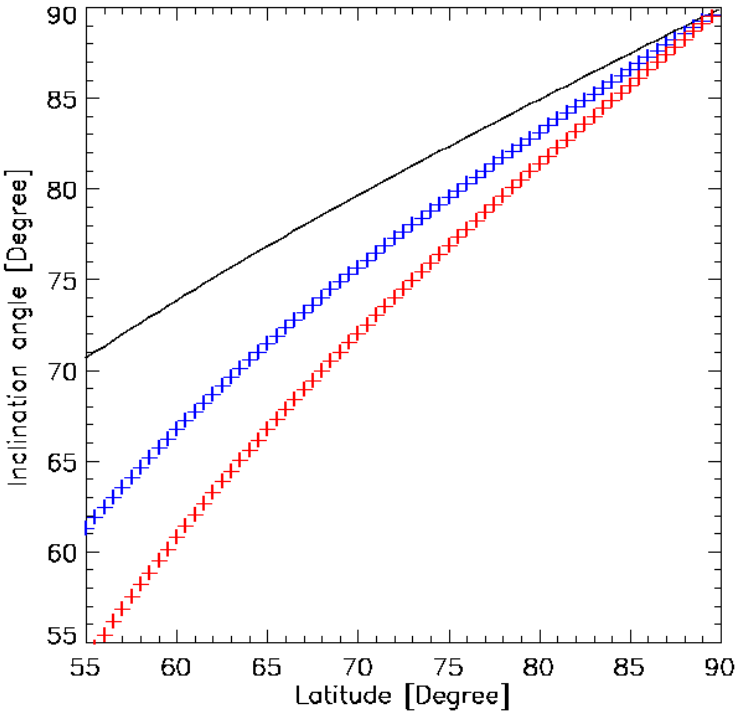

Figure 5.11: Inclination angle versus latitude. The black curve is dipole field. The red and blue curves are the results found for south and north pole, respectively.

time-intensity diagram. These sinograms, established from a single instrument over the time range of the Sun's half rotation, will be used for tomography in Chapter 6. We will also use them as input for stereoscopy, when taken from two differently located instruments at a given time.

We have measured the projected inclination for the plumes and their width in the plane of the sky. The mean inclination of plumes was found to be more horizontal than for a dipole magnetic field which is in agreement with Feng et al. (2009).

The study also revealed a deviation of the open polar cap magnetic field from the solar rotation axis by up to 6°. This deviation in the north and the south pole was found not synchronous and varying with time. The north/south asymmetry over the year is likely due to the global evolution of the solar magnetic field.

Chapter 6
Plume 3D Reconstruction

In this Chapter, we determine the 3D localization and structure of polar plumes. The two methods presented in Chapter 4, are applied to the sinogram data. The tomography method, which uses the filtered backprojection and includes the differential rotation of the Sun, is applied in Section 6.1. Secondly, the conventional stereoscopic triangulation is applied in Section 6.2. In Section 6.3, we show that tomography and stereoscopy are complementary to study polar plumes. Then, in Section 6.4, we discuss a series of identified plumes with regard to their positions, cross section area and temporal evolution. Finally, we study the plume relation with other phenomena in the solar corona such as jets and coronal holes in Section 6.5.

6.1 Tomography

For a series of pre-processed images $\tilde{I}(\mathbf{x}; t)$ (5.1) at a given time t, we consider the sinogram (4.1) for $\theta_1 = -35^\circ$ and $\theta_2 = 35^\circ$. We compute the filtered backprojection (4.15), i.e.,

$$\tilde{\mathrm{D}}(\mathbf{x}) = \int_{0\text{ days}}^{17.09\text{ days}} \int_{-350\text{ pixels}}^{350\text{ pixels}} \delta\left(x\cos[\omega(\beta)\,t] + y\sin[\omega(\beta)\,t] - \rho\right) \int_{-\infty}^{\infty} \mathrm{F}(\rho-\rho')\mathrm{I}(\rho';t)\,d\rho'\,d\rho\,dt,$$

where $\beta = \arccos\left(\frac{\sqrt{(x^2+y^2)}}{R_\odot}\right)$ is the latitude and $\omega(\beta)$ is the differential rotation rate given by (4.13). Fig. 6.1 shows the backprojection $\tilde{\mathrm{D}}(\mathbf{x})$ results. They are calculated independently for each spacecraft for the north pole of the images taken from the 1st up to the 17th of November 2007. The three images in Fig. 6.1 are rotated to the Heliocentric Earth Equatorial (HEEQ) coordinate system with Earth and SoHO located towards the bottom of the image. STEREO-A and B were respectively located at an angle of about 20° to the right and to the left from downwards (see Table 5.1). The separation between plumes with high intensity (yellow to white color on the image) and dark inter-plume regions (blue to black color) are clearly defined. However, the three images do not give an identical result. One reason is the different sensitivity and signal-to-noise ratio of each of the three instruments as we already observed in the sinogram result, Section 5.3. The other more important reason is coming from the fact that the plume intensity

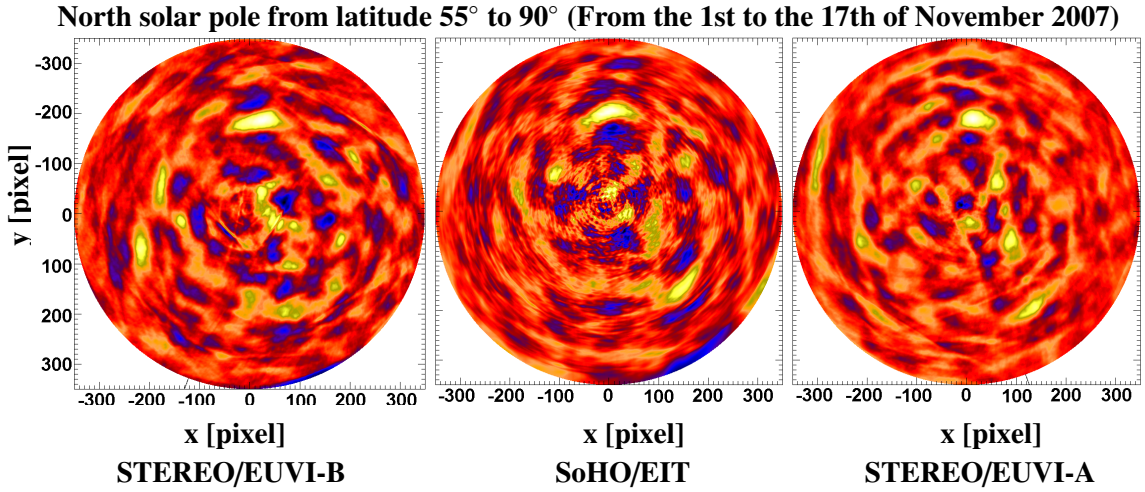

Figure 6.1: Filtered backprojections of the EUVI-B in (a), EIT in (b) and EUVI-A (c) sinograms, from north pole up to latitude 55^o North. North pole is at the center of each image. In the direction straight downwards is the SoHO spacecraft. In the direction downwards left is the STEREO-B spacecraft at about $-20°$ longitude, and STEREO-A is downwards right at about $+20°$ longitude.

varies considerably in time. Indeed, the time for the Sun to rotate 20° – from one spacecraft view direction to the next spacecraft view direction, in November 2007 – corresponds to two days based on the rotation of the pole, and 1.5 days at 55° latitude. Hence, the data seen by each spacecraft differs considerably. In order to test how much of the difference in Fig. 6.1 is due to different data quality, we applied the same analysis to STEREO data from February 2011. At this time the telescopes EUVI-A and B had a separation angle of about 180° (see Table 5.1) and should practically see the same corona. The backprojection results for this period are showed in Fig. 6.2. For both data sets, one can see that our procedure shows nearly identical results. The long curvy strip in the STEREO-A image, Fig. 6.2, is due to an artifact in an image from the 11th of February 2011.

The tomographic results suggest that not all plumes have a near-circular cross section while DeForest et al. (1997) proposed that they are all near-circular. Some plumes indeed look like they have a curtain-like shape, as suggested by Wang and Sheeley (1995); Gabriel et al. (2003). The distinction between the two populations, beam plumes and curtain plumes, is not obvious, because it seems that plumes in between these populations exist.

6.2 Stereoscopy

Ideally, the 3D plume axis is given by the intersection of three planes $\pi_A \cap \pi_B \cap \pi_E$, each of which is readily constructed, as shown in Fig. 6.3. The planes π_i for a detected plume in the images $i = A$, B and E are calculated with the Hough-wavelet parameters (ρ, a, θ), as in Section 6.2,

$$\pi_i(s,t) = P_i + s\ (\mathbf{e}_i + t\ (\mathbf{h}_i x_1 + \mathbf{v}_i y_1)\ \alpha\ \beta + (1-t)(\mathbf{h}_i x_2 + \mathbf{v}_i y_2)\ \alpha\ \beta)\ , \tag{6.1}$$

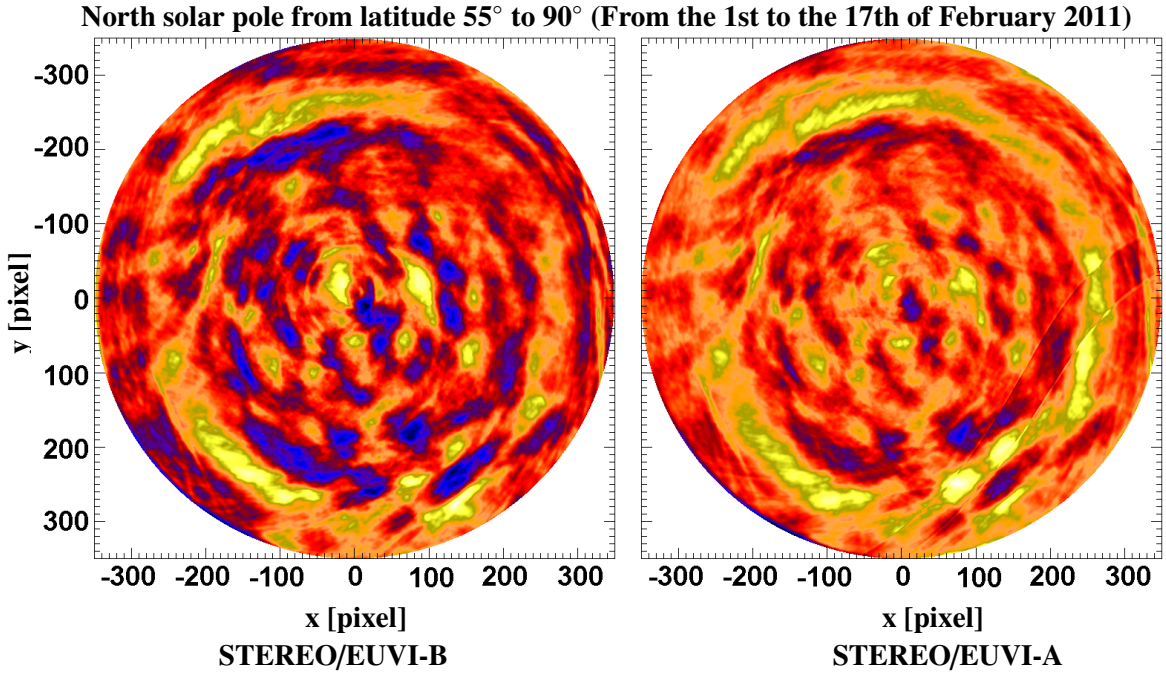

Figure 6.2: Filtered backprojections of the EUVI-B and EUVI-A sinograms for the 1st to the 17th of February 2011 . The north pole is at the center of each image. In the direction straight downwards is the SoHO spacecraft. STEREO-B spacecraft is located to the left at about $-180°$ longitude, and STEREO-A is located to the right at about $+180°$ longitude.

where α is the image conversion factor from pixels to arcsecs and Λ is the radian of an arcsecond. Here, s and P_i are in HEEQ coordinates with P_i as the position of the instrument ($i = A, B$ and E), $\mathbf{v}_i$ and $\mathbf{h}_i$ are the 3D unit vector directions along the edges of the image and $\mathbf{e}_i$ is the image view direction perpendicular to $\mathbf{v}_i$ and $\mathbf{h}_i$. The two arbitrary but different points (x_1, y_1) and (x_2, y_2) are calculated from the Hough-space coordinates of the plume, $(\rho, \theta)_i$. For each plume detected in the image, we calculate the pairwise intersections $\pi_A \cap \pi_B$, $\pi_E \cap \pi_B$ and $\pi_A \cap \pi_E$, which yields three 3D plume axes. For a given plume these three axes should all be identical in the ideal case (Fig. 6.3). The intersection of the axes with the solar surface then yields the footpoint position of the plume on the solar surface.

For each identified plume in the image, we have the measure of the apparent width $4a_{\mathrm{M}}/\sqrt{2}$ from the Hough-wavelet analysis. Given these widths on either side of the planes π_i, the intersection of a pair of planes gives the intersection region with the parallelepiped shape. For the three pairs from the three instruments A, B and E, the intersection area shrinks to a polygon, or is empty if the correspondence of the plumes in the three images was not correctly selected. An example of a plume detected in EUVI-A, B and EIT images is shown in Fig. 6.4. The colored lines (red, blue and green) represent the view directions of STEREO-A, B and EIT respectively. The distance between these pairs of lines corresponds to the respective width $4a_{\mathrm{M}}/\sqrt{2}$ and therefore to the respective apparent width of the plume. The intersection of the strips indicates the area where the plume resides.

The correspondence problem is very difficult to solve for plumes if the angle between the observ-

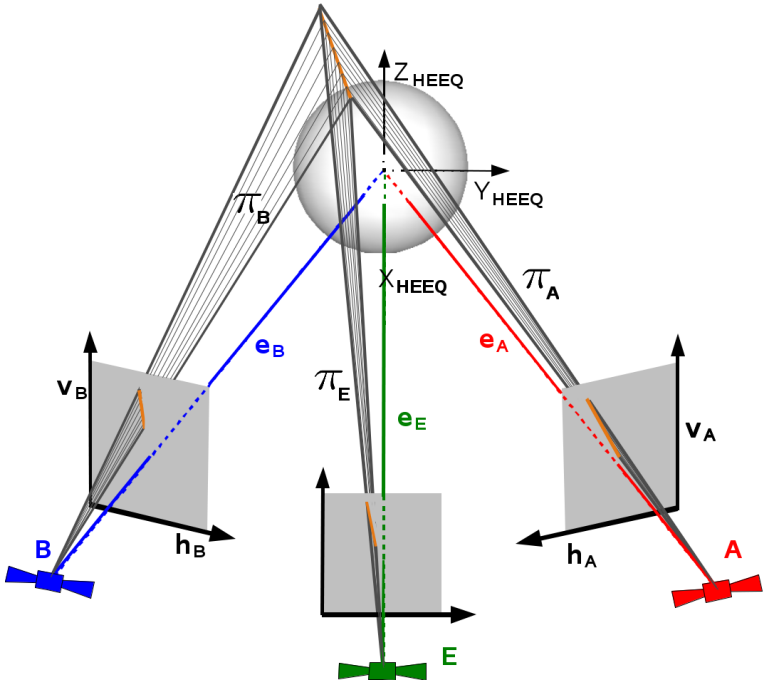

Figure 6.3: HEEQ coordinates with the Sun and the satellites STEREO-A, SOHO-E and STEREO-B. A plume located on the Sun is found at the intersection of the three planes $\pi_A \cap \pi_E \cap \pi_B$ and the solar surface.

ing spacecraft is larger than a few degrees. Since they are faint and diffuse, they become almost indistinguishable. For N_i plumes identified in the image i and N_j plumes identified in the image j with $i, j = A, B$ or E and $j \neq i$, we have in principle $N_i N_j$ stereoscopic solutions. However, most of these solutions are ghosts. To estimate if the stereoscopic solution is a physical solution, we quantify the quality of the correspondence between a plume combination p_i and p_j by the expression $C(p_i, p_j) = c_0 + c_1 + c_2 + c_3$. We define $C(p_i, p_j)$ in order that the smaller $C(p_i, p_j)$, the more probable is the selected correspondence correct:

- The first coefficient c_0 indicates whether the 3D plume axis $\mathbf{p}_{3D}$ has an intersection with the solar surface S. If there is no intersection, this solution is excluded. We define c_0 as,

$$c_0 = \begin{cases} 0 & \text{if} \quad \mathbf{p}_{3D} \bigcap S \neq \emptyset \,, \\ +\infty & \text{if} \quad \mathbf{p}_{3D} \bigcap S = \emptyset \,. \end{cases} \tag{6.2}$$

- Polar plumes are located above polar coronal holes. During solar minima, coronal holes are the largest, and they are located at the pole extend to about 55°–60° latitude. Therefore, the absolute value of each plume footpoint latitude $|\beta_{\mathbf{p}_{3D}}|$ should be greater than 55°. The coefficient c_1 quantifies the preferred position,

$$c_1 = \begin{cases} 0 & \text{if} \quad |\beta_{\mathbf{p}_{3D}}| \geq 55^\circ \,, \\ \dfrac{(|\beta_{\mathbf{p}_{3D}}| - 55^\circ)^2}{5^2} & \text{if} \quad |\beta_{\mathbf{p}_{3D}}| < 55^\circ \,. \end{cases} \tag{6.3}$$

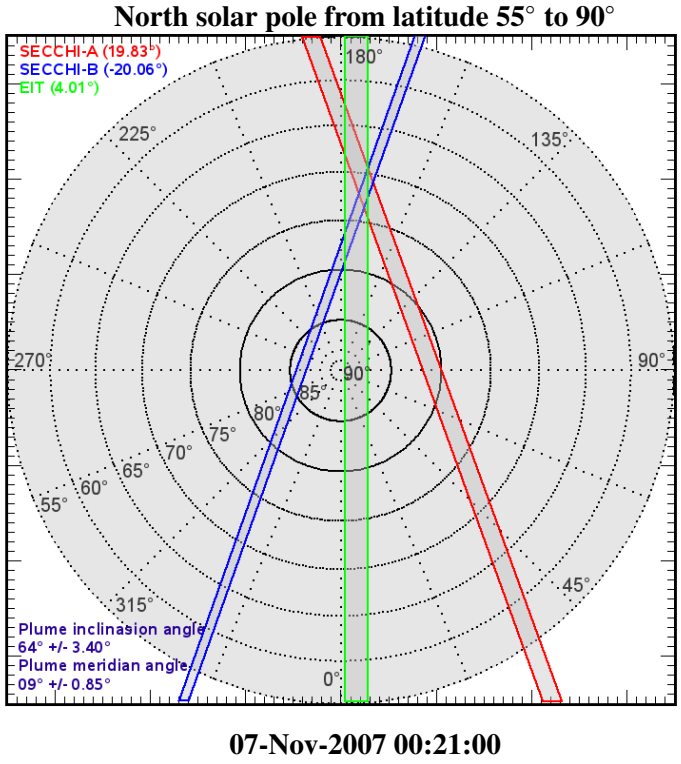

Figure 6.4: View from the top of the Sun in the same coordinates as Fig. 6.1. The intersection of the strips gives the polygon, within which the plume is concentrated.

- Feng et al. (2009) showed that plume 3D axis are less inclined than a dipole magnetic field. For a dipole magnetic field, the relation between the latitude β and the magnetic field inclination angle ι is,

$$\tan(\iota) = 2\tan(\beta)\ . \tag{6.4}$$

  Coefficient c_2 measures the difference between the inclination angle

$$\iota = \arctan(2\tan(\beta_{\mathbf{p}_{3D}}))$$

  of the dipole magnetic field and the inclination angle $\iota_{\mathbf{p}_{3D}}$ of the 3D reconstructed plume axis, and is biased towards smaller inclination angles

$$c_2 = \begin{cases} \dfrac{(\iota - \iota_{\mathbf{p}_{3D}})^2}{5^2} & \text{if} \quad \iota < \iota_{\mathbf{p}_{3D}}\ , \\ \dfrac{(\iota - \iota_{\mathbf{p}_{3D}})^2}{10^2} & \text{if} \quad \iota \geq \iota_{\mathbf{p}_{3D}}\ . \end{cases} \tag{6.5}$$

- The last coefficient c_3 indicates whether the 3D plume axis lies in the meridian plane defined by the solar rotation axis and the plume footpoint position. The meridian angle

$m_{\mathbf{p}_{3D}}$ of the 3D reconstructed plume axis should be close to zero,

$$c_3 = \frac{(m_{\mathbf{p}_{3D}})^2}{5^2} \ . \tag{6.6}$$

A serie of plume candidates is selected by considering the quantity $C(p_i, p_j) < 10$. Table 6.1 shows all possible correspondences found for plumes identified on the 7th of November 2007 at 07:00 for STEREO-A and STEREO-B in (a), STEREO-A and EIT-E in (b), and STEREO-B and EIT-E in (c). The first two columns are the identified plumes p_i numbered from 1 to N_i. The third column corresponds to their apparent width in Mm. The fifth to the eighth columns are the longitude and the latitude of the 3D axis footpoint, the inclination angle ι and the meridian angle m of the 3D axis in degrees, respectively. The second last but one column gives the value of $C(p_i, p_j)$. The polygons, within which the respective plumes have to reside, are shown in Fig. 6.5 (a), where the colors red, blue and green correspond to the Table 6.1 (a) (b) and (c) respectively. Finally, the overlap of these polygones from all three views gives us an effective consistency check of the selected correspondences. The locations where the plumes should be concentrated, are in the intersections of the red, blue and green polygons, shown in yellow in Fig. 6.5 (a). The solutions are numbered in reference to the entry in the last column in Tables 6.1. Fig. 6.5 (b) shows all the plume solutions found with this stereoscopic procedure during a period of one day, from four images observed from 06-Nov-2007 23:36 to 07-Nov-2007 23:38.

6.3 Comparison between Tomography and Stereoscopy

For a number of plumes detected in the EUV images at a given time from the three view directions, the correspondence problem for stereoscopy is hardly solvable. On the other hand, tomography calculation severely suffers from the non-stationarity of the plume structures. Combining both methods, tomography and stereoscopy, can help to identify the plumes and estimate their time variation and cross section shape.

To compare both methods, we repeated stereoscopic procedure with the correspondence coefficient $C(p_i, p_j) < 20$ during half a rotation from the 1st to the 17th of November 2007. Fig. 6.6 (a) shows the result where each stereoscopic solution has been added with taking into account the differential rotation of the Sun. From dark blue to yellow we have the number of occurrences that a plume is identified by the method. Fig. 6.6 (b) show the tomographic result calculated for the same period of time. We can see that plumes, which in Fig. 6.6 (a) occur often, have a counterpart in Fig. 6.6 (b). Therefore, we clearly see that tomography is sensitive to long lived plumes. Short lifetime plumes are reconstructed by stereoscopy, but due to the correspondence problem they are hardly recognizable among all stereoscopic solutions. If the short life plume has a high intensity, it appears in tomography, but distorted. For these plumes, it is necessery to combine stereoscopy and tomography methods to be be identified. Plume n° 1 in Fig. 6.5 is an example of this short lifetime plume and is discussed in the next section.

n° p_A	n° p_B	Width$_A$	Width$_B$	lon	lat	ι	m	$C(p_A, p_B)$	n° $\mathbf{p}_{3D}$
1	5	26.47	17.71	253.01	72.27	53.53	1.14	7.52	6
2	3	25.85	31.99	175.06	75.99	67.02	6.60	2.95	2
2	9	25.85	15.12	285.83	69.43	52.30	1.40	7.36	4
3	8	28.42	17.71	286.88	76.66	57.16	4.14	6.97	7
3	10	28.42	33.27	297.05	66.39	54.58	0.69	5.86	4b
4	6	9.42	24.27	181.63	86.39	83.93	4.60	0.39	
5	5	13.34	17.71	141.30	80.09	67.48	0.39	3.07	8a
5	6	13.34	24.27	155.59	85.86	84.81	2.53	0.16	
6	3	24.27	31.99	125.34	67.49	55.13	2.01	5.66	9
6	6	24.27	24.27	120.80	81.96	72.78	2.46	1.80	8b
7	4	12.26	6.88	114.80	67.79	51.65	6.45	7.80	
8	9	20.73	15.12	41.51	79.13	65.32	2.65	3.76	

(a)

n° p_A	n° p_E	Width$_A$	Width$_E$	lon	lat	ι	m	$C(p_A, p_E)$	n° $\mathbf{p}_{3D}$
1	2	26.47	38.95	255.96	71.82	51.10	5.86	9.09	6
2	2	25.85	38.95	178.40	76.63	61.51	1.59	4.74	2
2	3	25.85	24.27	261.48	77.52	60.57	5.50	5.65	
2	4	25.85	15.12	278.83	73.09	55.49	2.33	6.75	
2	5	25.85	24.27	286.95	68.63	51.36	1.54	7.70	4ab
3	5	28.42	24.27	288.27	75.95	59.73	1.87	5.39	7
3	6	28.42	17.71	296.14	68.38	55.96	0.64	5.32	
4	4	9.42	15.12	161.22	84.27	72.39	7.64	2.76	
5	4	13.34	15.12	143.35	81.61	77.97	1.98	0.65	8a
6	3	24.27	24.27	125.44	68.14	53.54	1.72	6.48	9
6	5	24.27	24.27	120.12	82.39	72.15	2.09	2.01	8b
8	8	20.73	23.98	44.40	79.12	65.12	4.35	3.95	
10	9	38.95	33.27	41.27	70.57	52.32	8.85	8.45	

(b)

n° p_B	n° p_E	Width$_B$	Width$_E$	lon	lat	ι	m	$C(p_B, p_E)$	n° $\mathbf{p}_{3D}$
3	2	31.99	38.95	170.74	75.77	69.69	17.57	4.80	2
3	3	31.99	24.27	123.60	66.85	56.67	0.22	4.92	9
4	4	6.88	15.12	121.95	71.03	66.52	1.71	1.91	
5	2	17.71	38.95	251.91	73.06	58.06	1.12	5.43	6
5	4	17.71	15.12	134.79	78.95	60.55	4.52	5.91	8a
6	3	24.27	24.27	255.34	79.21	68.04	2.14	2.77	
6	5	24.27	24.27	119.28	81.54	73.31	1.76	1.58	8b
7	3	12.92	24.27	271.19	72.56	61.52	0.00	3.82	
7	4	12.92	15.12	272.98	78.43	69.78	0.00	2.07	
8	5	17.71	24.27	288.26	77.34	54.69	2.37	8.41	7
8	8	17.71	23.98	77.88	72.30	69.23	11.14	2.61	
9	5	15.12	24.27	287.38	70.21	53.25	1.59	7.07	4ab

(c)

Table 6.1: All possible correspondences found for plumes identified on 07-Nov-2007 07:00 in (a) STEREO-A and STEREO-B, (b) STEREO-A and EIT-E and (c) STEREO-B and EIT-E. The 3D plume solutions $\mathbf{p}_{3D}$ are shown in yellow within Fig. 6.5 (a).

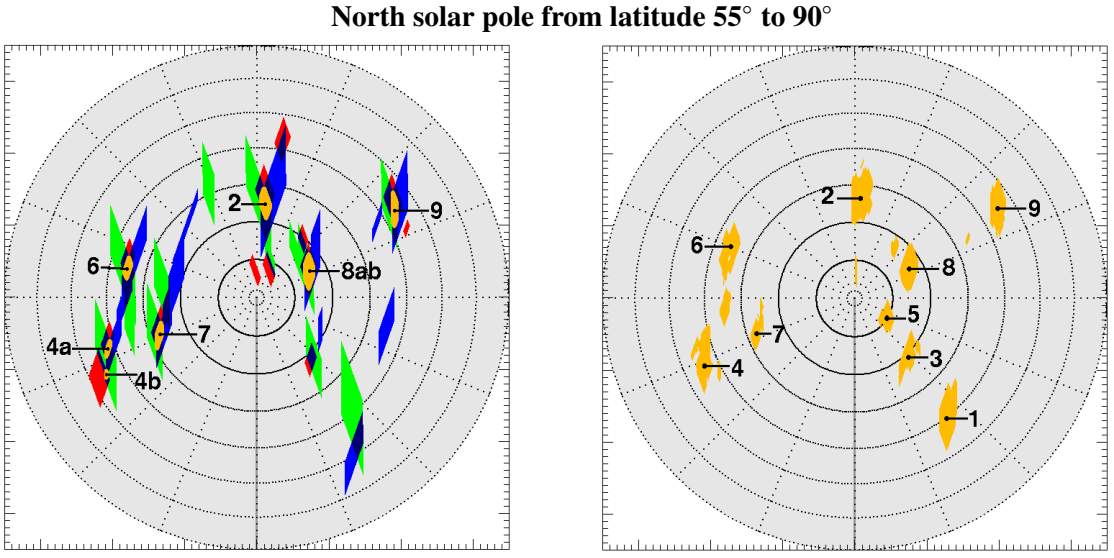

Figure 6.5: Stereoscopic results for a specific time in (a) and for one day in (b). Red polygons are the results for STEREO-A and STEREO-B (see Table 6.1 (a) for the values), blue polygons are the results for STEREO-B and EIT (Table 6.1 (b)) and green polygons are the results for STEREO-A and EIT (Table 6.1 (c)). The locations, within which the plumes are concentrated, are in the intersections of the three results shown in yellow. The blue color represents the overlap of two polygons.

6.4 Plume Lifetime and Cross Section

In general, tomography results give some evidence that plumes can have all types of cross section shapes, from highly located and compact shapes to more elongated shapes. In order to prove whether the shape is the true shape of the plume or if it is an artifact due to its short lifetime, we can check the lifetime of the plume by its trace in the sinogram. Few examples are discussed below, which have been extracted from de Patoul et al. (2011). Each example is numbered in reference to Fig. 6.7:

Plume n° 1

The first case is the plume located at $(x, y) = (110, 200)$ pixels corresponding to (lon,lat) = $(29^\circ, 67^\circ)$. This plume is visible in all the three sinograms (Fig. 6.7 (b)) during the same time period: starting the 3th of November and ending the 8th. It was also identified by stereoscopy during the 7th of November, see Fig. 6.5 (b). In this case, the apparent plume cross section obtained from tomography is elongated due to its short lifetime. Depending on the observing spacecraft, the elongation has a different orientation. The expected theoretical orientation along the average view direction is marked with a dashed line on Fig. 6.7 (a).

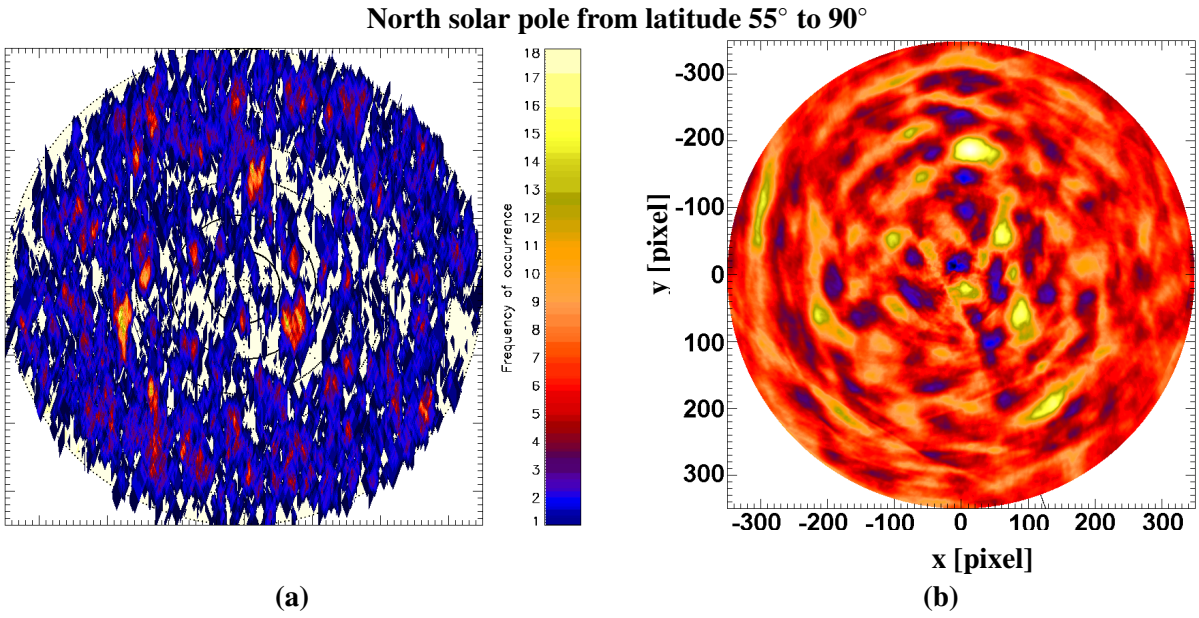

Figure 6.6: (a) Stereoscopic solutions added during half a rotation taking into account the differential rotation of the Sun. (b) Tomographic result for EUVI-A images. Long life plumes are well identified by stereoscopy while plumes with high intensity are better identified by tomography.

Plume n° 2

The second case is the plume located at $(x, y) = (10, -175)$ pixels corresponding to (lon,lat) = $(175°, 74°)$. This plume is visible first in the EUVI-B sinogram at the second of November. It appears about two days later in the sinogram from EIT data and about four days later in the EUVI-A sinogram. In each sinogram it lasts for about eight days. This two and four days delay corresponds exactly to the time for the corona to rotate from the STEREO-B view direction to SoHO ($\sim 20°$) to the STEREO-A view direction ($\sim 40°$) at about 73° latitude. In this case, we expect the true plume cross section be strongly elongated so that the plume becomes most visible when the major axis is aligned with the line-of-sight. The tomography result in Fig. 6.7 (a) shows this elongated cross section with the same orientation for all three instruments. This plume has also a lifetime long enough to be well identified by stereoscopy, see Fig. 6.5 (b) and Fig. 6.6 (b).

Plume n° 3

The third case is the plume located at $(x, y) = (95, 110)$ pixels corresponding to (lon,lat) = $(47°, 74°)$. In the sinogram, we can see that the intensity of this plume varies with time. It can be interpreted as a series of plumes appearing at approximately the same location. From the stereoscopy solution, Fig. 6.5 (b) and Fig. 6.6 (b), we can see two slightly different footpoints, which suggests two different plumes located close to each other and recurring within a short amount of time.

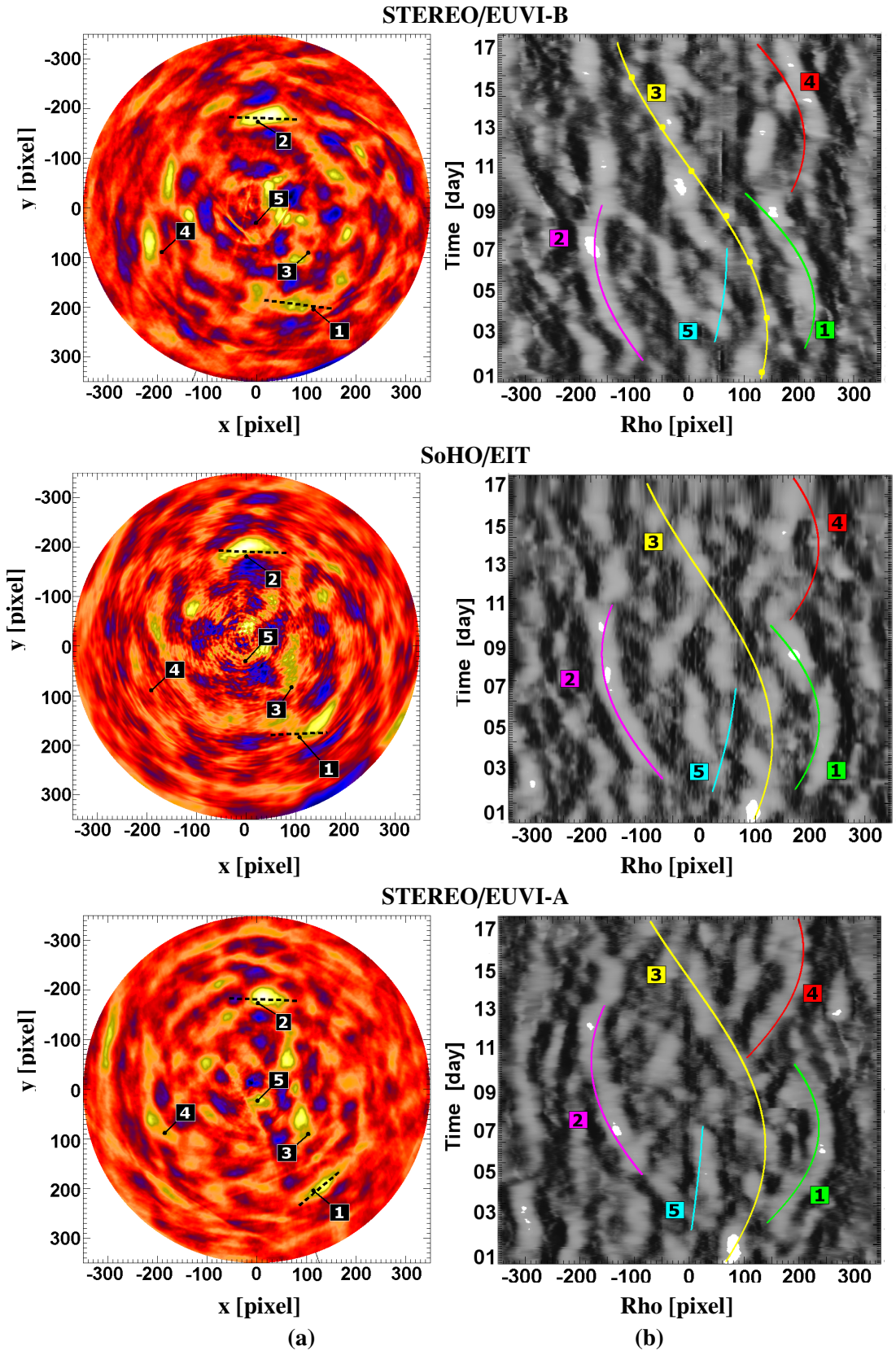

Figure 6.7: (a) Same results as presented in Fig. 6.1 from the 1th of November to the 18th of December 2007. (b) The corresponding sinograms used for the filtered backprojection results. The corresponding selected plumes are shown in colored line with their associated number.

Plume n° 4

Another case is the plume located at $(x, y) = (-190, 90)$ pixels corresponding to (lon,lat) = $(288^\circ, 70^\circ)$. In this case the plume is detected at the same time in all three sinograms, about the 10th of November. It is similar to case n° 1. The plume lasts for about 8 days and for some reason it is not well visible in the EIT instrument. In the tomography reconstruction, the plume cross section appears elongated, but the orientation of the elongation is characteristically rotated for STEREO-A and B due to the short lifetime.

Plume n° 5

The last case is the plume located at $(x, y) = (0, 30)$ pixels corresponding to (lon,lat) = $(0^\circ, 87^\circ)$ (n° 5. in Fig. 6.7). In the sinogram of EUVI-B and EIT, we can see that it consists of successive bursts. During the first burst on the 4th of November at 02:25 UT, a jet was observed, which has been analyzed by Kamio et al. (2010), see Section 6.5. The lifetime of this plume was about 5 days.

6.5 Plumes and other Phenomena

Once we have estimated the location, orientation and lifetime of individual plumes, we can study its relation with other phenomena in the solar corona. In this section, we discuss one case of plume-jet relation and we compare the footpoint positions to the location of the polar coronal holes.

Plume – Jet

Two successive jets were observed on the 4th of November 2007 at 02:00 and 02:30 UT at (lon,lat)= $(75^\circ, 85^\circ)$, which is the same location as plume n° 5. Kamio et al. (2010) studied the second of these jets. Fig. 6.8 shows this jet recorded at 304 Å (in He II) in EUVI-A images. Fig. 6.9 shows the stereoscopic 3D reconstruction of the jet axis. Note that in Fig. 6.9 the HEEQ coordinates are those of the 4th of November 2007 while in this chapter we used the HEEQ coordinates of the 1st of November 2007, which explains the 30° longitude difference between the Fig. 6.9 and the location of the plume n° 5.

Raouafi et al. (2008) suggested coronal jets as precursors of plumes. In this case the plume is visible already before the occurrence of the two jets. These jets cannot be considered as precursors but might be responsable of an enhancement of the plume. To observe a possible change in the plume brightening due to the jet, we compare its profiles in 304 Å and in 171 Å images. To do this, we re-project the plume 3D axes back to EUVI-A and B images for the series of images taken two hours before and five hours after the jets. For each image, a box containing the projected plume axes is built with the apparent width of the plume. Then, we integrate the intensity in the box over the width. Fig. 6.10 shows the resulting profiles to 304 Å (top) and for 171 Å (bottom). The jets can be clearly identified in profiles obtained from 304 Å images while

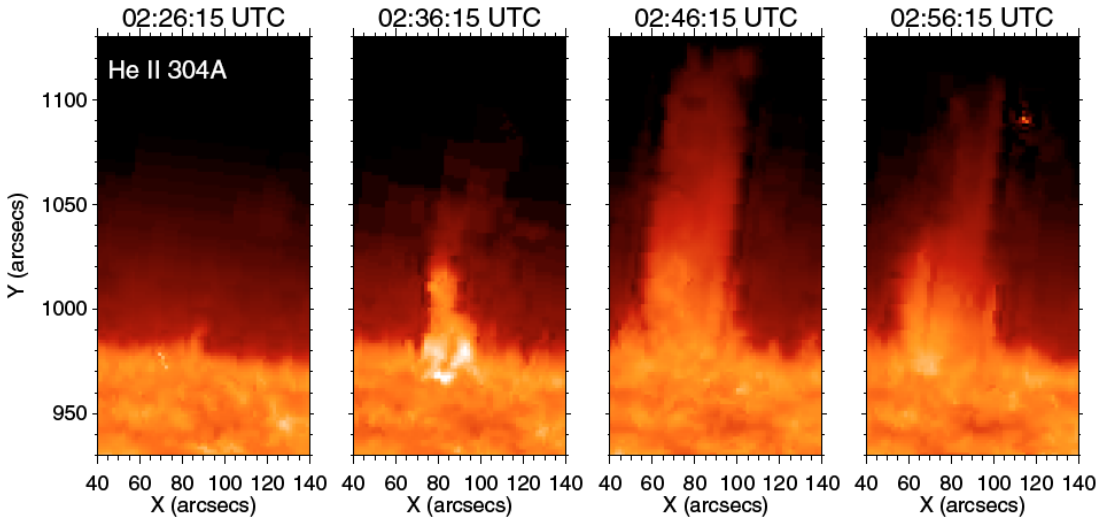

Figure 6.8: Sequence of He II 304 Å images (STEREO-A) showing a jet. (Kamio et al., 2010)

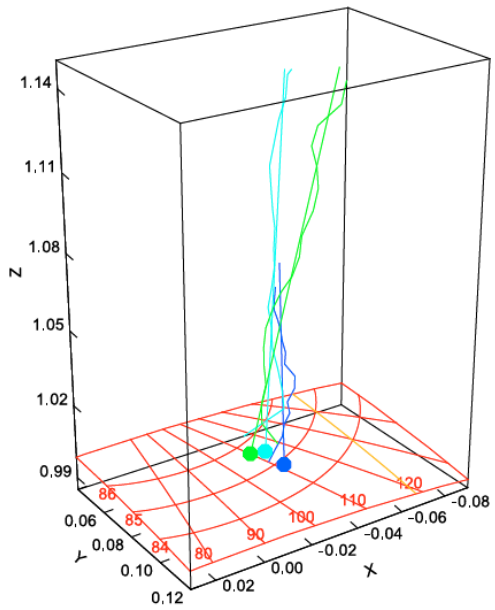

Figure 6.9: The reconstructed Jet from STEREO-A and B images. The centroid curve, fitted principal line, and footpoints are colour coded for the three times of observation: 02:36 UTC (dark blue), 02:46 UTC (light blue), 02:56 UTC (green). The Cartesian HEEQ coordinates are given in units of the solar radius along the outer square box. The solar surface is covered with the corresponding spherical grid in red. Earth is in the positive x direction (lower left). The apparent limb from Earth is indicated by the orange curve on the solar surface. (Kamio et al., 2010)

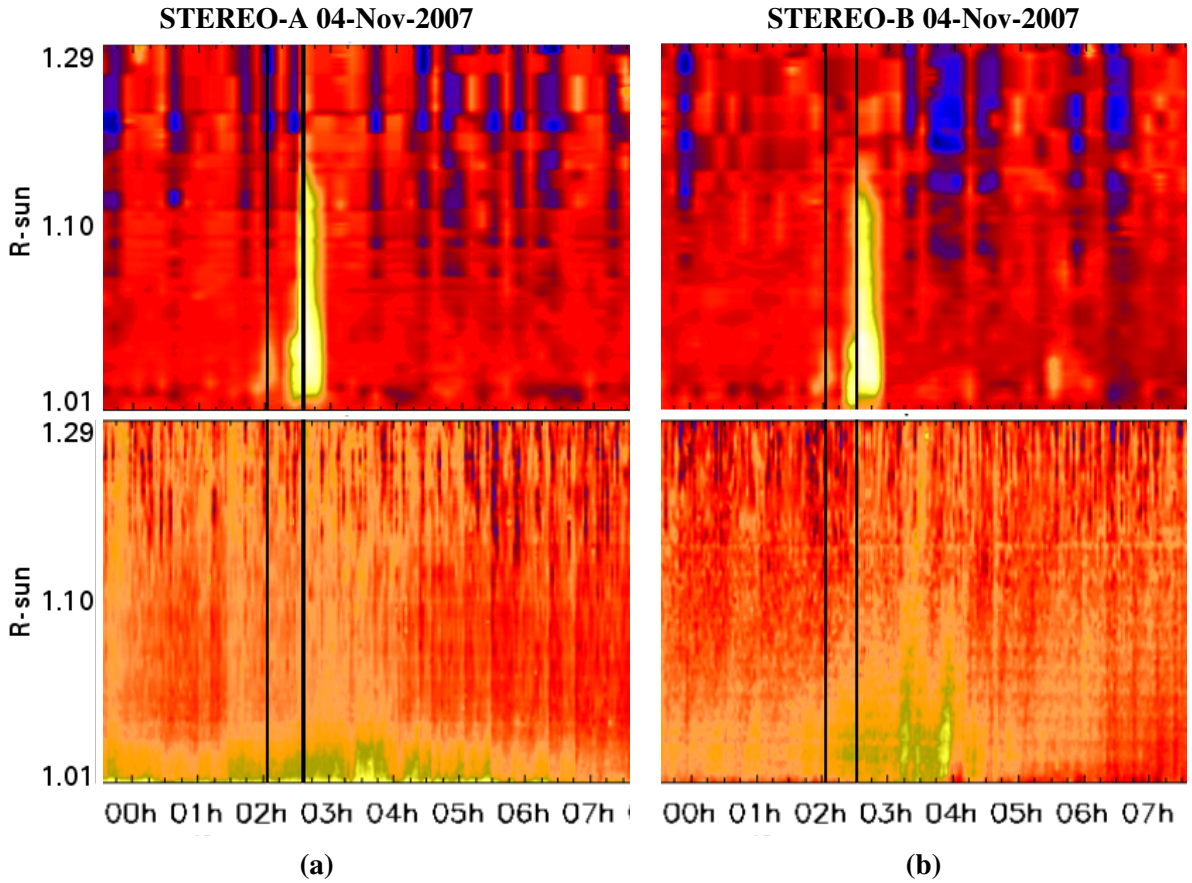

Figure 6.10: Jet and plume profile. Top: Images in He II 304 Å where the jet is well seen. Bottom: Plume profile in 171 Å.

in the 171 Å image where plumes are best seen, we observe only a slight enhancement after the jet event. As suggested by Raouafi et al. (2008), jet probably heats up the coronal plasma inside the plume, which causes the brightness enhancement in the sinogram.

Plume – Coronal hole

We compare the location of plumes relative to the coronal hole area. As a base for the plume distribution over the polar cap we use the tomography results obtained for November 2007. In order to detect the boundaries of the coronal hole, we use EIT and EUVI images at 304 Å where the coronal hole is best seen. For images taken every 20°, we identify the coronal hole boundary by the brighteness contrast. We select a series of points on the boundary and fit a spline curve to them, Fig 6.11 (a). The heliospherical coordinates of the curve are then determined assuming that the curve is lying on the surface of the Sun and taking into account the differential rotation. Fig 6.11 (b) shows the resulting boundary curves identified independently from observation of EUVI-A, EUVI-B and EIT drawn in red, blue and green, respectively. Since coronal holes do not change too fast, we see a good agreement between the three curves. However, at 340°, 0°

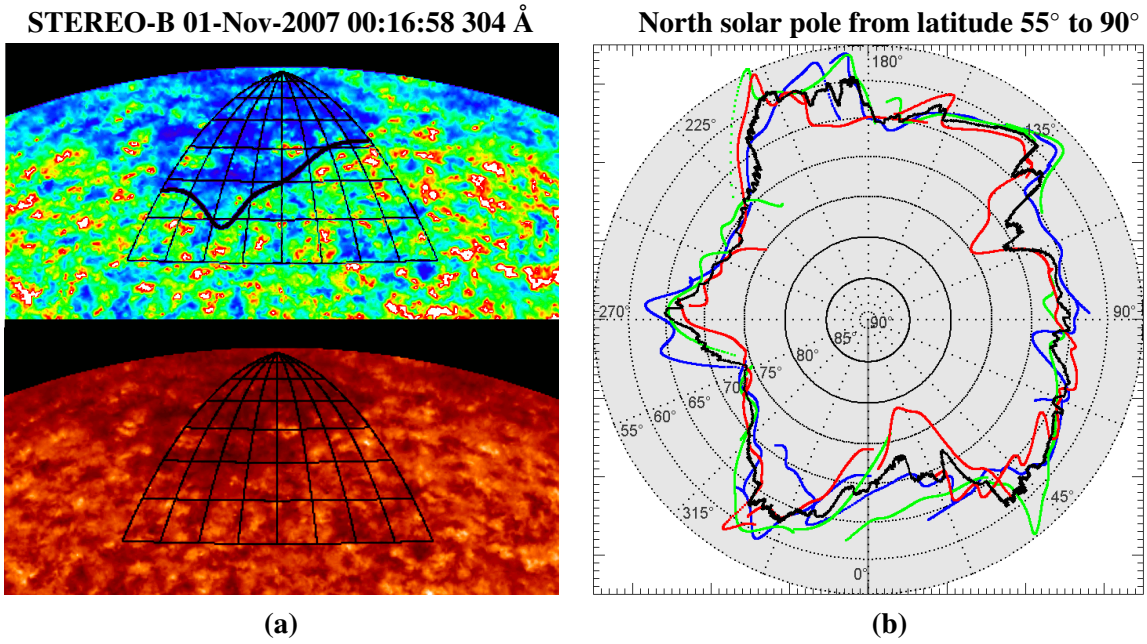

Figure 6.11: (a) Coronal hole seen in STEREO-B images at 304 Å. The top image is in rainbow colortable to emphezise the coronal hole. (b) The resulting curves along the edge of the coronal hole identified for each instruments EUVI-A, EUVI-B and EIT in red, blue and green respectively. The black curve correspond to the mean of these curves.

and 20° the blue, green and red curve respectively, does not close well. At this longitudes the data, from which the hole boundary was determined, jumps by one solar rotation. Over this time difference, the coronal hole boundary has changed by the amount of the discontinuity. The black curve in Fig 6.11 (b) is the mean of these curves. This black curve is then overplotted on the tomography results, Fig 6.12.
We can see that most of the beam plumes are located inside coronal holes. Moreover, as the coronal holes observed on surface of the Sun, expand higher in altitude, the boundary of these coronal holes can also be observed higher in altitude. Some of the elongated plumes close to the coronal hole boundary might be the result of the line of sight integration of this coronal hole boundary.

6.6 Summary and Conclusion

If we disregard the effect of the filter, the tomography reconstruction by plain backprojection at a given longitude and latitude corresponds to the integral along the respective sinogram trace. Hence the inspection of the variation of the sinogram intensity along the respective trace helps to interpret the tomography results.

Plumes with a long lifetime are well detected in tomography results. Moreover, the fact that we

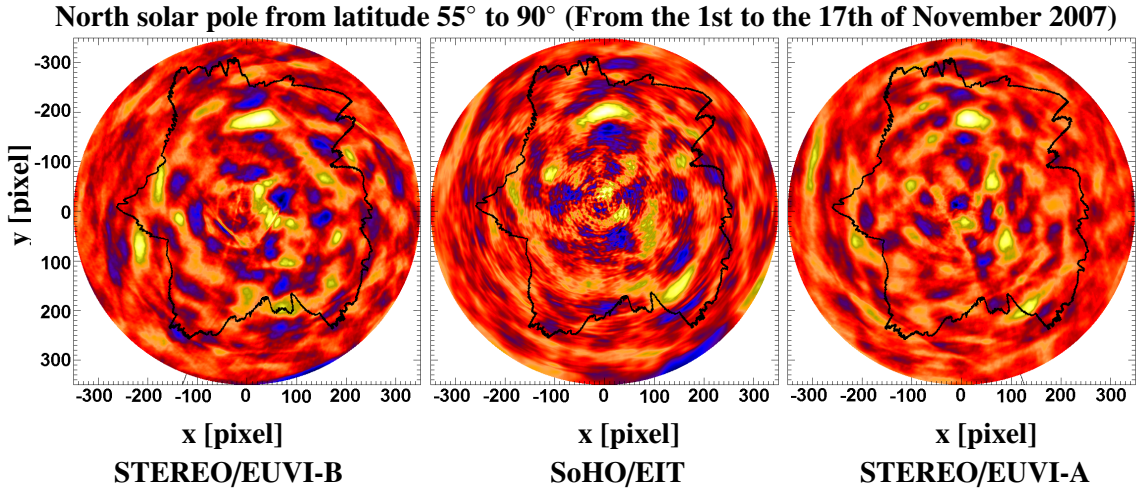

Figure 6.12: Filtered backprojections from Fig. 6.1 with the coronal hole edge marked in black.

can perform this analysis from the data of each spacecraft independently greatly helps to cross check the interpretation. However, the results of the tomography calculation suffer from the non-stationarity of the plume structures. Short lifetimes distort the apparent cross section shape in the reconstruction. On the other hand, stereoscopy reconstructs plumes from EUV images at a given time from two of more view directions. The correspondence problem is hard to solve. However, performing the procedure repeatedly over half a solar rotation allows identifing well the long lived plumes.

In this chapter we have shown that the combination of both methods helps to identify plumes and estimate their time variations and cross sectional shape. So far we have studied few cases. The plumes n° 1 and n° 4 very probably are typical *beam plumes* with a concentrated cross section. We suspect that plume n° 2 has a *curtain* shape with an elongated cross section. This finding confirms the coexistence of *beam plumes* and *curtain plumes* already proposed by Gabriel et al. (2005). However, the tomography result suggests that a broad range of intermediate configurations also exists. The plumes n° 3 and n° 5 were more complex and seem to appear and disappear at the same location with a period of about 2–3 days. A series of jets occurred during the lifetime of plume n° 5, which probably explains the repeated brightness enhancement in the sinogram. The results show that the cross section shape of a plume obtained from a tomography reconstruction can be misinterpreted if the lifetime of the plume is shorted than half a solar rotation.

Finally, we have found that all identified plumes are located inside the coronal holes and some of the elongated plumes close to the coronal hole boundary might be the result of the line of sight integration of this coronal hole boundary.

Part IV

Conclusion & Outlook

Summary and Conclusions

In this thesis we have studied polar plumes in a sequence of Solar EUV images taken nearly simultaneously by SECCHI/EUVI instruments on board the twin STEREO spacecrafts and EIT on board the SOHO spacecraft. Based on the studies of this work, the questions listed in Chapter 2 could be answered to some extent. On the other hand, a number of further considerations have been raised. They are summarized as an outlook following the conclusions.

In part II, we have established a set of new techniques capable of automatically identifying plumes in solar images and of reconstructing their 3-D geometry:

- We have designed a multi-scale method to automatically extract polar plumes in EUV images. We have called this method Hough-wavelet transform. We have tested this method on synthetic images and have shown that it is well adapted to identifying the location, width and orientation of plumes in an image.

- Starting from the Hough-wavelet analysis, we have developed a first 3-D reconstruction method based on tomography by means of the filtered backprojection. We have improved the method by including the differential rotation of the solar surface. By testing the method on a 3-D plume model, we have studied the effects of a short plume lifetime and we have shown the necessity to include differential rotation.

- The second method we have developed is stereoscopy using as input the Hough-wavelet parameters of plumes detected in a pair of images. We have shown the advantage of using the Hough-wavelet transform and we have described the difficulty for solving the correspondence problem in the case of only two view directions.

In part III, we have considered a set of STEREO-A, B and EIT images taken in the EUV wavelength 171Å from May 2007 to April 2008. In order to study plumes, we have established two pre-processing methods: a contrast enhancement and a cosmic ray hits removal procedure. Once the images are pre-processed, we have applied the new techniques on the images and analyzed the temporal evolution of plumes and their 3-D reconstruction:

- For each image taken from May 2007 to April 2008, we have measured the projected inclination of plumes in the southern and northern polar cap. The mean orientation of plumes was found to be more horizontal than for a dipole magnetic field, which is in agreement with Feng et al. (2009). The study revealed an asymmetry of the open polar cap magnetic field from the solar rotation axis by up to 6°. This asymmetry was found in

both, the northern and southern polar cap. We observe also a variation of this north/south asymmetry over the year, which is likely due to the global evolution of the solar magnetic field.

- With the tomographic technique we have identified the plume cross section. The results clearly indicate the presence of both near-circular cross section (DeForest et al., 1997) and curtain-like structures (Wang and Sheeley, 1995; Gabriel et al., 2003). Our tomography reconstruction also shows a network pattern with both types of plume cross sections as already proposed by Barbey et al. (2008) and Gabriel et al. (2009). We have discussed under which circumstances the reconstruction of the cross section shapes were the true cross sections of plumes or whether they were due to a short lifetime of the plume.

- With stereoscopic reconstructions we have reconstructed the 3-D plume axes. The correspondence problem for stereoscopic reconstructions has been improved by considering the three view directions STEREO-A, B and EIT. By combining tomographic and stereoscopic results, we found different lifetime of plumes: plumes having a long livetime up to 9 days, plumes having a short livetime of 2-3 days and series of short lived plumes re-occurring at the same location.

- With the 3-D reconstructions of plumes we have been able to identify the association of a plume with a jet and we could explain the intensity enhancement within the plume. Finally, we have found that all identified plumes are located inside coronal holes. Some of the plumes with elongated cross section close to the coronal hole boundary might be the result of a line of sight integration tangential to the coronal hole boundary.

Outlook

Taking advantage of the new techniques elaborated in this thesis and the information from several view directions, further investigations are required for a deeper understanding of polar plumes.

- The Hough-wavelet method is well adapted for characterizing plumes in a series of images. However, the method does not provide information about the curvature of the plumes. This could be improved by adding a curvature coefficient c for a family of wavelets $\psi_{\rho,a,\theta,c}$. The additional parameter, however, will blow up our Hough-space and complicate the search for intensity maxima representing the plumes. The Hough-wavelet tool package can be also used to identify other solar objects such as polar jets in chromospheric images or coronal mass ejections, which are already detected with the basic Hough transform by Robbrecht and Berghmans (2004).

- Up to now, the tomography procedure has been applied to the data from each of the three spacecrafts independently. For each reconstruction, half a rotation of the Sun, i.e. 17.1 days, is needed. In order to reduce this time, we could combine the data from all spacecraft for the density reconstruction. Depending on the angle between the spacecraft, the total observation time for a complete reconstruction could be markedly reduced. However, for this procedure, the different instruments need to be carefully intercalibrated.

- In this work we have restricted our plume study close to the surface, from 1.01 $R_\odot$ to 1.39 $R_\odot$. We could extend our plume analysis to solar radii of up to 15 $R_\odot$ by using the coronagraph data from SOHO/LASCO and STEREO/COR-1 & 2. For this particular study considering the curvature of the plumes becomes necessary.

- Since the launch of the SDO mission, the instrument SDO/AIA produces multiwavelength images at higher spatial resolution and higher time candance. From multiwavelength observations we can derive electron densities and temperatures (e.g. Walker et al. (1993)).

- The understanding of the origin and evolution of plume intensity variations is still puzzling. A careful look at the plasma dynamics at the footpoints could help to explain plume heating and plasma acceleration. Plumes could be heated by small magnetic reconnection events located at the footpoints (Wang, 1998; Raouafi et al., 2008). With the plume 3-D reconstruction, we can identify the correlation of plumes with other phenomena at their footpoints. So far we have studied few individual reconstructed plumes. For one plume we have established the relation between its intensity variation and a jet observed at the

same location. By studying more individually reconstructed plumes, we could improve our knowledge about the correlation between plumes and jets, or between plumes and bright points, which could be responsible for the heating process.

- There is a qualitative similarity between the tomography results and the solar supergranular network. However, the relation between plumes and the solar network is not fully established. Gabriel et al. (2009) have proposed forward modeling of plumes as field-aligned extensions of the solar network. With the help of tomography techniques further investigations on plume distributions over the solar pole could give some statistical evidence whether a relation between plumes and the network exists.

Appendix A
Image transforms

A.1 Hölder regularity

The strength of a local singularity in a 2D signal can be characterized by the *Hölder exponent* (Mallat, 1998; Torrésani, 1995). For a signal $f(\mathbf{x})$, n times differentiable, the Hölder exponent $h(\mathbf{x}_0)$ at the point $\mathbf{x}_0$ is defined in a rigorous way as the largest exponent possible such as there exists a polynom P_n of degree $n \leq h(\mathbf{x}_0)$ and a constant $K > \mathbb{R}_0^+$,

$$\forall \mathbf{x} \in \mathbb{R}^2 : \quad \|\mathbf{x} - \mathbf{x}_0\| < \epsilon, \quad |f(\mathbf{x}) - P_n(\mathbf{x} - \mathbf{x}_0)| \leq K\|\mathbf{x} - \mathbf{x}_0\|^{h(\mathbf{x}_0)}$$

where $\|\mathbf{x}\| = \sqrt{x^2 + y^2}$. The polynom P_n corresponds to the highest 2D Taylor series of f in the neighborhood of $\mathbf{x}_0$ with respect to the differentiability of the function f at this point. For example, a function

$$f(\mathbf{x}) = \begin{cases} \mathbf{x}^\alpha & \text{if } x \geq 0 \\ 0 & \text{if } x < 0 \end{cases}$$

has an Hölder exponent in $\mathbf{x}_0 = 0$ of α. The smaller $h(\mathbf{x}_0)$, the more singular is the image around $\mathbf{x}_0$.

A.2 Wavelets

In wavelets analysis, a function has to satisfy the *admissibility condition* to be a wavelets :

Definition A.2.1. *A* wavelet *is a function $\psi(\mathbf{x}) \in L^2(\mathbb{R}^2) \cap L^1(\mathbb{R}^2)$ satisfying the admissibility condition:*

$$0 < \quad C_\psi \equiv (2\pi)^2 \int_{\mathbb{R}^2} \frac{\left|\widehat{\psi}(\mathbf{k})\right|^2}{\|\mathbf{k}\|^2} \, d^2\mathbf{k} \quad < \infty, \tag{A.1}$$

where $\|\mathbf{k}\|^2 = \mathbf{k}_x^2 + \mathbf{k}_y^2$ and $\widehat{\psi}$ stands for the Fourier transform of ψ.

This definition means that the Fourier transform of the a wavelet decays sufficiently quickly at infinity. By definition, integral over ψ exists and is required to have zero mean:

$$\widehat{\psi}(0) = 0 \quad \Leftrightarrow \quad \int_{\mathbb{R}^2} \psi(\mathbf{x}) \, d^2\mathbf{x} = 0.$$

An admissible wavelet is a typical function with a wave-like oscillation. A *family of wavelets* is generated by elementary operations, i.e.,

- Translation: $(T^{\mathbf{b}}\,\psi)(\mathbf{x}) = \psi(\mathbf{x}-\mathbf{b}) \quad , \quad \mathbf{b}\in\mathbb{R}^2$ (A.2)
- Dilatation: $(D^a\,\psi)(\mathbf{x}) = \frac{1}{a}\psi\left(\frac{\mathbf{x}}{a}\right) \quad , \quad a\in\mathbb{R}_0^+$ (A.3)
- Rotation: $(R^\theta\psi)(\mathbf{x}) = \psi\left(r_\theta^{-1}(\mathbf{x})\right) \quad , \quad \theta\in[0,2\pi[$ (A.4)

  with r_θ the rotation matrix $r_\theta = \begin{pmatrix} \cos\theta & -\sin\theta \\ \sin\theta & \cos\theta \end{pmatrix}$

These three elementary transformations constitute the similitude group SIM(2) $= (\mathbb{R}^2 \times \mathbb{R}_r^+ \times$ SO(2)) which act on the wavelet function ψ as

$$(T^{\mathbf{b}}D^aR^\theta\,\psi)(\mathbf{x}) = \frac{1}{a}\psi\left(\frac{r_\theta^{-1}(\mathbf{x}-\mathbf{b})}{a}\right).$$

The operators $T^{\mathbf{b}}, D^a, R^\theta$ preserve the admissibility condition, so any function $\psi_{\mathbf{b},a,\theta} = (T^{\mathbf{b}}D^aR^\theta\,\psi)(\mathbf{x})$ obtained from a wavelet ψ is again a wavelet. In Fourier space, the space shift, $T^{\mathbf{b}}$, becomes a phase shift proportional to frequency and to the amount of the shift expressed by the operator $E^{-\mathbf{b}}$. The dilatation, D^a, becomes a contraction by the respective inverse scale factor: $D^{1/a}$. The rotation, R^θ, remains the same. The Fourier transform of the family of wavelets is therefore

$$(E^{-\mathbf{b}}D^{1/a}R^\theta\,\widehat{\psi})(\mathbf{k}) = a\,\widehat{\psi}\left(a\,r_\theta^{-1}(\mathbf{k})\right)\,e^{-i\mathbf{b}\cdot\mathbf{k}}\,.$$

Appendix B
Dipole Magnetic Field

A dipole magnetic field is the lowest order of approximation for the magnetic field of the global quiet Sun. It is generated at large distances by localized current distributions. We consider the circular current loop of radius a centered at the origin lying in the xy plane. The distance from the dipole center is denoted by r, the zenith angle from the dipole axis is ϕ and the azimuth angle is λ, (Fig. B.1). A general derivation of the dipole magnetic field in spherical coordinates is given in Jackson (1975), which in far-field approximation, i.e. $r \gg a$, it takes the analytical form,

$$B_r = \frac{\mu_0 I a^2}{2} \frac{\cos\phi}{r^3}\,, \tag{B.1}$$

$$B_\phi = \frac{\mu_0 I a^2}{4} \frac{\sin\phi}{r^3}\,, \tag{B.2}$$

$$B_\lambda = 0\,, \tag{B.3}$$

where I is the loop current. If we assume the circular current loop lying in the solar equatorial plane, we can derive the relation between the latitude β and the magnetic inclination ι, which is defined as the angle between $\mathbf{B}$ and $\mathbf{e}_\phi$ (Fig. B.1). We divide (B.1) by (B.2), and we obtain

$$\tan\iota = \frac{B_r}{B_\phi} = 2\ \cot\phi = 2\ \tan\beta\,. \tag{B.4}$$

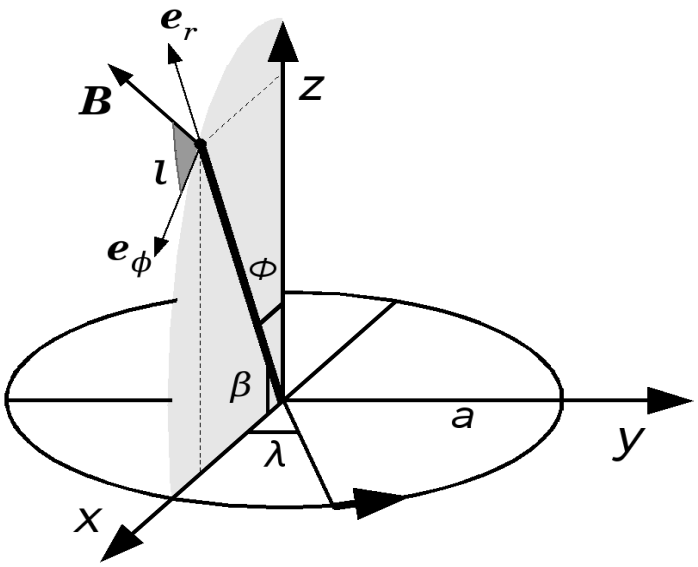

Figure B.1: The circular current system lying on the xy. $\mathbf{B} = (B_r, B_\phi, B_\lambda)$ is the magnetic field, ι is the inclination angle.

Bibliography

Ahmad, I. A., Webb, D. F., 1978, X-ray analysis of a polar plume, *Solar Physics*, 58, 323–336

Ahmad, I. A., Withbroe, G. L., 1977, EUV analysis of polar plumes, *Solar Physics*, 53, 397–408

Altschuler, M. D., Perry, R. M., 1972, On Determining the Electron Density Distribution of the Solar Corona from K-Coronameter Data, *Solar Physics*, 23, 410–428

Antoine, J.-P., Murenzi, R., Vandergheynst, P., 1999, Directional Wavelets Revisited: Cauchy Wavelets and Symmetry Detection in Patterns, *Applied and Computational Harmonic Analysis*, 6, 314–345

Antoine, J.-P., Demanet, L., Hochedez, J.-F., Jacques, L., Terrier, R., Verwichte, E., 2002, Application of the 2-D wavelet transform to astrophysical images, *Physicalia Magazine*, 24, 93–116

Antoine, J.-P., Murenzi, R., Vandergheynst, P., Ali, S., 2004, Two-Dimensional Wavelets and their Relatives, Signal Processing, Cambridge University Press

Aschwanden, M. J., 2004, Physics of the Solar Corona: an Introduction, Praxis Publishing Ltd., Chichester, UK, and Springer Verlag, Berlin

Aschwanden, M. J., 2010, Image Processing Techniques and Feature Recognition in Solar Physics, *Solar Physics*, 262, 235–275

Barbey, N., Auchère, F., Rodet, T., Vial, J.-C., 2008, A Time-Evolving 3D Method Dedicated to the Reconstruction of Solar Plumes and Results Using Extreme Ultraviolet Data, *Solar Physics*, 248, 409–423

Beck, J. G., 2000, A comparison of differential rotation measurements, *Solar Physics*, 191, 47–70

Benz, A., Murdin, P., 2000, Solar Flare Observations, Encyclopedia of Astronomy and Astrophysics

Bray, R. J., Loughhead, R. E., 1974, The solar chromosphere, Chapman and Hall, New York

Candès, E. J., Donoho, D. L., 1999, Ridgelets: a key to higher-dimensional intermittency?, *Philosophical Transactions of the Royal Society of London, A*, 357, 2495–2509

Charbonneau, P., 2010, Dynamo Models of the Solar Cycle, *Living Reviews in Solar Physics*, 7, 3

Cranmer, S. R., 2002, Coronal Holes and the High-Speed Solar Wind, *Space Science Reviews*, 101, 229–294

Cranmer, S. R., 2009, Coronal holes, *Living Reviews in Solar Physics*, 6, 3

Cranmer, S. R., Kohl, J. L., Noci, G., Antonucci, E., Tondello, G., Huber, M. C. E., Strachan, L., Panasyuk, A. V., Gardner, L. D., Romoli, M., Fineschi, S., Dobrzycka, D., Raymond, J. C., Nicolosi, P., Siegmund, O. H. W., Spadaro, D., Benna, C., Ciaravella, A., Giordano, S., Habbal, S. R., Karovska, M., Li, X., Martin, R., Michels, J. G., Modigliani, A., Naletto, G., O'Neal, R. H., Pernechele, C., Poletto, G., Smith, P. L., Suleiman, R. M., 1999, An Empirical Model of a Polar Coronal Hole at Solar Minimum, *Astrophysical Journal*, 511, 481–501

de Patoul, J., Inhester, B., Feng, L., Wiegelmann, T., 2011, 2D and 3D Polar Plume Analysis from the Three Vantage Positions of STEREO/EUVI A, B, and SOHO/EIT, *Solar Physics*, pp. 1–19

Defise, J.-M., 1999, Analyse des performances instrumentales du téléscope spatial EIT, Ph.D. thesis, Université de Liége, Belgium

DeForest, C. E., Gurman, J. B., 1998, Observation of Quasi-periodic Compressive Waves in Solar Polar Plumes, *Astrophysical Journal. Letters to the Editor*, 501, L217–L220

DeForest, C. E., Hoeksema, J. T., Gurman, J. B., Thompson, B. J., Plunkett, S. P., Howard, R., Harrison, R. C., Hassler, D. M., 1997, Polar Plume Anatomy: Results of a Coordinated Observation, *Solar Physics*, 175, 393–410

DeForest, C. E., Lamy, P. L., Llebaria, A., 2001, Solar Polar Plume Lifetime and Coronal Hole Expansion: Determination from Long-Term Observations, *Astrophysical Journal*, 560, 490–498

Del Moro, D., 2004, Solar granulation properties derived from three different time series, *Astronomy and Astrophysics*, 428, 1007–1015

Del Zanna, L., Hood, A. W., Longbottom, A. W., 1997, An MHD model for solar coronal plume, *Astronomy and Astrophysics*, 318, 963–969

Delaboudiniere, J.-P., Artzner, G. E., Brunaud, J., Gabriel, A. H., Hochedez, J. F., Millier, F., Song, X. Y., Au, B., Dere, K. P., Howard, R. A., Kreplin, R., Michels, D. J., Moses, J. D., Defise, J. M., Jamar, C., Rochus, P., Chauvineau, J. P., Marioge, J. P., Catura, R. C., Lemen, J. R., Shing, L., Stern, R. A., Gurman, J. B., Neupert, W. M., Maucherat, A., Clette, F., Cugnon, P., van Dessel, E. L., 1995, EIT: Extreme-Ultraviolet Imaging Telescope for the SOHO Mission, *Solar Physics*, 162, 291–312

Delouille, V., de Patoul, J., Hochedez, J. F., Jacques, L., Antoine, J. P., 2005, Wavelet Spectrum Analysis Of Eit/Soho Images, *Solar Physics*, 228, 301–321

Domingo, V., Fleck, B., Poland, A. I., 1995, The SOHO Mission: an Overview, *Solar Physics*, 162, 1–37

Erdős, G., Balogh, A., 2010, North-south asymmetry of the location of the heliospheric current sheet revisited, *Journal of Geophysical Research*, 115, A01 105

Feng, L., Inhester, B., Solanki, S. K., Wilhelm, K., Wiegelmann, T., Podlipnik, B., Howard, R. A., Plunkett, S. P., Wuelser, J. P., Gan, W. Q., 2009, Stereoscopic Polar Plume Reconstructions from STEREO/SECCHI Images, *Astrophysical Journal*, 700, 292–301

Frazin, R. A., Kamalabadi, F., 2005, Rotational Tomography For 3d Reconstruction Of The White-Light And Euv Corona In The Post-Soho Era, *Solar Physics*, 228, 219–237

Freeland, S. L., Handy, B. N., 1998, Data Analysis with the SolarSoft System, *Solar Physics*, 182, 497–500

Gabriel, A., Bely-Dubau, F., Tison, E., Wilhelm, K., 2009, The Structure and Origin of Solar Plumes: Network Plumes, *Astrophysical Journal*, 700, 551–558

Gabriel, A. H., Bely-Dubau, F., Lemaire, P., 2003, The Contribution of Polar Plumes to the Fast Solar Wind, *Astrophysical Journal*, 589, 623–634

Gabriel, A. H., Abbo, L., Bely-Dubau, F., Llebaria, A., Antonucci, E., 2005, Solar Wind Outflow in Polar Plumes from 1.05 to 2.4 R_{solar}, *Astrophysical Journal. Letters to the Editor*, 635, L185–L188

Gibson, S. E., Low, B. C., 1998, A Time-Dependent Three-Dimensional Magnetohydrodynamic Model of the Coronal Mass Ejection, *Astrophysical Journal*, 493, 460–473

Golub, L., Pasachoff, J., 2009, The Solar Corona, Cambridge University Press, Cambridge

Hall, J. C., 2008, Stellar Chromospheric Activity, *Living Reviews in Solar Physics*, 5, 2

Hartley, R. I., Zisserman, A., 2004, Multiple View Geometry in Computer Vision, Cambridge University Press, Cambridge, 2nd ed.

Hassler, D. M., Dammasch, I. E., Lemaire, P., Brekke, P., Curdt, W., Mason, H. E., Vial, J.-C., Wilhelm, K., 1999, Solar Wind Outflow and the Chromospheric Magnetic Network, *Science*, 283, 810–813

Holschneider, M., 1993, Inverse radon transfoms through inverse wavelet transforms, Inverse Problems, 7, 853–861

Howard, R., Harvey, J., 1970, Spectroscopic Determinations of Solar Rotation, *Solar Physics*, 12, 23–51

Howard, R. A., Moses, J. D., Vourlidas, A., Newmark, J. S., Socker, D. G., Plunkett, S. P., Korendyke, C. M., Cook, J. W., Hurley, A., Davila, J. M., Thompson, W. T., St Cyr, O. C., Mentzell, E., Mehalick, K., Lemen, J. R., Wuelser, J. P., Duncan, D. W., Tarbell, T. D., Wolfson, C. J., Moore, A., Harrison, R. A., Waltham, N. R., Lang, J., Davis, C. J., Eyles, C. J., Mapson-Menard, H., Simnett, G. M., Halain, J. P., Defise, J. M., Mazy, E., Rochus, P., Mercier, R., Ravet, M. F., Delmotte, F., Auchere, F., Delaboudiniere, J. P., Bothmer, V., Deutsch, W., Wang, D., Rich, N., Cooper, S., Stephens, V., Maahs, G., Baugh, R., McMullin, D., Carter, T., 2008, Sun Earth Connection Coronal and Heliospheric Investigation (SECCHI), *Space Science Reviews*, 136, 67–115

Howe, R., 2009, Solar interior rotation and its variation, *Living Reviews in Solar Physics*, 6,1

Howell, S. B., Handbook of CCD astronomy, Cambridge University Press, Cambridge, 2nd ed.

Hudson, H. S., 2011, Global Properties of Solar Flares, *Space Science Reviews*, 158, 5–41

Inhester, B., 2006, Stereoscopy basics for the STEREO mission, ArXiv Astrophysics e-prints, arXiv:astro-ph/0612649v1

Jackson, J. D., 1975, Classical electrodynamics, Academic Press, New York, 2nd ed.

Jacques, L., 2004, Ondelettes, repéres et couronne solaire, Ph.D. thesis, Université catholique de Louvain, Belgium

Kaiser, M. L., Kucera, T. A., Davila, J. M., St. Cyr, O. C., Guhathakurta, M., Christian, E., 2008, The STEREO Mission: An Introduction, *Space Science Reviews*, 136, 5–16

Kamio, S., Curdt, W., Teriaca, L., Inhester, B., Solanki, S. K., 2010, Observations of a rotating macrospicule associated with an X-ray jet, *Astronomy and Astrophysics*, 510, L1–L5

Lang, K. R., 2001, The Cambridge Encyclopedia of the Sun, Cambridge University Press, Cambridge

Lemen, J. R., Title, A. M., Akin, D. J., Boerner, P. F., Chou, C., Drake, J. F., Duncan, D. W., Edwards, C. G., Friedlaender, F. M., Heyman, G. F., Hurlburt, N. E., Katz, N. L., Kushner, G. D., Levay, M., Lindgren, R. W., Mathur, D. P., McFeaters, E. L., Mitchell, S., Rehse, R. A., Schrijver, C. J., Springer, L. A., Stern, R. A., Tarbell, T. D., Wuelser, J.-P., Wolfson, C. J., Yanari, C., Bookbinder, J. A., Cheimets, P. N., Caldwell, D., Deluca, E. E., Gates, R., Golub, L., Park, S., Podgorski, W. A., Bush, R. I., Scherrer, P. H., Gummin, M. A., Smith, P., Auker, G., Jerram, P., Pool, P., Soufli, R., Windt, D. L., Beardsley, S., Clapp, M., Lang, J., Waltham, N., 2011, The Atmospheric Imaging Assembly (AIA) on the Solar Dynamics Observatory (SDO), *Solar Physics*, pp. 115–139

Llebaria, A., Lamy, P., 1999, Time Domain Analysis of Solar Coronal Structures Through Hough Transform TEC hniques, in Astronomical Data Analysis Software and Systems VIII, (Eds.) D. M. Mehringer, R. L. Plante, D. A. Roberts, vol. 172 of Astronomical Society of the Pacific Conference Series, pp. 46–50

Llebaria, A., Lamy, P., DeForest, C., Koutchmy, S., 1998, Time domain analysis of polar plumes observed with LASCO-C2 and EIT, in Solar Jets and Coronal Plumes, (Ed.) T.-D. Guyenne, vol. 421 of ESA Special Publication, pp. 87–92

Llebaria, A., Saez, F., Lamy, P., 2002, The fractal nature of the polar plumes, in From Solar Min to Max: Half a Solar Cycle with SOHO, (Ed.) A. Wilson, vol. 508 of ESA Special Publication, pp. 391–394

Mallat, S., 1998, A wavelet tour of signal processing, Academic Press

Mallat, S., Hwang, W., 1992, Singularity detection and processing with wavelets, *IEEE Transactions on Instrumentation and Measurement*, 38, 617–643

Moses, D., Clette, F., Delaboudinière, J.-P., Artzner, G. E., Bougnet, M., Brunaud, J., Carabetian, C., Gabriel, A. H., Hochedez, J. F., Millier, F., Song, X. Y., Au, B., Dere, K. P., Howard, R. A., Kreplin, R., Michels, D. J., Defise, J. M., Jamar, C., Rochus, P., Chauvineau, J. P., Marioge, J. P., Catura, R. C., Lemen, J. R., Shing, L., Stern, R. A., Gurman, J. B., Neupert, W. M., Newmark, J., Thompson, B., Maucherat, A., Portier-Fozzani, F., Berghmans, D., Cugnon, P., van Dessel, E. L., Gabryl, J. R., 1997, EIT Observations of the Extreme Ultraviolet Sun, *Solar Physics*, 175, 571–599

Natterer, F., 2001, The mathematics of computerized tomography, Society for Industrial and Applied Mathematics, Philadelphia, PA, USA

Newkirk, Jr., G., Harvey, J., 1968, Coronal Polar Plumes, *Solar Physics*, 3, 321–343

Nordlund, Å., Stein, R. F., Asplund, M., 2009, Solar Surface Convection, *Living Reviews in Solar Physics*, 6, 2

Paternò, L., 2010, The solar differential rotation: a historical view, *Astrophysics and Space Science*, 328, 269–277

Peter, H., 2001, On the nature of the transition region from the chromosphere to the corona of the Sun, *Astronomy and Astrophysics*, 374, 1108–1120

Phillips, K., 1992, Guide to the sun, Cambridge University Press, Cambridge

Podladchikova, O., 2002, Statistical model of quiet Sun coronal heating, Ph.D. thesis, Laboratoire de Physique et Chimie de l'Environnement (LPCE) of the french National Centre for Scientific Research (CNRS), University of Orléans

Raouafi, N.-E., Harvey, J. W., Solanki, S. K., 2007, Properties of Solar Polar Coronal Plumes Constrained by Ultraviolet Coronagraph Spectrometer Data, *Astrophysical Journal*, 658, 643–656

Raouafi, N.-E., Petrie, G. J. D., Norton, A. A., Henney, C. J., Solanki, S. K., 2008, Evidence for Polar Jets as Precursors of Polar Plume Formation, *Astrophysical Journal. Letters to the Editor*, 682, L137–L140

Rieutord, M., Rincon, F., 2010, The Sun's Supergranulation, *Living Reviews in Solar Physics*, 7, 2

Robbrecht, E., Berghmans, D., 2004, Automated recognition of coronal mass ejections (CMEs) in near-real-time data, *Astronomy and Astrophysics*, 425, 1097–1106

Saito, K., 1958, Polar Rays of the Solar Corona, *Publications of the Astronomical Society of Japan*, 10, 49–78

Saito, K., 1965, Polar Rays of the Solar Corona, II., *Publications of the Astronomical Society of Japan*, 17, 1–26

Sanchez Almeida, J., Bonet, J. A., Viticchié, B., Del Moro, D., 2010, Magnetic Bright Points in the Quiet Sun, *Astrophysical Journal. Letters to the Editor*, 715, L26–L29

Schmieder, B., Murdin, P., 2000, Chromosphere, Encyclopedia of Astronomy and Astrophysics

Simon, G. W., Leighton, R. B., 1964, Velocity Fields in the Solar Atmosphere. III. Large-Scale Motions, the Chromospheric Network, and Magnetic Fields., *Astrophysical Journal*, 140, 1120–1147

Snodgrass, H. B., Ulrich, R. K., 1990, Rotation of Doppler features in the solar photosphere, *Astrophysical Journal*, 351, 309–316

Solanki, S. K., 2003, Sunspots: An overview, *Astronomy and Astrophysics Review*, 11, 153–286

Solanki, S. K., Inhester, B., Schüssler, M., 2006, The solar magnetic field, *Reports on Progress in Physics*, 69, 563–668

Stenborg, G., Cobelli, P. J., 2003, A wavelet packets equalization technique to reveal the multiple spatial-scale nature of coronal structures, *Astronomy and Astrophysics*, 398, 1185–1193

Stenborg, G., Vourlidas, A., Howard, R. A., 2008, A Fresh View of the Extreme-Ultraviolet Corona from the Application of a New Image-Processing Technique, *Astrophysical Journal*, 674, 1201–1206

Stix, M., 2004, The sun: an introduction, Springer, Berlin

Stoddard, L. G., Carson, D. G., Saito, K., 1966, Polar Rays of the Solar Corona Observed at the 1963 Eclipse, *Astrophysical Journal*, 145, 796–799

Suess, S. T., 1982, Polar coronal plumes, *Solar Physics*, 75, 145–159

Suess, S. T., Poletto, G., Wang, A.-H., Wu, S. T., Cuseri, I., 1998, The Geometric Spreading of Coronal Plumes and Coronal Holes, *Solar Physics*, 180, 231–246

Tadesse, T., Wiegelmann, T., Inhester, B., 2009, Nonlinear force-free coronal magnetic field modelling and preprocessing of vector magnetograms in spherical geometry, *Astronomy and Astrophysics*, 508, 421–432

Teriaca, L., Poletto, G., Romoli, M., Biesecker, D. A., 2003, The Nascent Solar Wind: Origin and Acceleration, *Astrophysical Journal*, 588, 566–577

Thalmann, J. K., Wiegelmann, T., 2009, Magnetic Field Extrapolation of Flaring Active Regions, *Central European Astrophysical Bulletin*, 33, 131–140

Thernisien, A. F. R., Howard, R. A., Vourlidas, A., 2006, Modeling of Flux Rope Coronal Mass Ejections, *Astrophysical Journal*, 652, 763–773

Thompson, B. J., Plunkett, S. P., Gurman, J. B., Newmark, J. S., St. Cyr, O. C., Michels, D. J., 1998, SOHO/EIT observations of an Earth-directed coronal mass ejection on May 12, 1997, *Geophysical Research Letters*, 25, 2465–2468

Toft, P., 1996, The Radon Transform, Theory and Implementation, Ph.D. thesis, Technical Univesity of Danmark

Torrésani, B., 1995, Analyse Continue par Ondelettes, Éditions du CNRS

Ulmschneider, P., 1996, Chromosphere and coronal heating mechanisms, in Cool Stars, Stellar Systems, and the Sun, (Ed.) R. Pallavicini & A. K. Dupree, vol. 109 of Astronomical Society of the Pacific Conference Series, pp. 71–78

Vandergheynst, P., 1998, Ondelettes directionnelles et ondelettes sur la sphère, Ph.D. thesis, Université catholique de Louvain, Belgium

Virtanen, I. I., Mursula, K., 2010, Asymmetry of solar polar fields and the southward shift of HCS observed by Ulysses, *Journal of Geophysical Research*, 115, A09 110

Walker, Jr., A. B. C., DeForest, C. E., Hoover, R. B., Barbee, Jr., T. W., 1993, Thermal and Density Structure of Polar Plumes, *Solar Physics*, 148, 239–252

Wang, Y. M., 1998, Network Activity and the Evaporative Formation of Polar Plumes, *Astrophysical Journal. Letters to the Editor*, 501, L145–L150

Wang, Y.-M., Sheeley, Jr., N. R., 1995, Coronal Plumes and Their Relationship to Network Activity, *Astrophysical Journal*, 452, 457–461

Wang, Y.-M., Hawley, S. H., Sheeley, N. R., J., 1996, The Magnetic Nature of Coronal Holes, *Science*, 271, 464–469

Wiegelmann, T., 2008, Nonlinear force-free modeling of the solar coronal magnetic field, *Journal of Geophysical Research*, 113, A03S02

Wiegelmann, T., Inhester, B., 2003, Magnetic modeling and tomography: First steps towards a consistent reconstruction of the solar corona, *Solar Physics*, 214, 287–312

Wilhelm, K., Dammasch, I. E., Marsch, E., Hassler, D. M., 2000, On the source regions of the fast solar wind in polar coronal holes, *Astronomy and Astrophysics*, 353, 749–756

Wilhelm, K., Abbo, L., Auchére, F., Barbey, N., Feng, L., Gabriel, A., Giordano, S., Imada, S., Llebaria, A., Matthaeus, W., Poletto, G., Raouafi, N.-E., Suess, S., Teriaca, L., Wang, Y.-M., 2011, Morphology, dynamics and plasma parameters of plumes and inter-plume regions in solar coronal holes, *Astronomy and Astrophysics*, 19, 1–70

Zirin, H., 1966, The solar atmosphere, Blaisdell Publishing Company

Acknowledgements

It is a pleasure to convey my gratitude to a great number of people whose contributions in assorted ways have helped me to accomplish this research.

Foremost, I would like to express my sincere gratitude to my first supervisor Dr. Bernd Inhester for the continuous support in my PhD research, for sharing his immense knowledge, for his enthusiasm and his patience. His guidance helped me at every stage of the research and the writing of this thesis. My sincere thanks also go to Dr. Thomas Wiegelmann, my second supervisor, for his constant availability and for his readiness to sharing his expertise. I am also indebted to Borut Podlipnik for his ongoing technical support and for his exceptional patience.

I am very grateful to Friday Meeting Group for the numerous (non-)scientific discussions: Dr. Li Feng, Dr. Julia Thalmann, Iulia Chifu, Dr. Tilaye Tadesse Asfaw, Borut Podlipnik and the group leaders Dr. Bernd Inhester and Dr. Thomas Wiegelmann. Thank to this regular meeting, I never felt isolated in my own research and several times, I found solutions of problems by exposing them.

This thesis has been done at the Max Planck Institute for Solar System Research in the framework of the International Max Planck Research School. I would like to thank the director, Dr. Sami K. Solanki, for providing me this stimulating and comfortable research environment and also for his expertise and guidance in my work.

I also want to thank my supervisors at the Technical University of Braunschweig Dr. Sami K. Solanki and Dr. Karl-Heinz Glassmeier for careful reading of this thesis.

I cannot forget to express my sincere thanks to all my friends for making this time such an unforgettable time: Kristofer, Anne, Ray, Li, Hannah, Julia, Roberto, Richard, Ramy, Tijmen, Fatima, Pauline and all of you. Many thanks also go to the coffee group people and to the tireless coffee machine more reliable than any computer. I believe it, our super-scientific issues surounded by the smell of Lavazza coffee made healthier our workplace. And a special thank go to you guys who gave me back my climbing and mountaineering passion: Michal, Kristofer, Ray, Yana and Orlando.

Finally, I would like to offer my regards and blessings to all of those who supported me in any respect and who trusted me during the completion of the project, Paul de Patoul, Brigitte de Patoul, Mauro Sbolgi, Lionel Van Holle, Elena Podladchikova, Véronique H.-Buchholz and Orlando Arevalo.

Judith de Patoul